Summer 2024

Iterative Power Flow Control Architecture for DC-AC-AC Triple Active Bridge Converters: Design, Simulation, and Hardware Testing

Jonathan Henri Saelens
Missouri University of Science and Technology

Recommended Citation

Saelens, Jonathan Henri, "Iterative Power Flow Control Architecture for DC-AC-AC Triple Active Bridge Converters: Design, Simulation, and Hardware Testing" (2024). *Masters Theses*. 8216.
https://scholarsmine.mst.edu/masters_theses/8216

ITERATIVE POWER FLOW CONTROL ARCHITECTURE FOR DC-AC-AC TRIPLE ACTIVE BRIDGE CONVERTERS: DESIGN, SIMULATION, AND HARDWARE TESTING

by

JONATHAN HENRI SAELENS

A THESIS

Presented to the Graduate Faculty of the

MISSOURI UNIVERSITY OF SCIENCE AND TECHNOLOGY

In Partial Fulfillment of the Requirements for the Degree

MASTER OF SCIENCE

in

ELECTRICAL ENGINEERING

2024

Approved by:

Dr. Jonathan W. Kimball, Advisor
Dr. Pourya Shamsi
Dr. Mehdi Ferdowsi

PUBLICATION THESIS OPTION

This thesis consists of the following two papers, formatted in the style used by the Missouri University of Science and Technology.

Paper I: Pages 22-37, Instantaneous Current and Average Power Flow Characterization of a DC-DC-DC Triple Active Bridge Converter, has been published in the proceedings of the Power and Energy Conference at Illinois (PECI) in Urbana, IL, in April 2024.

Paper II: Pages 38-72, Iterative Power Flow Control Algorithm Development and Performance Analysis for a DC-AC-AC Triple Active Bridge Converter, is intended for submission to *IEEE Transactions on Power Electronics*.

ABSTRACT

Driven by widespread electrification and escalating energy demands, efficient and cost-effective converter systems are necessary to maintain and improve our nation's electrical grid. Facilitating this necessity are power electronic converters in applications such as smart grids, renewable energy integration, and electric vehicles. Guided by the demand for improved converter topologies and conversion efficiency, much research has been conducted on varying designs, development, and control implementations. One such topology gaining significant research attention is the triple active bridge (TAB) converter. The TAB is a three-port power converter enabling both bidirectional power flow on each port and galvanic isolation for safety and noise isolation purposes. Its modularity and adaptability allow for implementation in a variety of high-frequency conversion applications while its high efficiency minimizes power losses and further reduces its physical size.

The main focus of this work is the implementation of a DC-AC-AC triple active bridge converter. Initially, the defining system equations for instantaneous current and average power are developed. These equations are then validated for efficacy through a PLECS simulation model and utilizing a physical hardware prototype of the DC-DC-DC TAB. Secondly, a feed-forward control algorithm is presented for the TAB using the Newton-Raphson power control method as a framework for development. This power sharing implementation is then validated in both PLECS and physical hardware for the DC-DC-DC TAB. Lastly, the aforementioned control strategy is then extended for applications within the DC-AC-AC TAB, while also being substantiated through hardware analysis. Overall, the main contribution of this thesis focuses on the development required for the advancement of power electronic technology by expanding its application scope and providing novel methods for operation.

ACKNOWLEDGMENTS

I am incredibly grateful to my advisor, Dr. Jonathan W. Kimball, for allowing me this opportunity to pursue my master's and for his guidance, understanding, and willingness to teach. Every interaction with Dr. Kimball has provided a learning experience and opportunity for growth, and his support, even during challenging times, has been invaluable. I also appreciate my committee members, Dr. Pourya Shamsi and Dr. Mehdi Ferdowsi, for their invaluable support and guidance throughout my undergraduate and graduate experience.

I am also profoundly thankful to my parents, Johan and Lieve Saelens, who have not only supported me through my graduate program but also throughout the entirety of my life. Thank you for always encouraging me, even when things have gotten a little more challenging. You have truly been an inspiration and have led me to who I have become today. To my incredible sisters, Heleen and Liz, thank you for providing love and support, and always encouraging me to keep going even when times got busy. I love you all!

To Lauren, who stood by and encouraged me all the way to the end, even when things got busy, difficult, and I felt disheartened. Thank you not only for always being there for me and loving me, but also for being my best friend. I love you so much!

I would not have been able to achieve this accomplishment without the unwavering support of my best friend and lab mate, Oroghene Oboreh-Snapps. With our final defense being just four short days apart, having someone to navigate the intricacies and push each other right up until the end has been vital to my success. I would also like to thank all my other lab members, Praneeth, Lauryn, Arnold, and Sophia, for always being my support structure. I am thankful for our after-hours and weekend Uno and Monopoly game nights.

I would like to thank the DOE Office of Electricity Energy Storage Program and Dr. Imre Gyuk for their generous financial support, and Dr. Stan Atcitty and Dr. Jacob Mueller for envisioning the DC-AC-AC Triple Active Bridge converter project.

TABLE OF CONTENTS

Page

PUBLICATION THESIS OPTION iii

ABSTRACT iv

ACKNOWLEDGMENTS v

LIST OF ILLUSTRATIONS ix

LIST OF TABLES xi

SECTION

1. INTRODUCTION 1

  1.1. MOTIVATION AND OBJECTIVES 3

  1.2. SCOPE AND LIMITATIONS 6

  1.3. CHALLENGES IN EXISTING APPLICATIONS 8

2. LITERATURE REVIEW 10

  2.1. MULTILEVEL H-BRIDGE CONVERTER 11

  2.2. PHASE-SHIFTED FULL BRIDGE CONVERTER 13

  2.3. DUAL ACTIVE BRIDGE 15

  2.4. RESONANT CONVERTERS 17

  2.5. TRIPLE ACTIVE BRIDGE 20

PAPER

I. INSTANTANEOUS CURRENT AND AVERAGE POWER FLOW CHARACTERIZATION OF A DC-DC-DC TRIPLE ACTIVE BRIDGE CONVERTER 22

  ABSTRACT 22

  1. INTRODUCTION 23

  2. DC-DC-DC TAB CONVERTER TOPOLOGY 24

3. SYSTEM EQUATIONS 25
4. RESULTS 27
    4.1. INSTANTANEOUS CURRENT EQUATIONS 31
        4.1.1. Unity Transformer Case 31
        4.1.2. Non-Unity Transformer Case 31
        4.1.3. Hardware Verification 32
    4.2. POWER FLOW EQUATIONS 33
        4.2.1. Unity Transformer Case 34
        4.2.2. Non-Unity Transformer Case 34
        4.2.3. Comparison to Previous Work 35
5. CONCLUSION 36
REFERENCES 36

II. FEED-FORWARD CONTROL ALGORITHM DESIGN AND PERFORMANCE ANALYSIS FOR A DC-DC-DC TRIPLE ACTIVE BRIDGE CONVERTER 38
ABSTRACT 38
1. INTRODUCTION 39
2. TRIPLE ACTIVE BRIDGE CONVERTER TOPOLOGY 43
    2.1. SYSTEM EQUATIONS 46
3. PROPOSED ALGORITHM 47
4. CONTROL ITERATION EFFICIENCY 52
5. DC-DC-DC TAB RESULTS 53
    5.1. UNITY TRANSFORMER SIMULATION RESULTS 57
    5.2. NON-UNITY TRANSFORMER SIMULATION RESULTS 57
    5.3. HARDWARE RESULTS 58
6. DC-AC-AC TAB HARDWARE RESULTS 60
7. CONCLUSION 64

8. APPENDIX - TAB SYSTEM DESIGN 65
    8.1. TRANSFORMER CONSTRUCTION 66
    8.2. TAB TWO-SWITCH BOARD 67
    8.3. SYSTEM VARIABLE MEASUREMENT 68
    8.4. GENERAL BRIDGE AND PORT CONSTRUCTION 68
        8.4.1. DC Bridge and Port Construction 69
        8.4.2. AC Bridge and Port Construction 69
REFERENCES 70

SECTION

3. CONCLUSIONS AND FUTURE WORK 73
    3.1. SUMMARY 73
    3.2. FUTURE WORK 74

APPENDICES

A. TAB TWO-SWITCH BOARD PCB SCHEMATIC AND LAYOUT 77

B. DC-AC-AC TAB NEWTON-RAPHSON MATLAB CONTROL CODE 83

REFERENCES 91

VITA 96

LIST OF ILLUSTRATIONS

Figure Page

SECTION

1.1. DAB distorted output current waveform. 4

1.2. DAB distorted output power waveform. 5

2.1. Solid state transformer configurations. Type A, B, C, and D. 11

2.2. Topology of a DC-DC multilevel H-bridge converter. 12

2.3. Topology of a DC-DC phase-shifted full bridge converter. 14

2.4. Topology of an AC-AC dual active bridge power converter. 16

2.5. Topology of a DC-DC LLC resonant converter. 18

2.6. Topology of a DC-DC CLLC resonant converter. 19

2.7. Topology of a DC-DC CLLLC resonant converter. 19

2.8. Topology of a DC-AC-AC triple active bridge power converter. 20

PAPER I

1. Triple active bridge circuit topology. 24

2. Diagram of six possible phase shift configurations within the TAB and their respective power transfer directions. 25

3. Periodic triple active bridge waveforms. Three-bridge transformer voltages and single-bridge (bridge 1) transformer current. 28

4. PLECS simulated system current vs calculated equation current with a 1:1:1 transformer ratio. The x-axis corresponds to time in seconds and the y-axis corresponds to current in amps. $T = \frac{1}{30{,}000}$ 29

5. PLECS simulated system current vs calculated equation current with a 1:4:2 transformer ratio. The x-axis corresponds to time in seconds and the y-axis corresponds to current in amps. $T = \frac{1}{30{,}000}$ 30

6. Instantaneous current TAB waveforms. Top to bottom: dark blue = bridge 1 current, light blue = bridge 2 current, pink = bridge 3 current, green = bridge 1 transformer voltage. $\phi_2 = 20°$, $\phi_3 = 30°$. 32

7. DC-DC-DC TAB hardware test setup. 33

8. Sweep of ϕ_2 parameter comparing PLECS simulated power vs calculated equation power with varying ϕ_3 values for a 1:1:1 transformer ratio. 34

9. Sweep of ϕ_2 parameter comparing PLECS simulated power vs calculated equation power with varying ϕ_3 values for a 1:4:2 transformer ratio. 35

10. Comparison of P_2 equation of PLECS output vs newly proposed equations vs previous work. 36

PAPER II

1. Topology of a DC-AC-AC triple active bridge power converter. 40

2. Diagram of six possible phase shift configurations within the TAB and their respective power transfer directions. 44

3. PLECS derived graphs of the proposed Newton-Raphson control algorithm implementation with a 1:1:1 transformer turns ratio. 54

4. PLECS derived graphs of the proposed Newton-Raphson control algorithm implementation with a 1:4:2 transformer turns ratio. 55

5. DC-DC-DC TAB hardware test setup. 58

6. Hardware derived graphs of the proposed Newton-Raphson control algorithm implementation with a 1:1:1 transformer turns ratio. 59

7. MATLAB generated ϕ values. $P_{1,d} = 0W$, $P_{3,d} = 60W$, $Q_{3,d} = 10VAR$. 61

8. Hardware generated ϕ values. Top to bottom: dark blue = ϕ_2, light blue = ϕ_3, pink = DC bridge voltage, green = AC bridge 2 voltage. $P_{1,d} = 0W$, $P_{3,d} = 60W$, $Q_{3,d} = 10VAR$. 62

9. MATLAB generated ϕ values. $P_{1,d} = 0W$, $P_{3,d} = -60W$, $Q_{3,d} = -10VAR$. 62

10. Hardware generated ϕ values. Dark blue = ϕ_2, light blue = ϕ_3, pink = DC bridge voltage, green = AC bridge 2 voltage. $P_{1,d} = 0W$, $P_{3,d} = -60W$, $Q_{3,d} = -10VAR$. 63

11. AC zero crossing transformer voltage and current waveforms. Dark blue = AC bridge 2 voltage, light blue = bridge 2 transformer voltage, pink = bridge 3 transformer voltage, green = bridge 2 transformer current. $\phi_2 = 0$, $\phi_3 = 0$. 64

12. DC-AC-AC TAB hardware test setup. 65

13. N87 transformer core material and 3D printed bobbin. 66

14. TAB two-switch board. 67

15. Voltage and current measurement board. 68

LIST OF TABLES

Table Page

PAPER I

1. Default TAB system parameters. 28
2. Unity transformer TAB system parameters... 28
3. Non-unity transformer TAB system parameters. 28

PAPER II

1. Newton-Raphson iteration measurement.. 52
2. Default TAB system parameters. 56
3. Unity transformer DC-DC-DC TAB system parameters........................... 56
4. Non-unity transformer DC-DC-DC TAB system parameters. 56
5. Unity transformer DC-AC-AC TAB system parameters. 61

SECTION

1. INTRODUCTION

Electricity plays a vital role in supporting a myriad of important daily operations including individuals and infrastructure. Ensuring a reliable supply of energy to meet this fluctuating demand requires efficient electrical sources and robust distribution lines. Energy generation includes the two main categories of non-renewable and renewable sources, with coal, oil, and natural gas being the most prominent non-renewable sources, and hydroelectric, wind, and solar being the most common renewable sources. Throughout the energy transmission process, multiple forms of energy conversion are typically required. For transmission across long distances, alternating current (AC) is customarily used for its reduced power losses, voltage regulation, and cost-effectiveness. Storing energy for future use involves converting from AC into direct current (DC) to charge batteries, and super-capacitors, or storing it as hydroelectric or thermal potential. In addition, voltage magnitude modulation is a frequent necessity often achieved utilizing large 60 Hz transformers placed adjacent to buildings or power distribution centers. While these transformers provide simplistic and effective voltage conversion, recent advancements in power electronics have propelled energy distribution to the forefront of transformative innovation. Not only does the integration of power electronics substantially reduce the overall footprint of electrical power conversion, but it also facilitates the implementation of sophisticated power regulation techniques. By replacing a conventional 60 Hz transformer with a solid state transformer (SST), voltage regulation, power flow control, frequency regulation, and grid support can be incorporated while preserving the inherent functionality of traditional systems.

In essence, a power electronic converter serves as an intermediary between varying electrical sources, loads, and energy storage devices. Its primary objective is to facilitate the controlled conversion of electrical energy from one form to another. Given the diverse power requirements indicated by modern-day electrical devices, ensuring the adaptability of converter systems is paramount. Some devices operate using AC while others use DC, some necessitate high voltage while others require low voltage, and some consume significant power while others consume comparatively low power. As a result, power electronics must be carefully designed with efficiency and adaptability as paramount objectives. The versatility of power electronics enables the integration of renewable energy sources, efficient power distribution, and optimization of energy utilization across all applications.

As more research is invested in the innovation of electronic devices such as vehicles and machines, the versatility and applications for power electronic converters continue to increase. Global energy demand has surged throughout the last few decades, prompting the drive toward sustainable energy solutions and emphasizing the pivotal role of power converters. Additionally, electric vehicles (EVs) have seen significant enhancements, and distributed energy resources (DERs) have proliferated in recent years. For each of these applications and more, converters enable efficient energy storage, vehicle-to-grid (V2G) integration, and bidirectional power flow control. This not only enhances energy sustainability but also fosters innovation in smart grid technologies and decentralized energy systems.

To accommodate the aforementioned large array of applications and varying load conditions, significant research has led to the development of a wide variety of power electronic converter topologies. One such more recent topology, the triple active bridge (TAB), represents a significant leap forward in conversion flexibility, efficiency, and grid integration capabilities. Comprised of three active H-bridges, the TAB allows for bi-directional power flow while enabling galvanic isolation through a high-frequency transformer. Its modular design allows each bridge to be independently connected to either AC or DC sources. Leveraging sophisticated control algorithms and high-frequency switching techniques, the TAB ensures precise regulation of voltage, frequency, and power flow. The potential applications for this topology are limitless, including an on-board EV charger with one AC input port and two DC output ports for charging the low-voltage and high-voltage vehicle batteries. Another application is grid-tied energy storage in which one port is an AC grid input, another is an AC grid output, and the third is a DC battery storage system allowing for grid support and power compensation. This application constitutes the primary focus of this thesis.

1.1. MOTIVATION AND OBJECTIVES

As modern electrical systems and infrastructures continue to evolve, the demand for advanced power electronic solutions becomes increasingly pronounced. This demand arises from the necessity for efficient and flexible power conversion, driven by factors such as the growing integration of renewable energy sources, the electrification of transportation, and the modernization of electrical infrastructure. Despite significant advancements made within power electronics, many challenges still exist which have been outlined comprehensively in Section 1.3. These challenges hinder the widespread adoption of such advanced converter topologies. One of the defining motivations behind this research is to address a subset of these challenges and contribute to the enhancement of power electronic topologies. Specifically, the focus is on the design and development of the triple active bridge power converter.

Efficiency is a fundamental concern in power electronic converters, as any losses can contribute to increased operational costs, higher converter operating temperatures, and potentially reduced converter longevity. Through the investigation of novel control strategies and the integration of optimization techniques such as soft switching, the efficiency losses can be mitigated and improved converter performance can be achieved. By exploring new avenues for innovation, significant contributions can be made to the field of power electronics, renewable energy integration, and grid modernization. Even incremental improvements in converter efficiency carry the potential for far-reaching implications for the future of energy sustainability and electrification.

Previous research in the same application space has mainly been centered around the AC-AC DAB, of which its operational principles are extensively covered in Section 2.3. One of its main drawbacks is presented when considering the transmission of reactive power through the converter. This results in a desired output power waveform slightly shifted from the output voltage waveform. Due to the area surrounding the zero crossings of the input voltage source, the transmission of current from the input port to the output port during this time becomes unachievable, resulting in the distorted output power waveform in Figure 1.2, and the distorted output current waveform in Figure 1.1. Through the incorporation of a third port containing a battery energy storage system (BESS), the existing DAB architecture can be improved allowing current to be provided to the output AC port regardless of the voltage state at the input AC port.

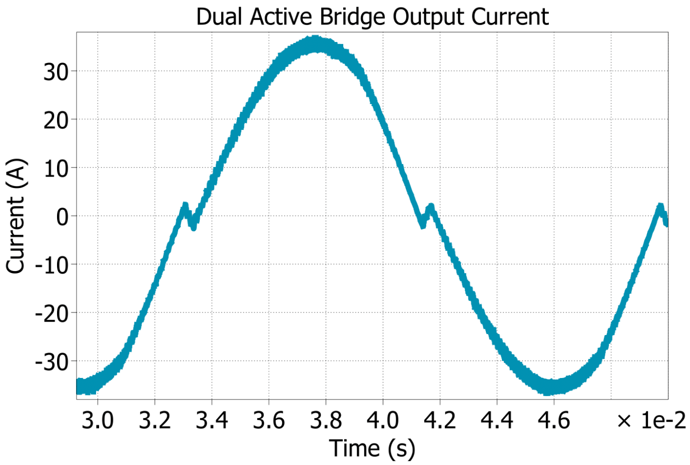

Figure 1.1. DAB distorted output current waveform.

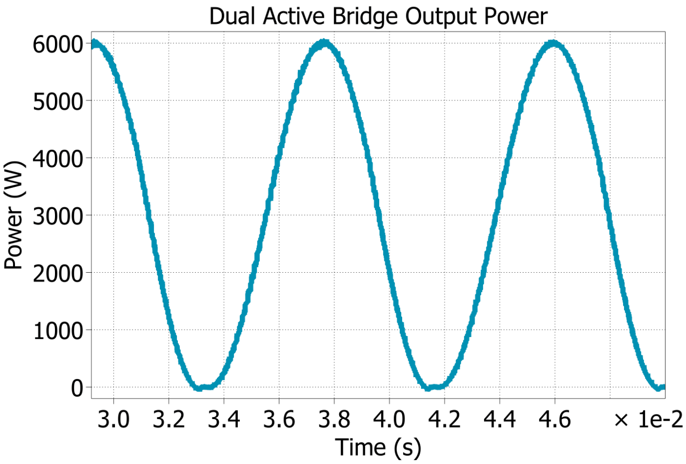

Figure 1.2. DAB distorted output power waveform.

The specific objectives and goals presented within this thesis research in order of completion are listed as follows:

1. Equation generation of a DC-DC-DC TAB converter: Developed and validated the instantaneous current and average power equations for the TAB converter which elucidate its defining operating principles.

2. Design and simulation of a DC-DC-DC TAB converter: Developed a detailed design and control methodology for a TAB converter prototype using the PLECS circuit simulation software suite. Included were optimization and validation of converter topology and design of control algorithms to meet specified performance requirements.

3. Hardware construction and experimental validation: The hardware prototype for the DC-DC-DC TAB was constructed, taking into account the required hardware configuration for the ultimate structure, the DC-AC-AC TAB. The generated control algorithm was applied to the converter to experimentally validate its efficacy.

4. Design and simulation of a DC-AC-AC TAB converter: Validated the hardware architecture for the new TAB configuration and extended the DC control methodology to encompass the AC case. Initial verification took place within the PLECS circuit simulation software suite.
5. Performance evaluation and experimental validation of a DC-AC-AC TAB: Modified the existing hardware to encompass the new composition, implemented the updated control scheme, and validated the converter's effectiveness. This included analyzing efficiency and a comparative analysis of the desired versus the achieved waveforms.
6. Analysis and future perspectives: Analyzed the performance of the DC-AC-AC TAB converter, highlighting its advantages, limitations, and potential applications. Additionally, provided insights into future research directions, emerging technologies, and areas for further improvement in TAB converter design and implementation.

By addressing the above objectives, this thesis contributes to the advancement of the DC-AC-AC TAB converter technology, fostering innovation in power electronics and facilitating the transition towards sustainable and resilient electrical systems.

1.2. SCOPE AND LIMITATIONS

The scope of this thesis encompasses an in-depth investigation into the DC-AC-AC triple active bridge power converter, focusing on specific aspects pertinent to its design, control, and performance analysis. The research has been conducted through the exploration of two main papers, each addressing distinct facets of the TAB converter.

The conference paper delves into the design and analysis of the defining instantaneous current and average power equations for the DC-DC-DC TAB converter configuration. This paper contributes to laying the theoretical foundation necessary for understanding the fundamental operating principles and performance characteristics of triple active bridge converters within the DC domain.

The journal paper focuses on the introduction of a novel control strategy tailored for the TAB, utilizing the average power flow equations generated in the conference paper. The control architecture integrates an extended version of the Newton-Raphson method to determine the phase shift parameters, ϕ_2 and ϕ_3, based on user-input power requirements at two of the bridges. Additionally, the algorithm is validated for computational efficiency to ensure practical application on various microcontrollers. The algorithm is also tested on both DC-DC-DC and DC-AC-AC TAB hardware ensuring its applicability and adaptability on multiple configurations. This paper aims to enhance the control flexibility and efficiency of the converter, paving the way for optimized power flow regulation.

While this research aims to comprehensively design the DC-AC-AC TAB converter with full effectiveness, time limitations and other theoretical constraints have made way for minor inefficiencies within the overall TAB implementation. Such inefficiencies can be further diagnosed and researched in the future, and are listed as follows:

1. Since the transition between power being supplied by the DC and AC input bridges is rather abrupt surrounding the voltage zero crossing, this causes some distortion in the current waveform on the AC input source. Further investigation can include softening the transition between bridge utilization or modifying the control methodology to prioritize sinusoidal input current.

2. Due to the complexity of the DC-AC-AC TAB architecture, the development of a mathematical model of the system becomes quite cumbersome. Such a model would be beneficial in determining alternate converter control schemes which may or may not provide improved reliability and performance to the Newton-Raphson method presented within this research.

1.3. CHALLENGES IN EXISTING APPLICATIONS

The desire and necessity for performing research is driven by the numerous challenges encountered throughout the field of power electronics. Some of these are experienced throughout the design of the converter, while others are limited to its integration and application. Performing research while maintaining sight of the challenges presented below allows for improved converter designs and enhanced applicability.

The first main challenge is that of converter efficiency. In a realistic application, the attainment of one hundred percent conversion efficiency is not possible. Regardless of the attention to detail and investment in converter topology design, the parasitic resistance, inductance, and capacitance of traces and other components will generate a tangible form of efficiency loss. Specifically pertinent to power electronics, the main sources of power loss include switching losses within the MOSFETs and conduction losses, particularly at high power levels or under variable load conditions. While it is impossible to completely mitigate system losses, careful design optimization, advanced control techniques, and the conscientious selection of semiconductor devices can aid in significantly improving the overall converter efficiency.

Another main challenge germane to power electronics is that of control methodologies. Control methodologies refer to the accurate and timely switching of the MOSFETs, typically dependent on instantaneous system voltages or currents. Unsuccessful implementation of a control strategy within a hardware system can result in converter reliability or efficiency issues, cause converter component damage, or at worst, physical or material harm. While it is largely beneficial to validate control architectures using a circuit simulation software suite such as PLECS, it is difficult to accurately model all realistic elements of the system, and therefore the physical implementation may yield somewhat differing results. Most converters are also typically non-linear and dynamic. Coupled with varying load conditions and system disturbances, the design and implementation of effective control strategies is not simplistic. These strategies must also address transient response, voltage regulation, and harmonic mitigation to enhance the system's stability and performance.

The third main complication is that of reliability and durability. Power electronic devices are typically subjected to harsh operating conditions including high temperatures and mechanical and electrical stresses. Under such harsh conditions, the performance and lifespan of semiconductor devices, capacitors, and other components can be degraded over time. Furthermore, adverse design choices such as thermal management, component stresses, and layout designs can exacerbate reliability issues, leading to increased necessitated maintenance or system failures. Ensuring robustness and longevity in converter designs demands careful consideration of component selection, thermal design, and reliability testing methodologies.

Additionally, cost and scalability are two other difficulties impacting the implementation of power electronics. Due to the complexity of power electronic converters, initial costs can be prohibitive, particularly when it comes to large-scale deployment. Ongoing maintenance costs and component replacement are unlikely to be massively expensive, assuming the proper use of design principles within the converter, but may still prove to be a challenge in some areas. Improving the cost-effectiveness and scalability of power electronic integration requires innovations in converter design, manufacturing processes, and supply chain management to reduce production costs, streamline installation, and enhance system reliability and performance.

2. LITERATURE REVIEW

In the quest for efficient and reliable power conversion, much research has been conducted to develop a multitude of different power converter topologies. While it is difficult to obtain a one-size-fits-all topology, each of them offers varying advantages concerning enhanced energy efficiency, grid integration capability, and both hardware and control complexity. This literature review delves into the most common converter topologies, including the multilevel H-bridge converter, the phase-shifted full bridge converter, the dual active bridge, a handful of resonant converters, and the triple active bridge. Each of the aforementioned topologies represents an innovative approach to power conversion and is generally developed using one or more H-bridges as the fundamental structure. In addition, they leverage advanced control strategies and semiconductor technologies to address the evolving demands of modern electrical systems. Specifically pertinent to applications in electric vehicles, a complete overview of charger technologies has been presented in [1].

Among the various topologies in power electronics, the solid-state transformer (SST) finds its way into many power distribution applications. Serving as a modern replacement for traditional electromagnetic transformers within power distribution systems [2], an SST maintains the original functionality of its predecessor while offering bi-directional power flow, voltage regulation, and grid synchronization capabilities. SSTs incorporate AC sources on both the input and the output but may have one or more stages of DC link capacitors. Shown in Figure 2.1, there are four main types of SSTs: A, B, C, and D. Type A SSTs contain one conversion stage with no DC link. Type B and C SSTs have two stages with a single central DC link. The differentiating factor of both types is the placement of the high-frequency transformer. Assuming power flow is from left to right, type B has the transformer closest to the input, allowing input isolation from the DC link capacitors, and type C has the transformer closest to the output, allowing output isolation from the DC link capacitors. Type D consists of three stages, with two DC link elements. The transformer is placed centrally to ensure only one DC link is electrically coupled to each input or output source.

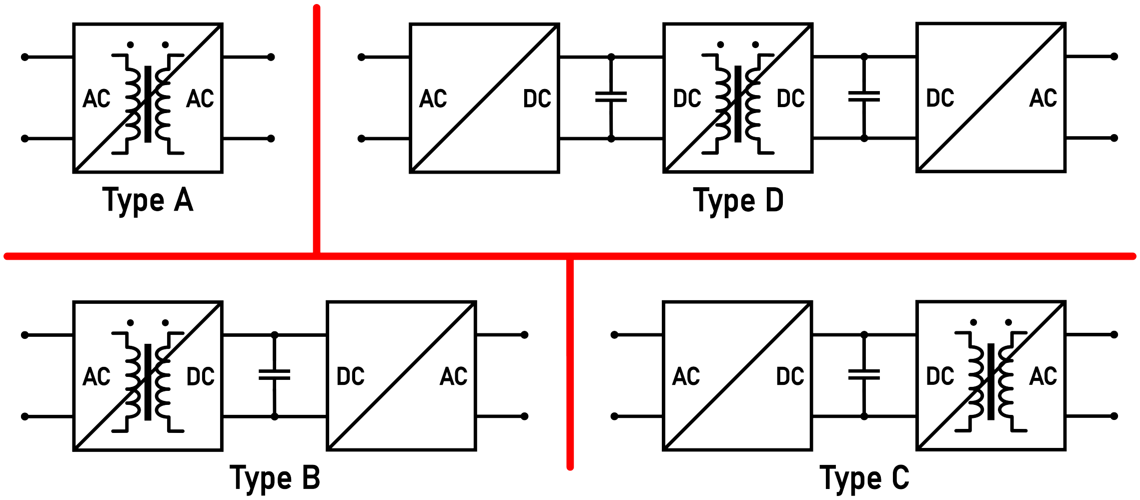

Figure 2.1. Solid state transformer configurations. Type A, B, C, and D.

Configuration of an SST in parallel or series is also feasible to achieve higher current capability or higher voltage, respectively. The design methodology and implementation example of an input series output parallel configuration is presented in [3]. When compared to a traditional 60 Hz transformer, an SST is slightly less efficient due to its added complexity and higher component count, as compared in [4]. However, the employment of improved control architectures such as soft switching can aid in decreasing this efficiency gap. In addition, the antecedent benefits outweigh the slight degradation in efficiency.

2.1. MULTILEVEL H-BRIDGE CONVERTER

The multilevel H-bridge converter is a prominent topology in power electronics renowned for its ability to generate near-sinusoidal output waveforms with reduced harmonic distortion and switching losses. At its core, this converter consists of multiple H-bridge segments, as shown in Figure 2.2, cascaded together to generate varying output voltage levels resembling a staircase waveform. These segments, each comprised of four semiconductor switches arranged in an H configuration, enable bidirectional current flow and voltage regulation. By controlling the switching states of individual segments, the converter achieves higher voltage resolution than traditional two-level converters due to its ability to produce additional voltage levels. An overview of this topology and output waveforms of the five, seven, and nine-level configurations are presented in [5]. This paper also presents configurations with unequal input voltage sources.

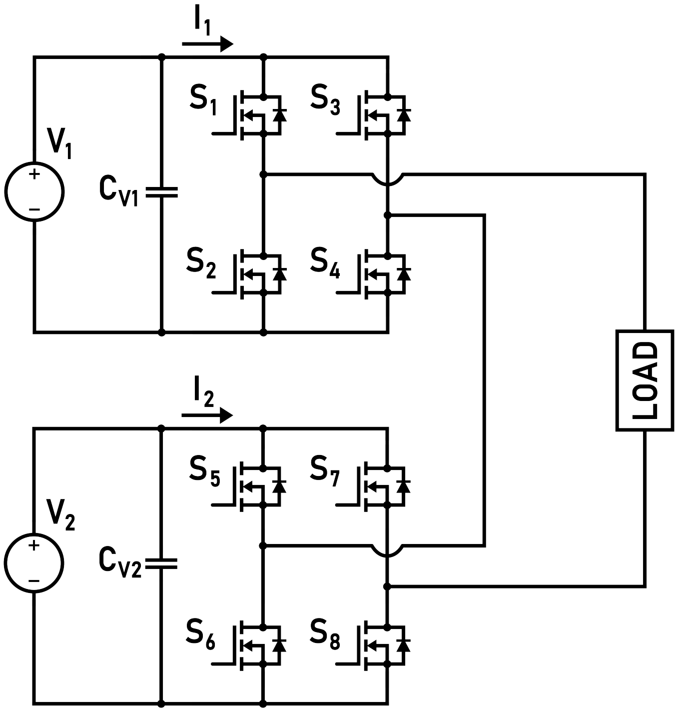

Figure 2.2. Topology of a DC-DC multilevel H-bridge converter.

The multilevel H-bridge converter boasts many key benefits, one of which includes its improved output waveform quality. The addition of multiple levels within the converter enables the generated output waveforms to contain reduced harmonic distortion. This leads to smoother voltage and current waveforms and improved power quality. Additionally, since the voltage is distributed among all input sources, the switches are not subjected to the full output voltage. This lowers the overall switching losses incurred by each switch, contributing positively to the overall system efficiency and reliability. Thirdly, due to the modularity and scalability of this topology, it can be adapted to wide ranges of input voltages and power requirements. Some of the drawbacks incurred by this topology include the lack of physical isolation between inputs and outputs. Next, the continual addition of levels brings diminishing returns in the form of cost and control complexity. Controlling the switch states of multiple H-bridge segments requires sophisticated control algorithms and gate drive circuitry. Achieving an optimal balance between output harmonic distortion and level complexity is crucial for effective converter design.

Despite these challenges, this converter topology is applicable in many applications including renewable energy systems. Due to the near-sinusoidal output voltage waveform and high conversion efficiency, it is an excellent choice for grid tied applications including photovoltaic inverters and wind turbine converters. Additionally, the multilevel H-bridge topology is widely used in high-voltage motor drives. By combining three such converters, it is possible to generate a three-phase AC waveform capable of driving an induction motor, as presented in [6]. Finally, the multilevel H-bridge is commonly used as active power filters to improve power quality and reduce harmonic distortion in grid-connected systems.

In summary, the multilevel H-bridge converter offers a compelling solution for high-quality power conversion across diverse applications. Its unique topology can be leveraged to achieve superior efficiency, voltage regulation, and power quality. Through ongoing advancements in semiconductor and control algorithms, the multilevel H-bridge converter continues to drive innovation in power electronics and facilitate the integration of renewable energy sources into modern electrical grids.

2.2. PHASE-SHIFTED FULL BRIDGE CONVERTER

The phase-shifted full bridge converter is a topology in which two bridges are connected through a high frequency transformer, improving safety and providing noise isolation. The input bridge consists of an active bridge with four electronic switches, or MOSFETs, and the output bridge is a passive bridge containing four diodes as an AC to DC rectifier. A depiction of this topology can be seen in Figure 2.3. This converter operates through a phase shift introduced between each leg of the H-bridge. Altering this phase shift modulates the quantity of power transferred from the input to the output, with an illustration of the system's operational states presented in [7].

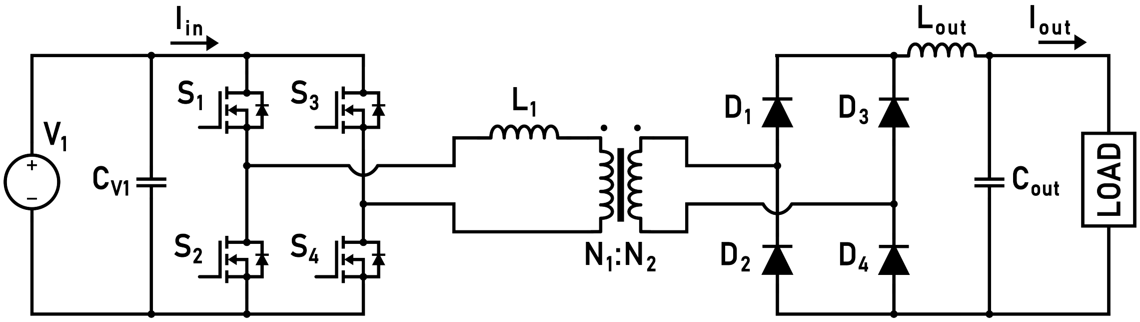

Figure 2.3. Topology of a DC-DC phase-shifted full bridge converter.

The phase-shifted full bridge converter offers several benefits, including high efficiency and precise voltage regulation. Through adjustment of the phase shift between switching signals, the converter can be optimized to achieve high performance under varying load conditions while minimizing losses. The incorporation of the high frequency transformer allows for improved safety and can be used to modify the voltage magnitude. In addition, the control algorithm of this topology is relatively simple due to only having one active bridge, and zero voltage switching implementation is possible to reduce switching losses, as shown in [8]. However, the diode-based output bridge leads to non-negligible power loss and voltage drop at higher output power and limits the topology to unidirectional power flow. Additionally, the inclusion of an isolation transformer increases the converter's overall footprint, which may pose a challenge in smaller applications.

Despite these drawbacks, the phase-shifted full bridge converter finds applications in various high-power and high-voltage systems requiring precise voltage regulation and efficient power conversion. Electric vehicle chargers are a prominent application as they must establish high efficiency regardless of the output load [7]. Additionally, uninterruptible power supplies and high-power motor drives are common instances of the phase-shifted full bridge converter. This converter's ability to handle high-power densities and provide galvanic isolation makes it well-suited for demanding industrial applications where reliability, efficiency, and simplicity are crucial.

In conclusion, the phase-shifted full bridge converter is a quality solution for high-power applications in which efficient power conversion and precise voltage regulation are of utmost importance. While it faces limitations such as slightly increased power loss due to the diode bridge and a larger footprint due to the isolation transformer, its benefits of safety and high efficiency outweigh these drawbacks in many industrial applications.

2.3. DUAL ACTIVE BRIDGE

The dual active bridge (DAB) is a highly versatile converter topology renowned for enabling bi-directional power flow and power conversion between two independent voltage sources. It is constructed with two active bridges with four switches, or MOSFETs, connected in a full bridge configuration, separated by a high-frequency transformer, as shown in Figure 2.4. The DAB operates by introducing a phase shift, denoted as ϕ, between the switching signals of its primary and secondary bridges. The magnitude of the phase shift indicates the amount of power flow, with a larger phase shift indicating more power transfer. A positive value of ϕ indicates power flow from bridge 1 to bridge 2, or as in Figure 2.4 from left to right, and a negative value of ϕ indicates power flow from bridge 2 to bridge 1, or from right to left. While the DAB typically operates at a fixed duty cycle of 50%, modulation of this duty cycle, as described in [9], can lead to improved converter efficiency and a reduced converter size. In the case where the duty cycle is fixed at 50%, it is the transformer turns ratio that determines the voltage magnitude on the output.

The DAB accommodates both DC and AC sources, making it adaptable to many different applications. In the DC-DC variant, the converter facilitates efficient energy transfer from the load to the source analyzed by a power flow model presented in [10]. Since the DC case lacks time-varying components, the phase shift must only be calculated once per

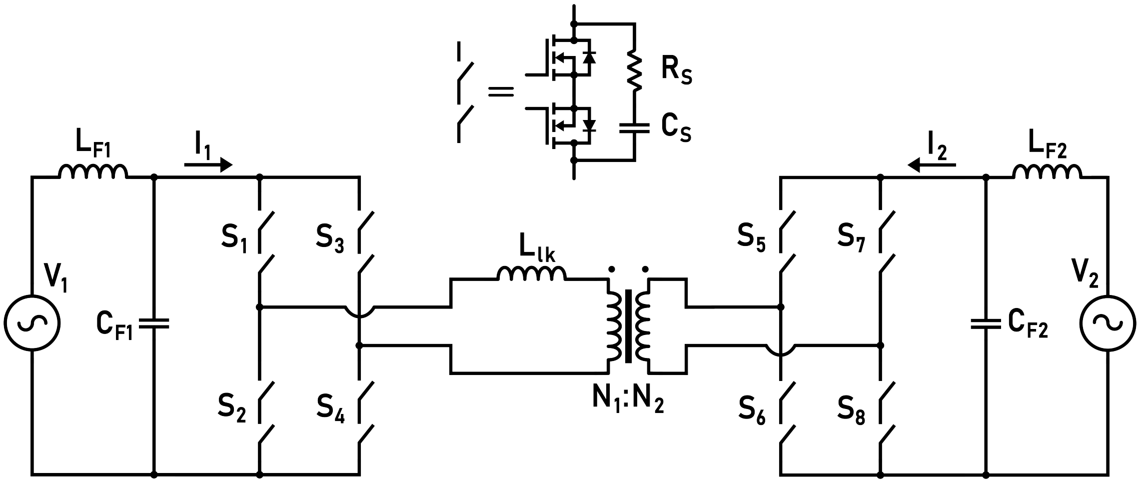

Figure 2.4. Topology of an AC-AC dual active bridge power converter.

measured variation in the voltages or connected loads. In the AC-AC variant, the converter typically serves as a power filter or grid-tied inverter for renewable energy systems. Utilizing a phase lock loop controller, the converter can be synchronized with the grid voltage to regulate the output voltage and frequency, improving the overall power quality. Provided within [11] is a comprehensive overview and proposal of the AC-AC DAB converter topology.

The main advantage of the DAB lies in its ability to accommodate bi-directional power flow and provide galvanic isolation, making it suitable for applications requiring voltage regulation, power factor correction, and grid integration of renewable energy sources. Additionally, the DAB offers high conversion efficiency which can be further improved through control techniques such as soft switching. However, the incorporation of two active bridges significantly complicates the control algorithms, and generation of a mathematical system model is quite challenging. Despite its complexity, the design and implementation of a closed-loop control algorithm for the DC-DC case is presented in [12], and one for the AC-AC case is illustrated in [13]. A method of obtaining a mathematical system model using the generalized average modeling approach is presented in [14]. Specific to the AC-AC implementation of the DAB, the transfer of reactive power causes the required output power to become phase shifted from the output voltage. This results in the inability to transfer current from the input bridge to the output bridge surrounding the voltage zero crossings at the input bridge, distorting the sinusoidal nature of the output current [15].

The DAB finds itself in a multitude of applications requiring efficient power conversion and voltage regulation. In the DC-DC case, common applications include large-scale energy storage systems [16] and electric vehicle charging infrastructures. In the AC-AC case, the converter is placed in many grid-tied renewable energy systems, active power filters, and energy storage systems. Through grid phase synchronization and power transfer controllability, the DAB facilitates seamless integration of renewable energy sources and enhances grid power quality.

In closure, the dual active bridge converter is a robust solution for efficient power conversion and voltage regulation in diverse applications. Despite challenges in control complexity and reactive power transfer, its bi-directional power flow capability and galvanic isolation make it highly applicable for modern energy systems, contributing to the advancement of renewable energy integration and grid stability.

2.4. RESONANT CONVERTERS

Resonant converters are comprised of active switches arranged in the H-bridge configuration and resonant tank circuits. These tank circuits consist of varying numbers of inductors (L) and capacitors (C) arranged in differing forms, with the three most common variations being the LLC, the CLLC, and the CLLLC. Operating at or close to the resonant frequency of the converter, the output voltage and current waveforms are sinusoidal and thus the converter exhibits reduced power losses and improved efficiency. As an additional benefit, the configuration of the resonant converter integrates bi-directionality and decreased electromagnetic interference.

The LLC resonant converter is a widely used topology in high-power applications due to its high efficiency and low EMI characteristics. It consists of an input inductor, an output inductor, and a resonant capacitor as illustrated in Figure 2.5. The LLC converter topology contains both a half-bridge variant as presented in [17] and a full-bridge configuration as described in [18]. Such converters can also be designed utilizing gallium nitride (GaN) switches to improve their efficiency and power density [19].

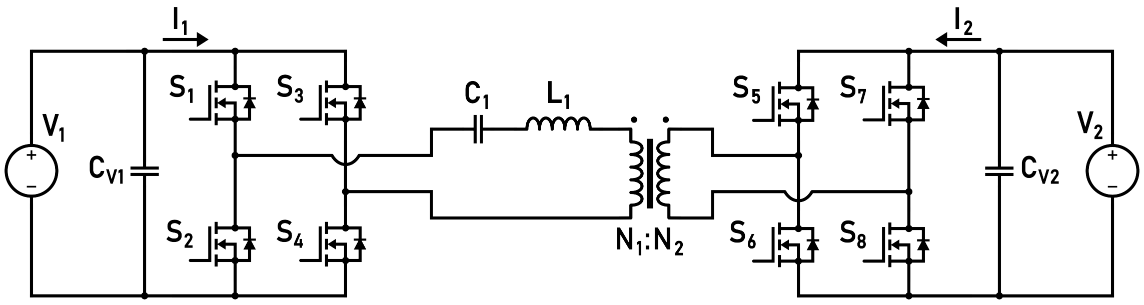

Figure 2.5. Topology of a DC-DC LLC resonant converter.

The CLLC resonant converter is an extension of the LLC topology, and features an additional capacitor, as shown in Figure 2.6, to improve transient response and voltage regulation. This configuration improves perturbation recovery and aids in maintaining stable output under varying load conditions. The main benefit of the CLLC topology over the LLC topology is its improved operation in both forward and reverse mode, and its enhanced efficiency [20]. As with the LLC, the CLLC contains both a half-bridge configuration [21] and a full-bridge configuration, dependent on the desired converter application requirements. The CLLC can also be designed to minimize switching losses while avoiding the use of snubber circuits, as outlined in [22].

The CLLLC resonant converter is a further extension of the previous two topologies, incorporating an additional inductor in series with the tank circuit, as in Figure 2.7. This additional inductor further improves the transient rejection capabilities and enables upgraded precise voltage control. The design of the resonant tank components is achieved utilizing the CLLLC voltage gain equation to meet the desired converter design specifications [23].

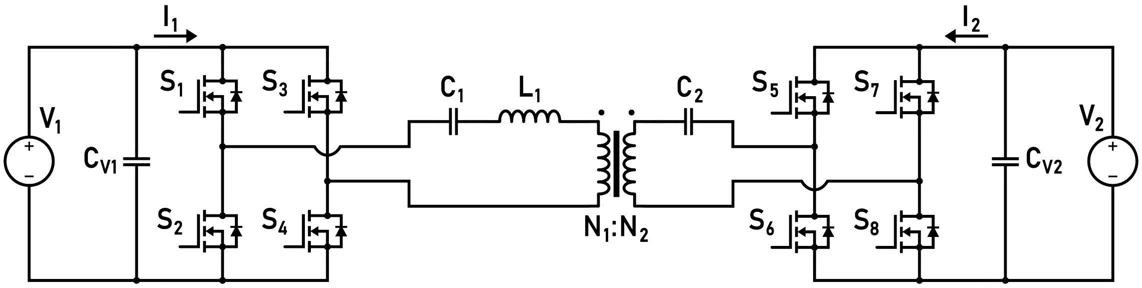

Figure 2.6. Topology of a DC-DC CLLC resonant converter.

The incorporation of soft switching within this converter topology allows for significantly higher frequency operation, and therefore a smaller physical transformer size [24]. Further reduction of the CLLLC converter footprint is possible through utilization of an integrated PCB winding transformer, as developed in [25].

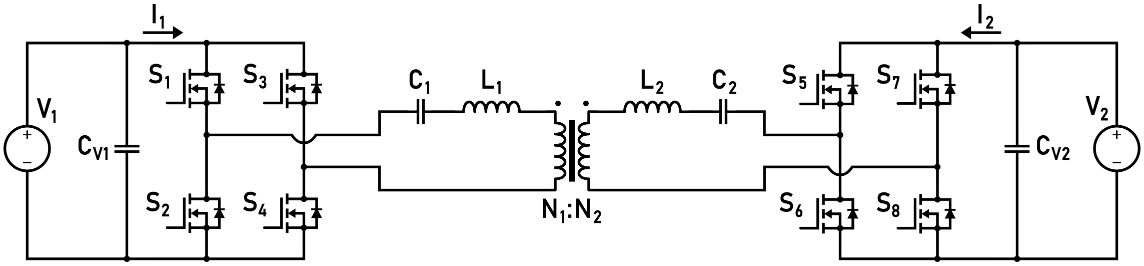

Figure 2.7. Topology of a DC-DC CLLLC resonant converter.

In conclusion, the three aforementioned resonant converter topologies find applications in various high-power and high-frequency systems. Due to their efficient power conversion, voltage regulation, and bi-directional power transfer capabilities, they are an excellent choice for renewable energy grid integration and electric vehicle chargers in both the grid-to-vehicle (G2V) and vehicle-to-grid (V2G) configurations [26].

2.5. TRIPLE ACTIVE BRIDGE

The triple active bridge (TAB) is a sophisticated circuit topology, building upon the antecedent DAB configuration presented in Section 2.3. Comprised of three bridges as shown in Figure 2.8, the TAB offers bi-directional power flow, galvanic isolation, improved flexibility, and power flow control. The magnitude and direction of power transfer is defined based on the phase shift between the switching signals of bridges. Designating bridge 1 as the reference bridge, ϕ_2 is denoted as the phase shift from bridge 1 to bridge 2, and ϕ_3 is expressed as the phase shift from bridge 1 to bridge 3. Although not explicitly defined, the phase shift between bridges 2 and 3, ϕ_{23}, can be calculated through the relationship of $\phi_3 - \phi_2$. Mathematical analysis of this average power was first presented in [27] for one of six specific phase configurations. As with the DAB, the TAB is also typically operated with a constant switching duty cycle of 50%, but can be modulated to further reduce losses [28]. A design methodology for the TAB converter is presented in [29].

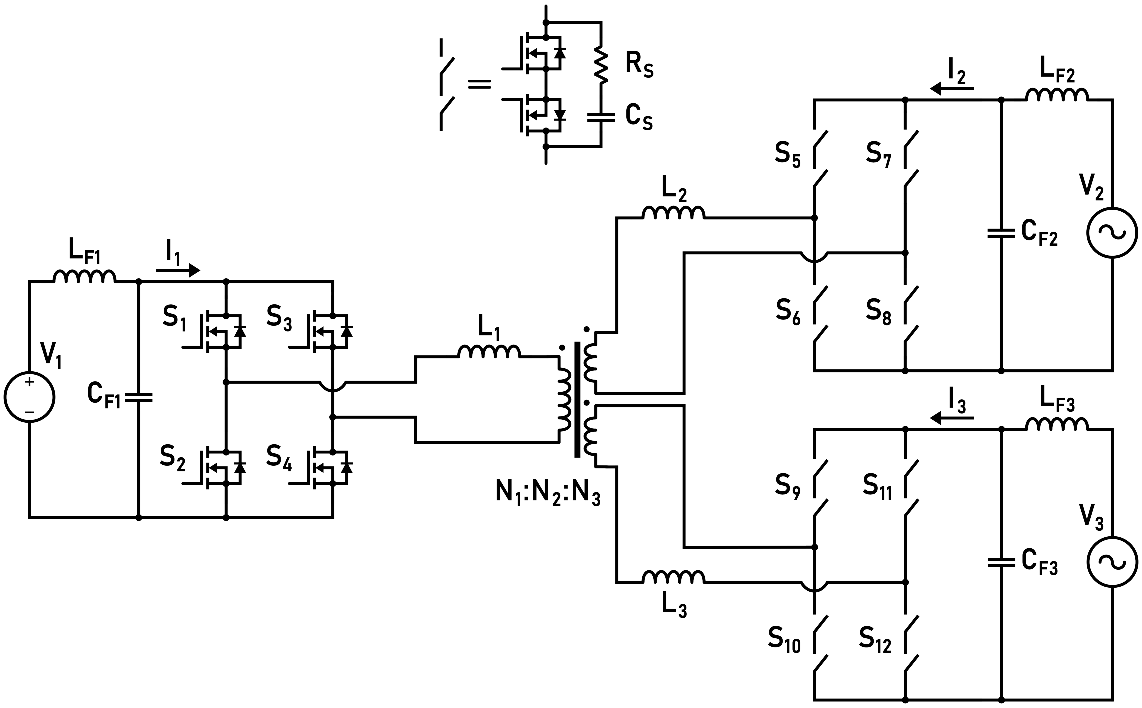

Figure 2.8. Topology of a DC-AC-AC triple active bridge power converter.

Control architectures of the TAB are still being readily developed, including within the composition of this thesis. In the DC-DC-DC case, twelve switches must be controlled for proper operation, and due to the requirement of anti-series switches for blocking AC voltages, twenty switches must be appropriately modulated in the DC-AC-AC case. Because the TAB represents a non-linear system, determining the phase shift values, ϕ_2 and ϕ_3, poses a significant challenge and requires complex control algorithms. One such control strategy, illustrated in [30], attempts to control the transformer current during each switching cycle, effectively reducing the DC transients. An alternate method of TAB control includes supervised machine learning, thereby mitigating the requirement to mathematically identify the desired converter operational point [31]. Depending on the specific application requirements and operating conditions, each control strategy offers unique advantages in terms of efficiency, dynamic response, and stability.

Because the TAB is still a relatively recent circuit topology, little research has been conducted into its implementation with AC sources. One available application utilizes one AC bridge and two DC bridges, specifically designed for charging the batteries of electric vehicles [32]. The TAB can also be implemented in a three-phase AC configuration with two of the bridges being DC. Incorporating a resonant LC tank circuit on the AC bridge, this topology is outlined in [33]. An alternate three-phase configuration, presented in [34], illustrates both of the DC bridges operating in an output series configuration to charge a high-voltage DC battery.

In summary, the TAB can be implemented in various applications including energy storage grid integration [35], microgrids, uninterrupted power supplies, data center power distribution, and electric vehicles or aircraft [36]. Because of its diverse applications, high efficiency, and galvanic isolation, the TAB is an effective choice for improving modern power systems. Its adaptability and efficiency position the TAB for large-scale future integration.

PAPER

I. INSTANTANEOUS CURRENT AND AVERAGE POWER FLOW CHARACTERIZATION OF A DC-DC-DC TRIPLE ACTIVE BRIDGE CONVERTER

Jonathan Saelens, Lauryn Morris, Oroghene Oboreh-Snapps, Arnold Fernandes,
Praneeth Uddarraju, Sophia A. Strathman, Jonathan W. Kimball
Missouri University of Science and Technology, Rolla, MO, USA
Email: jhskrw@mst.edu, lrmdhf@mst.edu, oogdq@mst.edu, af2vc@mst.edu,
pu5mb@mst.edu, ss6k4@mst.edu, kimballjw@mst.edu

ABSTRACT

The Triple Active Bridge (TAB) is a three-port power converter that facilitates bi-directional power flow and provides galvanic isolation, making it a subject of significant research attention. This is attributed to its diverse applications in high-frequency DC-DC conversion, electric vehicles, renewable energy integration, and micro-grids. Controlling the system at run-time involves modification of the two phase-shift parameters between respective bridges. By analyzing the fundamental converter operating equations, future control designers can use this framework to optimize control schemes to mitigate the under-determined nature of the TAB converter. In this paper, we elucidate the foundational operational principles of the TAB and establish the defining equations for instantaneous current and average power flow. Furthermore, we validate these equations through a comparative analysis involving a simulation model of the TAB in PLECS and hardware implementation.

Keywords: Triple Active Bridge, DC-DC Converter, Bi-directional, Power Electronics, Instantaneous Current, Average Power, High Frequency Conversion.

1. INTRODUCTION

The dual active bridge (DAB), a classification of solid-state transformers [1], is a dual H-bridge power converter renowned for its many admirable qualities, including bi-directional power flow capability, high conversion efficiency, galvanic isolation, and low component counts [2], [3]. Its well-understood topology and varied control strategies make it a exceptional and robust candidate for many of today's high-power applications such as electric vehicle chargers and micro-grids [4]. Although the DAB is currently widely used, it's important to note that the single-source single-sink configuration is not sufficient for all use cases. The triple active bridge (TAB), on the other hand, still retains all of these beneficial qualities while improving on the DAB's core structure [5]. Through the inclusion of a third bridge, the TAB allows for either single-source multi-sink or multi-source single-sink, offering adaptability depending on the desired implementation strategy. This enables the TAB to be used in many additional scenarios including modern onboard vehicle chargers, smart grids, and battery storage grid integration [6], [7].

Appropriately controlling the TAB converter requires understanding and analysis of the system's instantaneous current and average power by utilizing their respective equations. The main contribution of this paper is to present these defining TAB system equations, for use in future control schemes, while expanding on existing work presented in [8] and [9]. In Section 2, a brief description of the TAB topology is provided. The proposed equations are then presented with a functional description of their derivation process in Section 3. To verify efficacy, the equations are then compared against simulation and hardware in Section 4 before concluding the paper and presenting a direction for future work in Section 5.

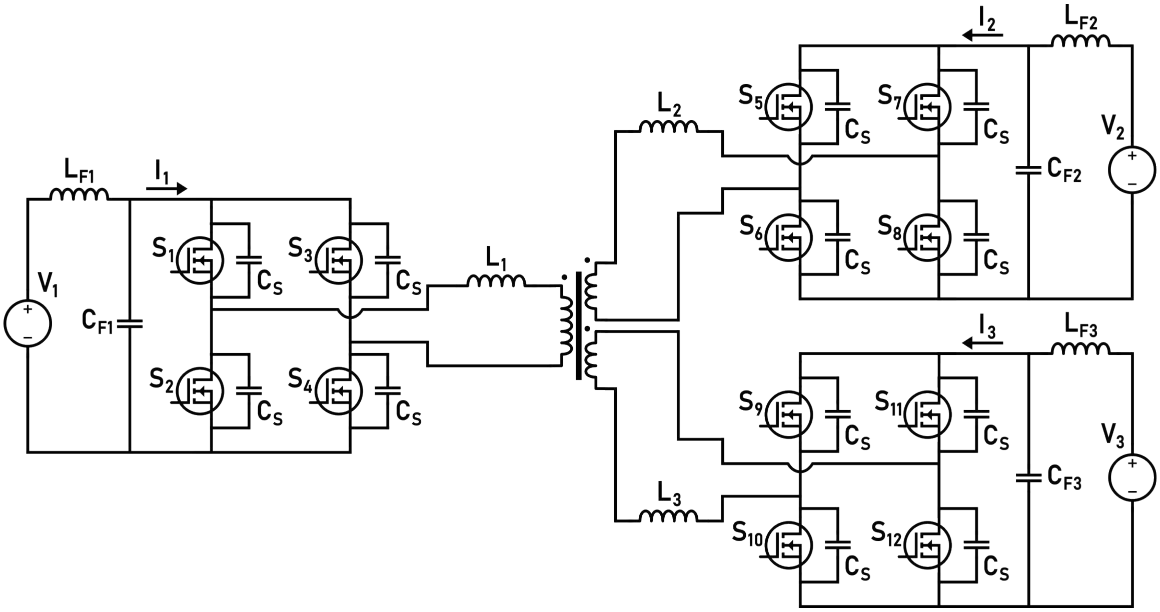

Figure 1. Triple active bridge circuit topology.

2. DC-DC-DC TAB CONVERTER TOPOLOGY

The triple active bridge converter is a three-bridge system that allows bi-directional power flow on each port and galvanic isolation between all ports. The diagram of the topology is available in Figure 1. The TAB consists of three H-bridges connected through a high-frequency three-winding transformer [10]. Each bridge has a leakage inductance L_1, L_2, and L_3, typically incorporated within the transformer itself, that can be tuned to designate the amount of power transfer present throughout the system. In [11], a methodology for determining such inductances and the required transformer turns ratio is presented. The main control parameters, while the TAB is in operation, are the respective phase shift values between bridges, ϕ_2 and ϕ_3. Bridge 1 is designated as the reference bridge and has a phase shift of zero degrees. By modulating these two phase shift parameters, the amount of power transferred between bridges can be calculated as described in Section 3. Further descriptions of the system will be discussed in the proceeding sections.

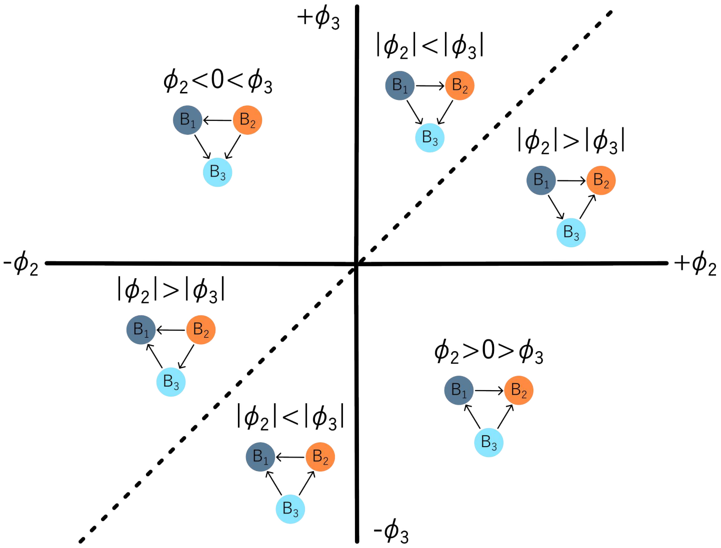

Figure 2. Diagram of six possible phase shift configurations within the TAB and their respective power transfer directions.

3. SYSTEM EQUATIONS

Based on the typical TAB transformer design, the leakage inductance is significantly smaller than the internal magnetizing inductance. To simplify calculations, we can therefore assume that the magnetizing inductance, L_m, is infinite and hence may be ignored. The leakage inductor current is governed by:

$$I(\theta) = \frac{1}{L}\int_0^{\theta} V(\tau)\,d\tau + I(0) \tag{1}$$

To accurately incorporate the transformer turns ratios into the newly proposed equations, illustrating the relationship of translating voltages and inductances between two arbitrary windings, a and b, is necessary. These dependencies are exemplified by:

$$V_a = V_b \frac{N_a}{N_b} \tag{2}$$

$$L_a = L_b \left(\frac{N_a}{N_b}\right)^2 \tag{3}$$

The computation of average power, including a simplified version enabling current waveform analysis, is emphasized by:

$$P = \frac{1}{T}\int_0^T (V(t) \cdot I(t))\,dt \tag{4}$$

$$P = \frac{2V}{T}(A_1 + A_2 + A_3) \tag{5}$$

The incorporation of transformer turns ratios within the average power flow equations allows for more diverse usage scenarios. These ratios, $\frac{N_1}{N_2}$ and $\frac{N_1}{N_3}$, are denoted by n_{12} and n_{13}, respectively. The power flow on each port is given by:

$$P_1 = \frac{V_1V_2\phi_2L_3n_{12}n_{13}^2(\pi - |\phi_2|) + V_1V_3\phi_3L_2n_{12}^2n_{13}(\pi - |\phi_3|)}{2f_s\pi^2(L_1L_2n_{12}^2 + L_1L_3n_{13}^2 + L_2L_3n_{12}^2n_{13}^2)} \tag{6}$$

$$P_2 = \frac{V_2V_1\phi_2L_3n_{12}n_{13}^2(|\phi_2| - \pi) + V_2V_3L_1n_{12}n_{13}(\phi_2 - \phi_3)(|\phi_2 - \phi_3| - \pi)}{2f_s\pi^2(L_1L_2n_{12}^2 + L_1L_3n_{13}^2 + L_2L_3n_{12}^2n_{13}^2)} \tag{7}$$

$$P_3 = \frac{V_3V_1\phi_3L_2n_{12}^2n_{13}(|\phi_3| - \pi) + V_3V_2L_1n_{12}n_{13}(\phi_2 - \phi_3)(\pi - |\phi_2 - \phi_3|)}{2f_s\pi^2(L_1L_2n_{12}^2 + L_1L_3n_{13}^2 + L_2L_3n_{12}^2n_{13}^2)} \tag{8}$$

Instantaneous current for each of the six available phase shift combinations present within the TAB is governed by:

$$I_1 = \frac{A(L_2(V_1Bn_{12}^2 + Hn_{12}^2n_{13}) + L_3(V_1Bn_{13}^2 + Gn_{12}n_{13}^2))}{4\pi \mathrm{f_s}(L_1L_2n_{12}^2 + L_1L_3n_{13}^2 + L_2L_3n_{12}^2n_{13}^2)} \tag{9}$$

$$I_2 = \frac{-A(L_1(Gn_{12}^2 - Hn_{12}n_{13}) + L_3(V_1Bn_{12}n_{13}^2 + Gn_{12}^2n_{13}^2))}{4\pi \mathrm{f_s}(L_1L_2n_{12}^2 + L_1L_3n_{13}^2 + L_2L_3n_{12}^2n_{13}^2)} \tag{10}$$

$$I_3 = \frac{-A(L_1(Hn_{13}^2 - Gn_{12}n_{13}) + L_2(V_1Bn_{12}^2n_{13} + Hn_{12}^2n_{13}^2))}{4\pi \mathrm{f_s}(L_1L_2n_{12}^2 + L_1L_3n_{13}^2 + L_2L_3n_{12}^2n_{13}^2)} \tag{11}$$

Where:

$$\theta = 2\pi \cdot \frac{\mathrm{mod}(t, T)}{T} \tag{12}$$

$$A = \mathrm{sgn}(\pi - \theta) \tag{13}$$

$$B = 2\theta + \pi(\mathrm{sgn}(\pi - \theta) - 2) \tag{14}$$

$$C = A \cdot \mathrm{sgn}(|\phi_2| - \theta) \cdot \mathrm{sgn}(|\phi_2| + \pi - \theta) \tag{15}$$

$$D = A \cdot \mathrm{sgn}(|\phi_3| - \theta) \cdot \mathrm{sgn}(|\phi_3| + \pi - \theta) \tag{16}$$

$$E = A \cdot \mathrm{sgn}(|\phi_2| - \pi + \theta) \cdot \mathrm{sgn}(|\phi_2| - 2\pi + \theta) \tag{17}$$

$$F = A \cdot \mathrm{sgn}(|\phi_3| - \pi + \theta) \cdot \mathrm{sgn}(|\phi_3| - 2\pi + \theta) \tag{18}$$

$$G = \begin{cases} V_2(\pi + C(B + \pi - 2|\phi_2|)) & \phi_2 \geq 0 \\ -V_2E(2(|\phi_2| + \theta) + \pi(A + E - 3)) & \phi_2 < 0 \end{cases} \tag{19}$$

$$H = \begin{cases} V_3(\pi + D(B + \pi - 2|\phi_3|)) & \phi_3 \geq 0 \\ -V_3F(2(|\phi_3| + \theta) + \pi(A + F - 3)) & \phi_3 < 0 \end{cases} \tag{20}$$

4. RESULTS

To delineate the background of the newly proposed equations for instantaneous current and average power flow, this section provides a brief description of the method by which these equations were obtained and provides experimental data to further demonstrate their validity.

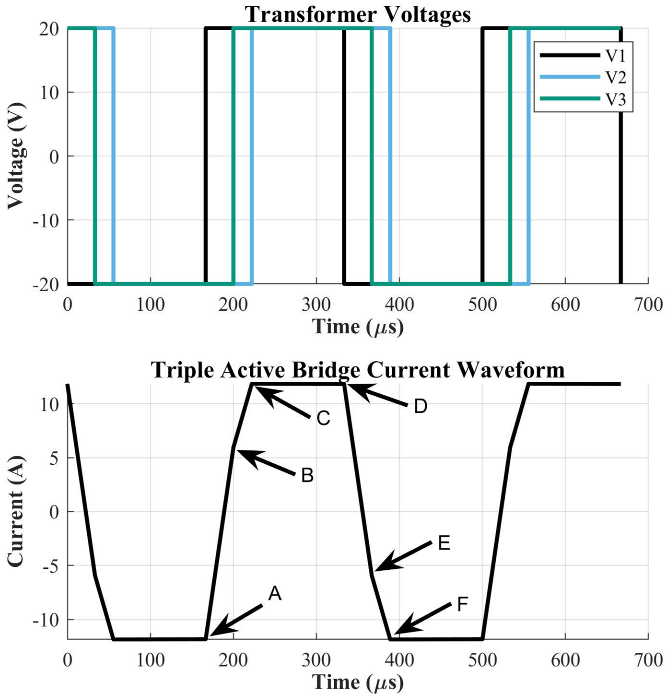

Figure 3. Periodic triple active bridge waveforms. Three-bridge transformer voltages and single-bridge (bridge 1) transformer current.

Switching Frequency	30 kHz
Duty Cycle	50%
Leakage Inductance L_1	12.26μH
Leakage Inductance L_2	7.186μH
Leakage Inductance L_3	18.34μH

Table 1. Default TAB system parameters.

Turns Ratio (N_1:N_2:N_3)	1:1:1
Primary Voltage (V_1)	20V
Secondary Voltage (V_2)	20V
Tertiary Voltage (V_3)	20V

Table 2. Unity transformer TAB system parameters.

Turns Ratio (N_1:N_2:N_3)	1:4:2
Primary Voltage (V_1)	20V
Secondary Voltage (V_2)	80V
Tertiary Voltage (V_3)	40V

Table 3. Non-unity transformer TAB system parameters.

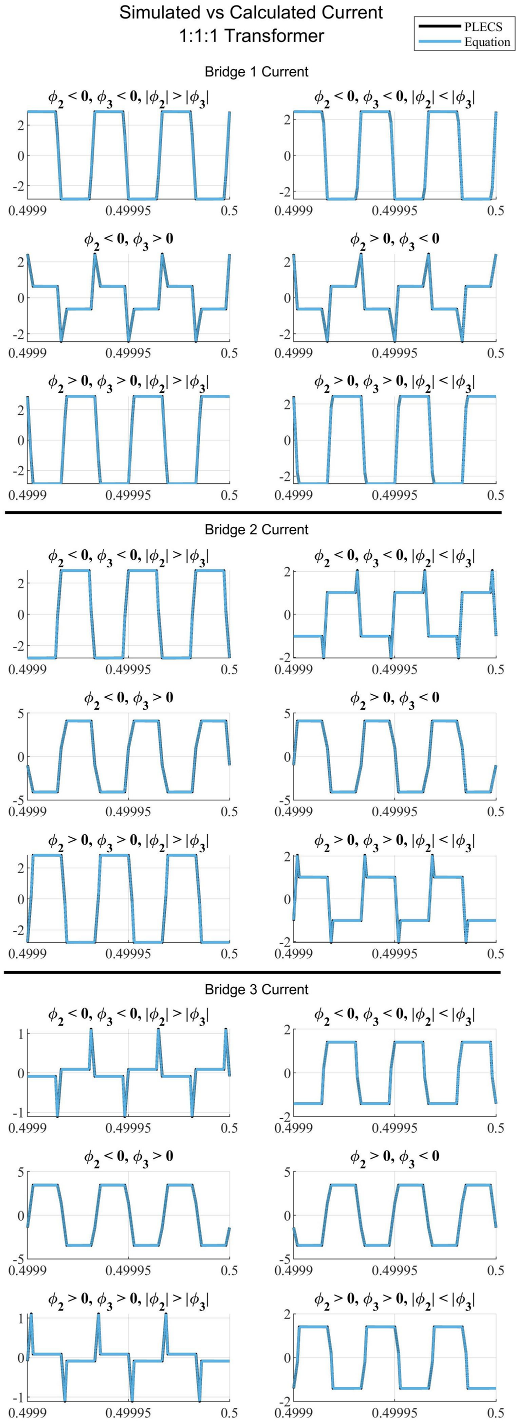

Figure 4. PLECS simulated system current vs calculated equation current with a 1:1:1 transformer ratio. The x-axis corresponds to time in seconds and the y-axis corresponds to current in amps. $T = \frac{1}{30{,}000}$.

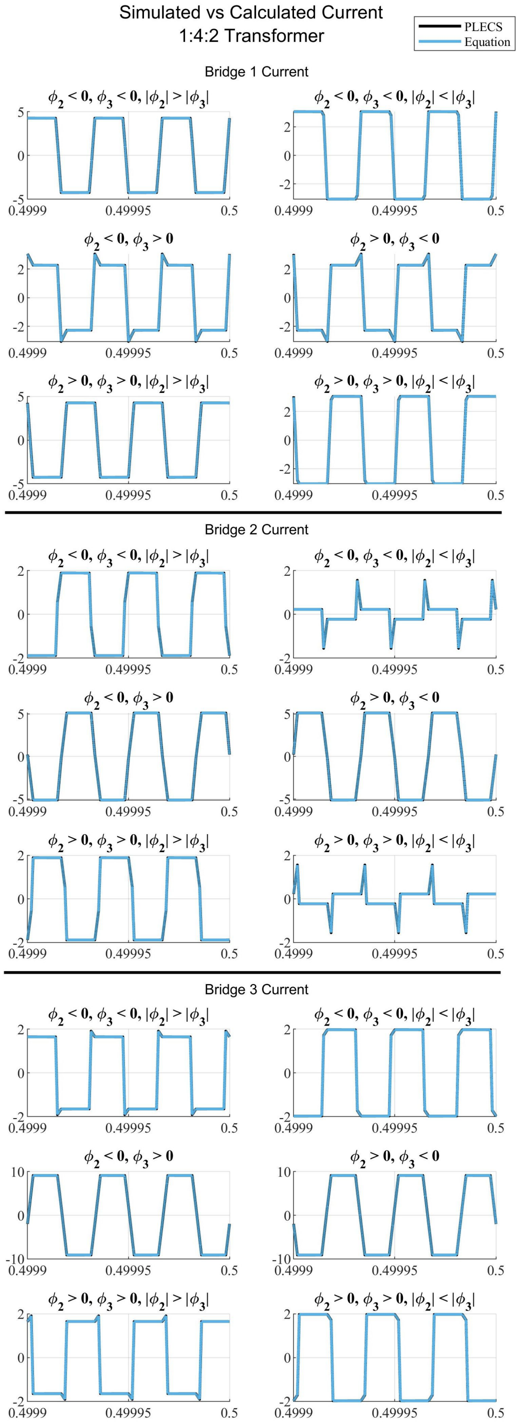

Figure 5. PLECS simulated system current vs calculated equation current with a 1:4:2 transformer ratio. The x-axis corresponds to time in seconds and the y-axis corresponds to current in amps. $T = \frac{1}{30{,}000}$.

4.1. INSTANTANEOUS CURRENT EQUATIONS

The under-determined nature of the TAB produces numerous valid solution combinations of ϕ_2 and ϕ_3. Analyzing the instantaneous current facilitates identifying a single configuration providing higher efficiency or improved converter response. The following analysis will utilize a positive current indicating power flow from the DC port toward the transformer, and a negative current indicating power flow from the transformer toward the DC port. The current waveform of the TAB contains six main segments, referenced in Figure 3, where the current at point A is equal to the negative of the current at point D. Using the inductor current in (1), the instantaneous current at each of these six segments can be defined. In this equation, L is the inductance, V is the inductor voltage, and $I(0)$ is the initial current at $\theta = 0$.

By generating this equation for the first three linear time segments (A→B, B→C, and C→D) and performing substitution so each is dependent on I(A), the first equation evaluated at $\theta = A$ can be equated to the negative of the third equation evaluated at $\theta = D$ and solved for I(A), then substituted back into the original three equations. Repeating this for all phase combinations and bridges yields a multitude of equations, and performing algebraic manipulation, the resulting relationships are available in (9), (10), and (11).

4.1.1. Unity Transformer Case. For many applications within power electronics, a unity, or 1:1:1 turns ratio transformer is used. This allows for safety and noise isolation while not affecting output voltage. For this analysis, general system parameters are defined in Table 1, and the transformer specifications are defined in Table 2. Collecting data for three switching cycles before t = 0.5s to discount startup transients, Figure 4 demonstrates that the PLECS simulations and the computed current equations line up identically thus validating the current equations for all phase combinations in Figure 2.

4.1.2. Non-Unity Transformer Case. In many realistic applications, the same voltage magnitude on all bridges may not be desired. Because the duty cycle is not being modulated, the transformer turns ratio impacts the voltages. To incorporate the transformer turns ratios into the instantaneous current equations, voltages and inductances must be translated across a three-winding transformer. From the b winding to the a winding, the transfer is exemplified by (2) and (3), respectively. By including (2) and (3), it is possible to characterize the instantaneous current using any set of transformer turns ratios.

Utilizing the constant system parameters outlined in Table 1 and the non-unity transformer specifications defined in Table 3, Figure 5 illustrates that the simulated PLECS current and calculated equation current line up analogously.

4.1.3. Hardware Verification. The hardware setup consists of system elements defined in Table 1 and Table 2. A photo of the complete setup is shown in Figure 7. Because physical hardware incorporates non-idealistic elements that are not easily modeled through circuit simulation, it is expected to encounter slight deviations or signal ringing within the current waveforms. When comparing the graph presented in Figure 6 to the waveforms for $\phi_2 > 0,\ \phi_3 > 0,\ |\phi_2| < |\phi_3|$ in Figure 4, it can be seen that both possess similarities in waveform shape.

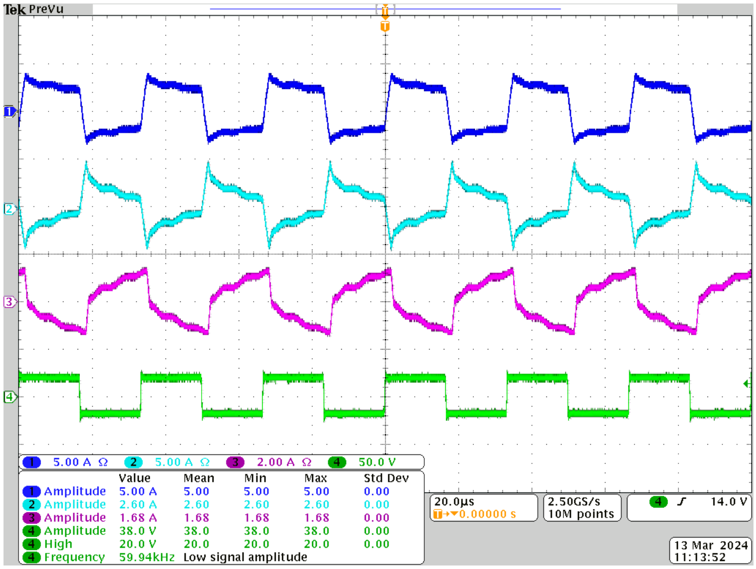

```
              Value     Mean   Min    Max    Std Dev
1 Amplitude   5.00 A    5.00   5.00   5.00   0.00
2 Amplitude   2.60 A    2.60   2.60   2.60   0.00
3 Amplitude   1.68 A    1.68   1.68   1.68   0.00
4 Amplitude   38.0 V    38.0   38.0   38.0   0.00
4 High        20.0 V    20.0   20.0   20.0   0.00
4 Frequency   59.94kHz  Low signal amplitude
```

Figure 6. Instantaneous current TAB waveforms. Top to bottom: dark blue = bridge 1 current, light blue = bridge 2 current, pink = bridge 3 current, green = bridge 1 transformer voltage. $\phi_2 = 20°$, $\phi_3 = 30°$.

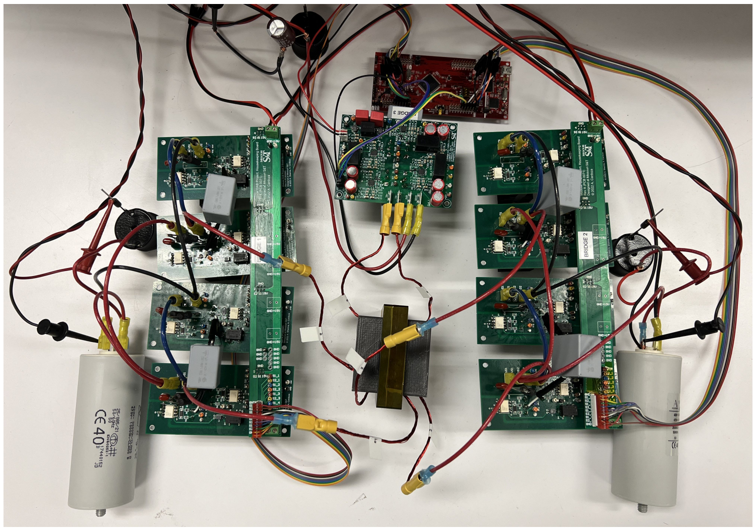

Figure 7. DC-DC-DC TAB hardware test setup.

4.2. POWER FLOW EQUATIONS

In a TAB, the power flowing through the system is characterized by the amount of power at one specific bridge, where a positive value indicates a power source and a negative value indicates a power sink. Based on the system configuration, the only atributes that can be modified while the converter is in operation are the phase shift parameters, ϕ_2 and ϕ_3. By using the quantity of desired power, the average power flow equations can be used to determine a possible configuration for ϕ_2 and ϕ_3 to meet demands.

Using P_1 as an example, the average power between P_1 and P_2 and then P_1 and P_3 are calculated using the general average power equation provided in (4) and then added versus analyzing the power due to all three bridges simultaneously. Since the power transfer in the first half of the switching cycle is equal to that in the second half, we can compute the average power by multiplying the integral of the first three time segments (from point A to point D) by the voltage and dividing by the time period, as in (5). Repeating this process for each of the bridges and phase combinations will yield a comprehensive list of defining equations. After further simplification and combination, these equations have been reduced and are indicated in (6), (7), and (8).

In an ideal system, the efficiency of any converter is equal to 100%. As an initial equation verification step, it is important to note that due to the conservation of power, computing the sum of P_1, P_2, and P_3, should result in a net value of zero. Summing (6), (7), and (8) yields this expected result.

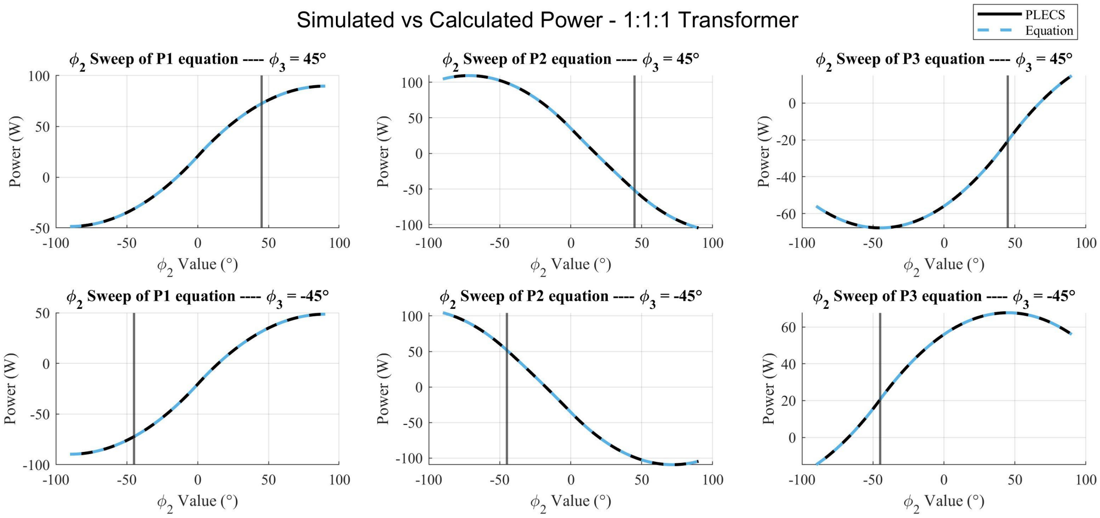

Figure 8. Sweep of ϕ_2 parameter comparing PLECS simulated power vs calculated equation power with varying ϕ_3 values for a 1:1:1 transformer ratio.

4.2.1. Unity Transformer Case. To perform analysis on the average power equations, a parameter sweep for ϕ_2 was used rather than a time-dependent signal shown in the instantaneous current case. Utilizing the same system parameters, the graphs in Figure 8 illustrate a sweep of ϕ_2 while keeping ϕ_3, the vertical line, constant. For all measured values of ϕ_2, the resulting equations exactly match the PLECS simulation outputs.

4.2.2. Non-Unity Transformer Case. When considering the non-unity transformer case, it is imperative that the power flow equations continue to hold to enable calculation of the phase shift parameters, ϕ_2 and ϕ_3. Using PLECS to measure simulated average system power and plotting these values against the newly proposed average power flow equations, the results, employing the same non-unity system parameters as before, can be seen in Figure 9. All of the simulated PLECS waveforms precisely match the equations.

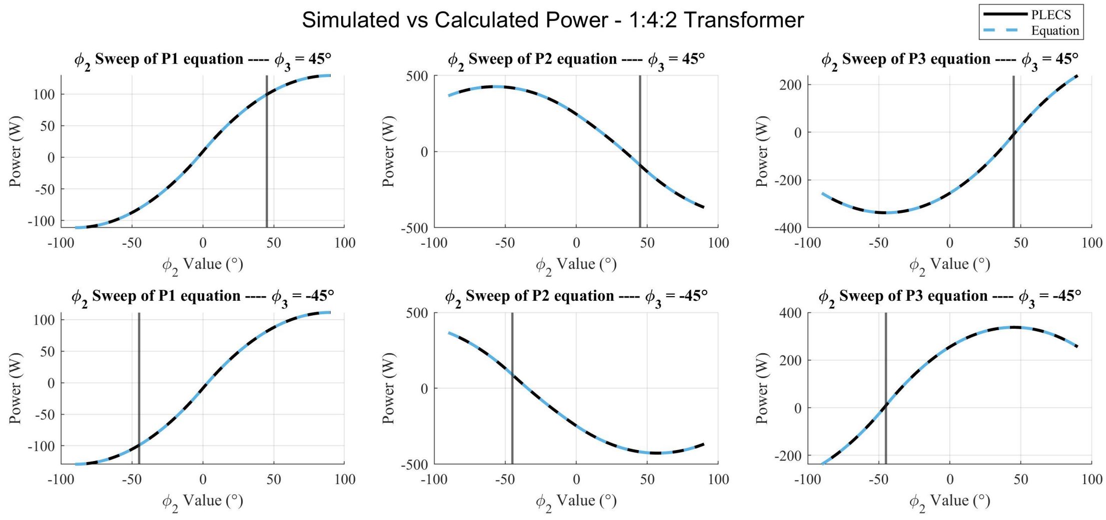

Figure 9. Sweep of ϕ_2 parameter comparing PLECS simulated power vs calculated equation power with varying ϕ_3 values for a 1:4:2 transformer ratio.

4.2.3. Comparison to Previous Work. In a typical triple active bridge application, following [8], bridge 1 is usually considered the primary source, with power also flowing from bridge 3 to bridge 2. This is dictated by positive phase shift values for both ϕ_2 and ϕ_3, and ϕ_2 being greater than ϕ_3. While scenarios where bridge 1 is a source and bridge 3 is either a source or sink are explored in [9], such cases limit the bi-directional capabilities of the TAB. To address this limitation, the newly proposed equations, accommodating all six modes of operation presented in Figure 2, extend beyond the scope of previous studies. Unlike equations in [8], the updated mathematical formulations in (6), (7), and (8) incorporate transformer turn ratios, crucial for a comprehensive analysis.

Figure 10, with a unity transformer, illustrates that the previous equations from [8] hold true only when $\phi_2 > \phi_3$. Conversely, the introduced equations consistently match PLECS results across the entire range of ϕ_2 values, irrespective of ϕ_3. Employing different transformer turn ratios reveals a stark divergence, where the previous equations deviate significantly from the simulated PLECS curve, while the presented mathematical expressions maintain their expected behavior.

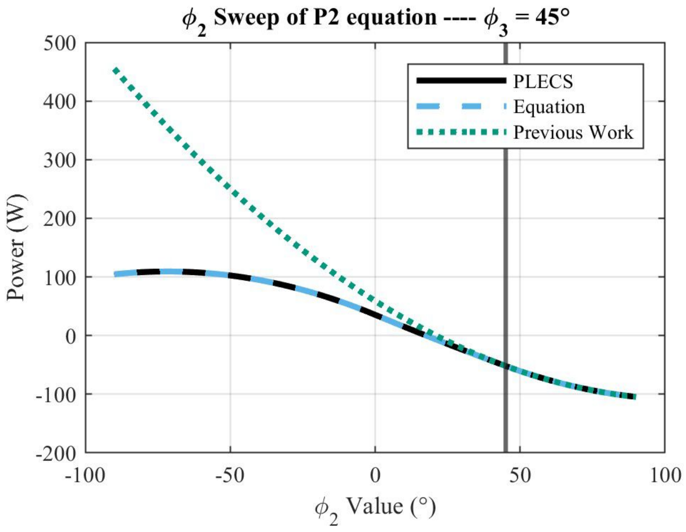

Figure 10. Comparison of P_2 equation of PLECS output vs newly proposed equations vs previous work.

5. CONCLUSION

The triple active bridge is a sophisticated power converter containing a wide array of system variables. Through the examination provided above, a set of defining equations for both instantaneous current and average power have been presented which encompass all possibilities of transformer turns ratios and phase configurations. Their efficacy has been validated through analysis of PLECS simulations and hardware implementation. Presenting a direction for future work includes developing an appropriate control strategy for effectively calculating phase shift parameters ϕ_2 and ϕ_3. In addition, adaptation of the presented equations to allow for one or more bridges to interface with AC rather than solely DC would allow for more diverse converter applications.

REFERENCES

[1] Xu She, Alex Q. Huang, and Rolando Burgos. Review of solid-state transformer technologies and their application in power distribution systems. *IEEE Journal of Emerging and Selected Topics in Power Electronics*, 1(3):186–198, 2013. doi: 10.1109/JESTPE.2013.2277917.

[2] Hengsi Qin and Jonathan W. Kimball. Solid-state transformer architecture using ac–ac dual-active-bridge converter. *IEEE Transactions on Industrial Electronics*, 60(9): 3720–3730, 2013. doi: 10.1109/TIE.2012.2204710.

[3] Kartikeya Jp Veeramraju, Angshuman Sharma, and Jonathan W. Kimball. A comprehensive analysis on complex power flow mechanism in an ac-ac dual active bridge. In *2022 IEEE Power and Energy Conference at Illinois (PECI)*, pages 1–6, 2022. doi: 10.1109/PECI54197.2022.9744009.

[4] Angshuman Sharma, Kartikeya Jp Veeramraju, and Jonathan W. Kimball. Power flow control of a single-stage ac-ac solid-state transformer for ac distribution system. In *2022 IEEE Power and Energy Conference at Illinois (PECI)*, pages 1–6, 2022. doi: 10.1109/PECI54197.2022.9744006.

[5] Subhradip Mukherjee and Indrajit Sarkar. A brief review on triple active bridge dc-dc converter. In *2023 IEEE International Students' Conference on Electrical, Electronics and Computer Science (SCEECS)*, pages 1–6, 2023. doi: 10.1109/SCEECS57921.2023.10063031.

[6] Shenli Zou, Jiangheng Lu, Ayan Mallik, and Alireza Khaligh. Modeling and optimization of an integrated transformer for electric vehicle on-board charger applications. *IEEE Transactions on Transportation Electrification*, 4(2):355–363, 2018. doi: 10.1109/TTE.2018.2804328.

[7] Viju Nair R., Srinivas Gulur, Ritwik Chattopadhyay, and Subhashish Bhattacharya. Integrating photovoltaics and battery energy storage to grid using triple active bridge and voltage source converters. In *IECON 2020 The 46th Annual Conference of the IEEE Industrial Electronics Society*, pages 3691–3696, 2020. doi: 10.1109/IECON43393.2020.9255053.

[8] Chuanhong Zhao, Simon D. Round, and Johann W. Kolar. An isolated three-port bidirectional dc-dc converter with decoupled power flow management. *IEEE Transactions on Power Electronics*, 23(5):2443–2453, 2008. doi: 10.1109/TPEL.2008.2002056.

[9] Ritwik Chattopadhyay, Sayan Acharya, Ghanshyamsinh Gohil, and Subhashish Bhattacharya. One switching cycle current control strategy for triple active bridge phase-shifted dc-dc converter. In *2017 IEEE Industry Applications Society Annual Meeting*, pages 1–8, 2017. doi: 10.1109/IAS.2017.8101785.

[10] Babak Rahrovi, Ramin Tafazzoli Mehrjardi, and Mehrdad Ehsani. On the analysis and design of high-frequency transformers for dual and triple active bridge converters in more electric aircraft. In *2021 IEEE Texas Power and Energy Conference (TPEC)*, pages 1–6, 2021. doi: 10.1109/TPEC51183.2021.9384990.

[11] Venkateswara Rao Kudaravalli, Vishwabandhu Uttam, and Vishnu Mahadeva Iyer. A design methodology for triple active bridge dc- dc converter. In *2022 IEEE International Conference on Power Electronics, Drives and Energy Systems (PEDES)*, pages 1–7, 2022. doi: 10.1109/PEDES56012.2022.10080029.

II. FEED-FORWARD CONTROL ALGORITHM DESIGN AND PERFORMANCE ANALYSIS FOR A DC-DC-DC TRIPLE ACTIVE BRIDGE CONVERTER

Jonathan Saelens, Graduate Student Member, IEEE,
Lauryn Morris, Graduate Student Member, IEEE,
Oroghene Oboreh-Snapps, Graduate Student Member, IEEE,
Praneeth Uddarraju, Graduate Student Member, IEEE,
Arnold Fernandes, Graduate Student Member, IEEE, Sophia A.
Strathman, Student Member, IEEE, and Jonathan W. Kimball, Senior Member, IEEE

Missouri University of Science and Technology, Rolla, MO, USA
Email: jhskrw@mst.edu, lrmdhf@mst.edu, oogdq@mst.edu, af2vc@mst.edu,
pu5mb@mst.edu, ss6k4@mst.edu, kimballjw@mst.edu

ABSTRACT

Power electronic converters are vital to facilitating the integration of renewable energy systems into the electrical grid and keeping up with the widespread electrification demands. One such topology gaining significant research attention is the Triple Active Bridge (TAB). The TAB is a power converter containing three ports to allow for the incorporation of various sources and loads. Its modular topology allows for the facilitation of bidirectional power flow and provides galvanic isolation between ports. Positioned at the forefront of innovation, the TAB finds applications in high-frequency DC-DC conversion, electric vehicles, renewable energy integration, and micro-grids. This research paper primarily delves into the development and analysis of a power-based control algorithm, leveraging the Newton-Raphson method to derive a linear approximation for the governing set of non-linear power flow equations. Practical validation of the proposed control architecture occurs in both PLECS circuit simulation and a physical TAB prototype, allowing a comparative analysis between simulation and real-world results. The emergence of this algorithm contributes to the evolving field of power electronics by providing a systematic approach to the implementation of the triple active bridge, offering valuable insights into the real-world applicability and enhanced performance.

Keywords: Triple Active Bridge, AC-AC Converter, DC-DC Converter, DC-AC-AC Converter, Bi-directional, Power Electronics, High Frequency Conversion, Power Flow Control.

1. INTRODUCTION

Existing 60 Hz transformers positioned in large distribution systems and adjacent to buildings have been utilized for many years due to their simplicity and overall widespread adoption. More recently, solid-state transformers (SSTs) have begun to replace these existing transformers due to their unique benefits. The main premise of an SST is to replicate the existing functionality of a 60 Hz transformer by incorporating a significantly higher isolation frequency [1]. By largely increasing the isolation frequency to tens or hundreds of kilohertz (kHz), the size of the converter can be substantially decreased. Further SST size reduction can be achieved through proposed novel transformer design methods, as illustrated in [2], with a litz wire transformer developed within a six-layer PCB. In addition, an SST can also be used to adjust the power quality or enable power flow control [3].

One such type of SST, the dual active bridge (DAB), stands out for its commendable features, encompassing bi-directional power flow, high conversion efficiency, galvanic isolation, and a streamlined component count [4], [5]. Its well-established structure and diverse control strategies position it as an excellent and robust choice for various high-power applications such as electric vehicle chargers and micro-grids [6]. While the DAB enjoys widespread usage, it's crucial to recognize that the single-source single-sink configuration may not suffice for all scenarios. In contrast, the triple active bridge (TAB) maintains the advantageous traits of the DAB while enhancing its fundamental structure [7]. By incorporating a third bridge, the TAB introduces the flexibility of supporting multiple configurations while adapting to diverse implementation strategies such as smart grids, contemporary onboard vehicle chargers, the integration of battery storage elements into the grid [8], [9], and electric vehicles or aircraft [10].

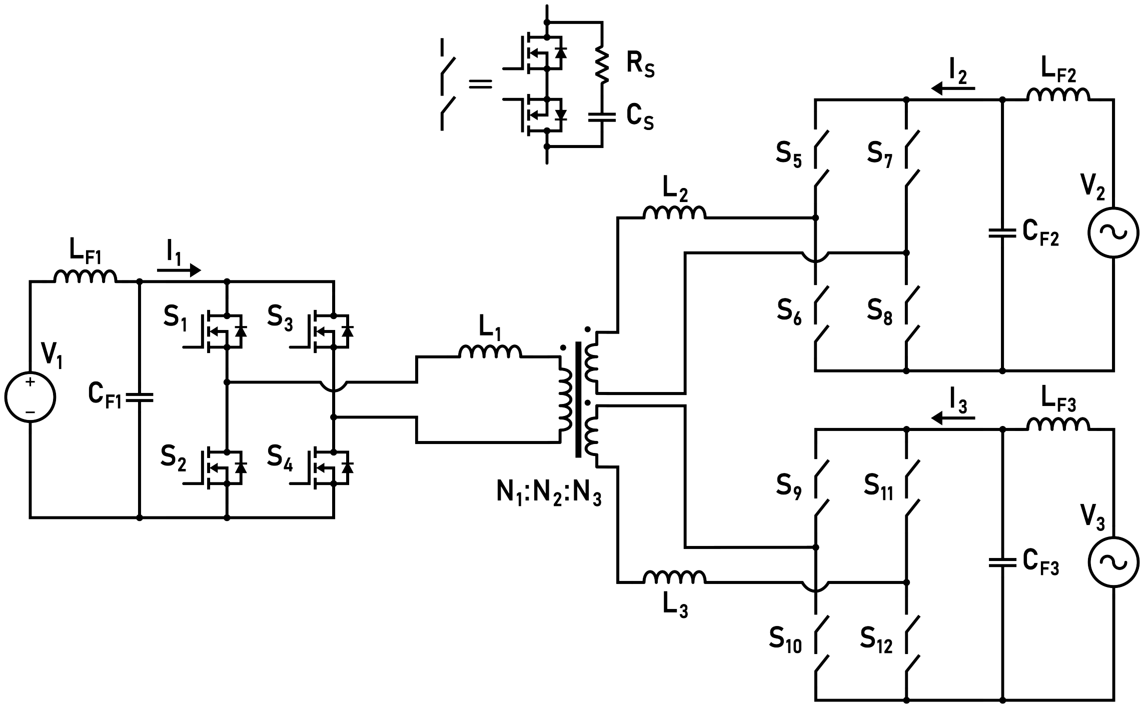

Figure 1. Topology of a DC-AC-AC triple active bridge power converter.

In addition to the DAB, several other main converter topologies exist, including the multilevel H-bridge, phase-shifted full bridge, and various resonant converters. The multilevel H-bridge is a topology consisting of multiple H-bridge segments connected in an output series configuration. Due to its many stages, this converter is capable of enabling voltage regulation and producing multiple output levels [11]. The main advantages of the multilevel H-bridge are its improved output waveform quality, high modularity, and reduced voltage stresses across individual components. Typical applications include photovoltaic inverters, active power filters, and three-phase motor drives [12]. The phase-shifted full bridge is comparable to the DAB, except that the output bridge is a passive one consisting of four diodes arranged in a rectification pattern. By modulating the phase shift between the two legs of the active input H-bridge, the quantity of power transfer is adjusted [13]. Its advantages include galvanic isolation for safety purposes, a comparably simplistic control requirement, and high efficiency. The phase-shifted full bridge converter finds applications in electric vehicle chargers, uninterruptible power supplies, and high-power motor drives. The resonant converter has three main variants, depending on the configuration of inductors and capacitors placed between the two bridges. These include the LLC, the CLLC, and the CLLLC. The LLC converter topology can be constructed using a half-bridge, [14], or a full-bridge configuration, [15]. The CLLC, an extension of the LLC converter, incorporates an additional capacitor allowing for improved operation in forward and reverse mode for greater efficiency [16]. The CLLLC is a further extension of the previous two and features improved transient rejection capabilities and allows for finer output voltage control [17].

Each of these previously discussed topologies has independent strengths and weaknesses, making them suitable for more specific applications. The TAB, however, is a topology more suited for diverse implementation spaces. It consists of three interconnected active bridges joined through a high-frequency three winding transformer. Since all bridges contain active switches, power may be transferred between sources and loads in six possible directions as exemplified in Figure 2. The main advantages boasted by the TAB include high efficiency, bidirectional power flow, implementation flexibility, and improved power density. Although the TAB is generally significantly more complex in terms of control and operation than some of the other previously mentioned topologies, its wealth of advantages position it as a topology gaining significant traction in the field of power electronics.

Because the TAB is such a complex converter and implements a non-linear system, elaborate control methodologies are required for proper operation. In addition, the interdependence of power sharing between the three ports further complicates the matter. While these control strategies are still being readily developed, including within this paper, a few notable ones have come to light. Illustrated in [18], an architecture to control the transformer current during each switching cycle is presented. The current is sampled in one switching cycle and the switching commands are generated for application in the next switching cycle. Another method implements supervised machine learning to train the converter to improve transmission power efficiency [19]. This method mitigates the need to mathematically derive the controller operating parameters, instead requiring operational data to train a model. Additionally, a strategy for controlling the power flow with closed-loop feedback and load balancing is presented in [20].

Each of these aforementioned control strategies, while effective at obtaining the desired output, presents challenges when it comes to implementation complexity and efficiency. Another method of control is through direct analysis of the system's average power equations. Because these equations constitute a non-linear set, a more complex control algorithm is needed to properly determine the phase shift values, ϕ_2 and ϕ_3. Rather than the computationally burdensome approach of directly computing the solution to a set of non-linear equations, an iterative linearization approach will be employed, fundamentally derived from the Newton-Raphson method. Additionally, the algorithm will initially validate the desired power flow quantity and set unattainable requests to zero to ensure converter safety. Once the maximum iteration count has been reached, or algorithmic convergence has been achieved, the computation is concluded and the microcontroller returns to perform alternate tasks. Overall, the control strategy aims to minimize power sharing error while maintaining computation that can be completed within one converter switching cycle of the F28377S C2000 TI Launchpad microcontroller.

The main contributions of this research work are as follows:

1. The proposed control algorithm is an efficient yet accurate feed-forward strategy for calculating the two phase shift parameters between respective bridges, ϕ_2 and ϕ_3, in a triple active bridge converter.

2. This work is focused on pioneering the fundamental challenge of enabling the TAB to function accurately and reliably. While most other research studies typically attempt to improve a specific aspect of the converter such as performance or control efficiency, this approach addresses the core functionality of converter operation in multiple applications.

3. The proposed control algorithm can be easily adapted for implementation on differing hardware configurations of DC and AC bridges. In this paper, the DC-DC-DC and DC-AC-AC cases are presented.

By ensuring effective power transfer among all three bridges, the proposed implementation incorporates the groundwork necessary to facilitate future advancements and applications of the TAB. In Section 2, a concise depiction of the TAB topology and its defining average power equations is outlined. The newly introduced control strategy takes center stage in Section 3, where its algorithm and intricacies are thoroughly examined. An efficiency analysis is then conducted for the proposed algorithm in Section 4. Following this, the proposed control approach undergoes practical implementation within a PLECS model and in hardware to validate its efficacy in the DC-DC-DC case in Section 5. Transitioning two of the bridges to AC sources, the control algorithm is then vetted once again through a DC-AC-AC hardware prototype in Section 6. The paper concludes by summarizing findings and outlining avenues for future research in Section 3. Lastly, the appendix in Section 8 illustrates a general overview of the design process for the physical TAB prototype.

2. TRIPLE ACTIVE BRIDGE CONVERTER TOPOLOGY

The triple active bridge converter constitutes a trilateral system facilitating bidirectional power flow on every port while ensuring galvanic isolation among them. For all instances within this paper, the area of source connection is referred to as the port and the H-bridge and transformer connection constitute the bridge. An illustration of the topology of the converter can be viewed in Figure 1. Comprised of three H-bridges interconnected through a high-frequency three-winding transformer [21], the TAB incorporates three leakage inductances L_1, L_2, and L_3, typically embedded within the transformer itself. These inductances can be finely tuned to specify the power transfer distribution within the system, and can also be implemented as separate elements. A design methodology for the TAB converter parameters and the transformer specifications is presented in [22].

A relatively simplistic TAB topology includes three DC ports and only contains high-frequency AC square waves at the three-winding transformer. It is this topology that will be initially utilized to substantiate the proposed control algorithm. A more complex topology and the specific implementation of the TAB utilized for the ultimate goal of this research project incorporates two AC bridges and one DC bridge. The typical operating point of the converter is transmitting a desired quantity of active and reactive power from AC bridge 2 to AC bridge 3, although the converter can also operate bidirectionally if desired. As illustrated in [5], utilizing a dual active bridge (DAB) with two AC ports is not sufficient for providing a purely sinusoidal current and power output signal when reactive power transfer is desired. This is mainly due to the inability to transfer current from the input bridge to the output bridge surrounding the voltage zero crossings. The phase shift parameter becomes saturated and thus the converter can no longer deliver additional resources. Adding in a third DC bridge can allow compensation for the inefficiencies of the input AC bridge. Additionally, unique to the AC bridges, back-to-back MOSFET pairs are required to block current during the negative half cycle of the input waveform.

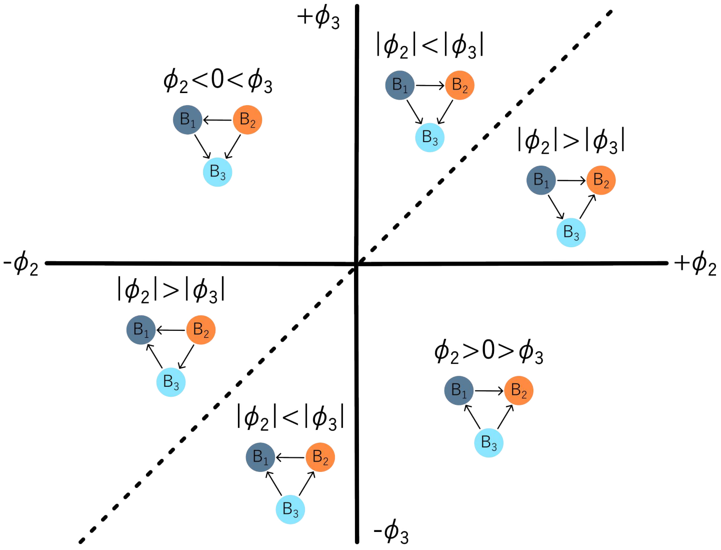

Figure 2. Diagram of six possible phase shift configurations within the TAB and their respective power transfer directions.

$$-\frac{\pi}{2}+\epsilon \leq \phi_2 \leq \frac{\pi}{2}-\epsilon \tag{1}$$

$$-\frac{\pi}{2}+\epsilon \leq \phi_3 \leq \frac{\pi}{2}-\epsilon \tag{2}$$

Throughout TAB operation, pivotal control parameters include the phase shift values between bridges, denoted as ϕ_2 and ϕ_3. ϕ_2 is described as the phase shift between bridges 1 and 2, and ϕ_3 is the phase shift between bridges 1 and 3. Notably, bridge 1 serves as the reference bridge, maintaining a zero-degree phase shift. The modulation of these phase shift parameters allows for the precise control of power transfer among bridges, a process elucidated by the equations detailed in Section 2.1. The phase shift values, ϕ_2 and ϕ_3, are bounded by (1) and (2), with ϵ being a safety margin chosen to be 0.04 in our case. These bounds are enforced to ensure normal operation, as exceeding these constraints may lead to system instability, increased component stresses, or reduced efficiency.

The TAB has six possible modes of operation, dependent on the configuration of ϕ_2 and ϕ_3. These six modes are depicted in Figure 2. While only the phase shift parameters ϕ_2 and ϕ_3 are specified, there is also a relationship concerning the phase shift present between bridges 2 and 3. This phase shift, denoted as ϕ_{23}, is exemplified by:

$$\phi_{23} = \phi_3 - \phi_2 \tag{3}$$

Due to the interdependence of all three bridges, a modification of ϕ_2, for example, does not simply modify the power flow on ports 1 and 2. It also adjusts the power flow on port 3 as well, specifically due to the value of ϕ_{23}. This linkage presents mathematical challenges in determining appropriate values of ϕ_2 and ϕ_3 given the desired quantity of power transfer. Also important to note are the conditions in which maximum power transfer is achieved to a specific bridge. This occurs at the values of ϕ_2 and ϕ_3 illustrated in the following relationships:

Maximum power transfer to bridge 1 occurs at:

$$\phi_2 = -\frac{\pi}{2} + \epsilon, \qquad \phi_3 = -\frac{\pi}{2} + \epsilon \tag{4}$$

Maximum power transfer to bridge 2 occurs at:

$$\phi_2 = \frac{\pi}{2} - \epsilon, \qquad \phi_3 = -\epsilon \tag{5}$$

Maximum power transfer to bridge 3 occurs at:

$$\phi_2 = -\epsilon, \qquad \phi_3 = \frac{\pi}{2} - \epsilon \tag{6}$$

2.1. SYSTEM EQUATIONS

The most important component of the triple active bridge converter is being able to quantify the power being transferred throughout each of the three bridges. A positive quantity of P_1, P_2, or P_3 indicates a power source and a negative quantity indicates a power sink. Appropriate control of the system would prove to be quite challenging without this knowledge and outlines the necessity for defining relationships. As outlined in [23], the power flow on each of the three bridges of the TAB is governed by:

$$P_1 = \frac{V_1 V_2 \phi_2 L_3 n_{12} n_{13}^2 (\pi - |\phi_2|) + V_1 V_3 \phi_3 L_2 n_{12}^2 n_{13} (\pi - |\phi_3|)}{2 f_s \pi^2 (L_1 L_2 n_{12}^2 + L_1 L_3 n_{13}^2 + L_2 L_3 n_{12}^2 n_{13}^2)} \tag{7}$$

$$P_2 = \frac{V_2 V_1 \phi_2 L_3 n_{12} n_{13}^2 (|\phi_2| - \pi) + V_2 V_3 L_1 n_{12} n_{13} (\phi_2 - \phi_3)(|\phi_2 - \phi_3| - \pi)}{2 f_s \pi^2 (L_1 L_2 n_{12}^2 + L_1 L_3 n_{13}^2 + L_2 L_3 n_{12}^2 n_{13}^2)} \tag{8}$$

$$P_3 = \frac{V_3 V_1 \phi_3 L_2 n_{12}^2 n_{13}(|\phi_3| - \pi) + V_3 V_2 L_1 n_{12} n_{13}(\phi_2 - \phi_3)(\pi - |\phi_2 - \phi_3|)}{2 f_s \pi^2 (L_1 L_2 n_{12}^2 + L_1 L_3 n_{13}^2 + L_2 L_3 n_{12}^2 n_{13}^2)} \tag{9}$$

$$P_1 + P_2 + P_3 = 0 \tag{10}$$

In (7), (8), and (9) above, V_1, V_2, V_3, L_1, L_2, and L_3 are the voltages and leakage inductances at bridges 1, 2, and 3, respectively. The transformer turns ratio of $\frac{N_1}{N_2}$ and $\frac{N_1}{N_3}$ are denoted by n_{12} and n_{13}, respectively. ϕ_2 is the phase shift between bridges 1 and 2, ϕ_3 is the phase shift between bridges 1 and 3, and f_s is the switching frequency of the converter. Also, since the ideal case of the converter indicates a conservative system, the summation of power at each of the bridges should add up to zero, as exemplified in (10).

3. PROPOSED ALGORITHM

When only specifying the desired power at a single bridge of the TAB, there are multiple solutions of ϕ_2 and ϕ_3 which can be used to obtain that result. To address this, enumerating power at any two bridges becomes crucial, and the power at the third bridge can be identified utilizing (10). This will reduce the number of solutions to one, contingent on the fact that the desired power transfer is feasible given the hardware elements and phase shift constraints. Examining the power flow relationships presented in (7), (8), and (9), it becomes evident that these equations are non-linear and do not have a straightforward solution method. There are multiple approaches for solving non-linear equations, but one that provides overall rapid convergence to the solution is the Newton-Raphson method. As a brief overview, the Newton-Raphson method operates by iteratively refining an initial guess for the solution to a system of equations. It utilizes the first-order Taylor series expansion to approximate the root, achieving convergence toward the true solution through successive iterations.

While it is not unequivocally essential that the control algorithm operates rapidly and efficiently for the DC implementation, as it only needs to be executed once per measured variability in the load or source voltages, it is paramount for AC implementations. In the AC case, the goal of the system is to generate a purely sinusoidal voltage and current signal at the output bridge(s). To accomplish this, the phase shift must be dynamically recalculated and modified as often as possible, with higher frequencies producing improved results. For a sinusoidal signal, the maximum rate of voltage change occurs around the zero crossing. This means that by utilizing both the switching frequency, f_s, and the grid frequency, f_g, it is possible to determine the maximum change in input voltage over one switching cycle. This expression is defined as follows:

$$\Delta V_{in,max} = V_{in,max}\left(\sin\left(\frac{2\pi}{\frac{2f_s}{f_g}}\right) - \sin\left(\frac{-2\pi}{\frac{2f_s}{f_g}}\right)\right) \tag{11}$$

Examining (11) presented above reveals that, with fixed values for f_s and f_g, the maximum change per switching cycle exhibits a linear dependence on the maximum input voltage, $V_{in,max}$. With $f_s = 10\,\text{kHz}$, $f_g = 60\,\text{Hz}$, and $V_{in,max} = 20\,\text{V}$, the maximum change in input voltage per switching cycle can be computed to be 0.7539 V. Simply adjusting the computation frequency to occur once every two switching cycles, as opposed to every cycle, results in a doubling of the effective change in input voltage, necessitating a more substantial adjustment in both ϕ_2 and ϕ_3. A higher calculation frequency results in a diminished disparity in input voltage, thereby empowering the converter to generate a more refined and accurate sinusoidal output voltage and current signal. The efficiency of the algorithm becomes pivotal in enabling it to keep pace with the dynamic nature of the system, thereby contributing to the enhancement of the overall converter precision and efficiency.

Considering a high-level overview of the controller, it is a multi-input multi-output system. The two inputs to the algorithm are the desired power magnitudes present at any two of the ports. Concerning only the DC-DC-DC case, it becomes arbitrary which two of the three bridges are specified in terms of desired power. But in the DC-AC-AC case, mentioned in Section 2, it is more sensible to specify the desired power at the DC bridge and one of the AC bridges. As we are generally treating bridge 2 to be an AC input and bridge 3 to be an AC output for our implementation purposes, although the bidirectional nature of the converter allows for these to be either inputs or outputs, the desired power will be specified at ports 1 and 3. At its core, the algorithm is mainly centered around repetitively evaluating the average power flow equations (7), (8), and (9), shifting closer to the desired output result at every iteration. Because of the relationship presented in (10), it is only necessary to apply the Newton-Raphson method to two of the equations instead of all three, specifically (7) and (9) in this case.

Since the power specified at the AC bridges contains average active and reactive power components, it must first be converted into instantaneous total power prior to being utilized within the control algorithm. The translation of desired active ($P_{in,d}$) and reactive ($Q_{in,d}$) power to instantaneous total power at bridge x ($P_{x,desired}$) is illustrated by the following relationships where ω_{f_g} is the grid frequency in $\frac{rad}{s}$ and t_g is the position of the current grid cycle in seconds, ranging from 0 to $\frac{1}{f_g}$:

$$P_{dt} = P_{in,d} - P_{in,d} \cos(2 \cdot \omega_{f_g} \cdot t_g) \tag{12}$$

$$Q_{dt} = Q_{in,d} \sin(2 \cdot \omega_{f_g} \cdot t_g) \tag{13}$$

$$P_{x,desired} = P_{dt} + Q_{dt} \tag{14}$$

The first step of the algorithm is to verify the feasibility of power transfer to individual bridges. In this case, calculation of (7) using parameters of (4) will provide the absolute maximum power transfer to bridge 1 from bridges 2 and 3, and calculation of (9) using parameters of (6) will provide the absolute maximum power transfer to bridge 3 from bridges 1 and 2. If either of these values is smaller than the desired power, the transfer is deemed to be infeasible, and ϕ_2 and ϕ_3 are simply set to zero to prevent any power transfer and maximize safety. This is an initial step used to avoid the microcontroller from having to compute the Newton-Raphson iterative algorithm if the desired power transfer to individual bridges is not possible. It still does not, however, verify that the entered combination of P_1 and P_3 is attainable. This must be done through the successive iterations.

$$R = \begin{bmatrix} P_1 - P_{1,Desired} \\ P_3 - P_{3,Desired} \end{bmatrix} \qquad J = \begin{bmatrix} \frac{\partial P_1}{\partial \phi_2} & \frac{\partial P_1}{\partial \phi_3} \\ \frac{\partial P_3}{\partial \phi_2} & \frac{\partial P_3}{\partial \phi_3} \end{bmatrix} \tag{15}$$

Residuals and Jacobian matrices

$$R_c = \begin{bmatrix} R_{P_1} & R_{P_3} \end{bmatrix} \qquad J_c = \begin{bmatrix} J_{P_1} & J_{P_3} \end{bmatrix} \tag{16}$$

Combined residuals and Jacobian matrices

$$C_m = -J_c^{-1} \cdot R_c \tag{17}$$

$$\begin{aligned} \phi_{2,New} &= \phi_{2,Old} + C_m[1,1] \\ \phi_{3,New} &= \phi_{3,Old} + C_m[2,1] \end{aligned} \tag{18}$$

New ϕ_2 and ϕ_3 values

Next, the controller performs the iterative Newton-Raphson approach repeating the following steps for a maximum of ten iterations. The residuals and Jacobian matrices are first calculated for ports 1 and 2 through (15). Then, the old values of ϕ_2 and ϕ_3 from the previous iteration are compared against each other to ensure their values are non-equal. Substituting equivalent values of ϕ_2 and ϕ_3 into the power flow equations will result in computational errors, and thus 0.05 is either added or subtracted to ϕ_2 depending on whether it is negative or positive, respectively. The old phase shift values, or the ones calculated in the previous iteration, along with the other parameters specified in Table 2 and either Table 3 or Table 4 depending on the transformer configuration, are then substituted into the residual and Jacobian matrices and then combined to form a single system as in (16). The corrections matrix is then generated using the inverse matrix function as in (17). Next, the updated values of ϕ_2 and ϕ_3 can be calculated using the newly generated corrections matrix by evaluating the relationships in (18). Ensuring proper operation of the converter, the updated phase shift values must then be saturated to the bounds illustrated in (1) and (2).

$$\text{norm}([\phi_{2,New} - \phi_{2,Old} \quad \phi_{3,New} - \phi_{3,Old}]) \tag{19}$$

At this point, the newly generated phase shift values can be checked for convergence. Once the Euclidean norm, calculated as in (19), is lower than a specified threshold of 10^{-6}, the power sharing solution has been achieved and the system can break out of the iterative loop. If convergence has not yet been achieved, the values of $\phi_{2,Old}$ and $\phi_{3,Old}$ must be set equal to $\phi_{2,New}$ and $\phi_{3,New}$, respectively, and the loop should repeat. If the maximum number of iterations has been reached without the controller breaking out of the loop, this is indicative of the controller not being able to find a solution to the requested configuration of power flow. In this case, the transfer is unattainable given the hardware components, and the values of ϕ_2 and ϕ_3 are both set to zero for safety. Lastly, the newly calculated values of ϕ_2 and ϕ_3 can then be applied to a phase shift controller to generate the appropriate MOSFET switching control signals.

While not recommended for physical hardware implementation due to the extra microcontroller computational overhead, for control algorithm verification purposes, the generated phase shift values can be substituted back into (7), (8), and (9) to obtain the calculated output power. This can then be compared against the desired output power to ensure algorithmic efficacy. This serves as the baseline for the analysis presented in Section 5 and Section 6.

4. CONTROL ITERATION EFFICIENCY

In most instances, the computation of the Newton-Raphson iterative approach can be completed within only a couple of iterations. By implementing the algorithm within MATLAB, Table 1 outlines the number of iterations required to reach convergence of the solution. This table follows the same power step changes as presented in Figure 3, Figure 4, and Figure 6. The first step is indicative of the initial algorithmic computation when the converter is first turned on and thus no previous values exist. In this case, ϕ_2 and ϕ_3 are set to arbitrarily chosen values, $\phi_2 = 0.1$ and $\phi_3 = 0.2$. All future step changes use starting values of ϕ_2 and ϕ_3 that were calculated in the previous step change as an initial starting point. As expected, Table 1 illustrates algorithmic efficiency, allowing for rapid convergence to the desired power-sharing solution, even under extreme cases with large changes in both the sign and magnitude of the desired power at each port. With a maximum iteration count of 5 and an average of 4.625, the controller will spend little time deriving the new phase shift values at each step change. Reducing the magnitude difference of power demanded between step changes will further decrease the number of required iterations, illustrating promising results for implementation in the AC case.

Step	1	2	3	4	5	6	7	8
$P_{1,Desired}$ (W)	45	-15	-30	-30	10	50	0	35
$P_{3,Desired}$ (W)	-10	50	40	-15	40	-10	-30	-40
Iteration Count	4	5	4	5	5	5	5	4

Table 1. Newton-Raphson iteration measurement.

Identifying the power equations presented in (7), (8), and (9), there are several simplifications that can be made to improve the computational efficiency at runtime. First, the denominator is made up of terms determined by the converter architecture, and can therefore be calculated at compile time rather than at runtime. Additionally, by utilizing the relationship in (10), it can be seen that specifying power at only two bridges suffices. This allows the application of the Newton-Raphson method to reap enhanced calculation efficiency and simplicity. Lastly, executing each step of the proposed method on the microcontroller one by one takes additional overhead and is not necessary. Symbolically working through the method provides two resulting equations for $\phi_{2,New}$ and $\phi_{3,New}$ that, while visually complex, can be directly solved for, substantially reducing the algorithmic computation time.

Because MATLAB is not implemented on a real-time system, it is not possible to accurately obtain iteration execution time. Instead, the code must be translated to a real-time system, such as the F28377S C2000 Launchpad used as the main TAB control board. Based on this, the average execution time for a single iteration of the proposed algorithm was determined to be $2.76\,\mu$s. Utilizing the switching frequency identified in Table 2, the algorithm can be executed 36.23 times per switching cycle. This is significantly more than the absolute worst-case calculation length of 20 iterations.

In the DC-AC-AC case, the computation of phase shift values through the newly proposed control algorithm occurs once per switching cycle. In this case, the system parameters from one cycle to the next incur very small changes. Performing a simulation of the DC-AC-AC TAB control algorithm within MATLAB, it can be observed that for the system parameters specified in Table 2 and Table 5, the average number of iterations per switching cycle is calculated to be 1.9965. Applying the hardware-determined execution time of $2.76\,\mu$s, the average execution time per switching cycle is $5.5103\,\mu$s. This deems the algorithm appropriate for implementation on the DC-AC-AC TAB converter.

5. DC-DC-DC TAB RESULTS

To successfully validate the control algorithm for the triple active bridge, the accuracy must be verified for each of the scenarios presented in Figure 2 due to the converter's bidirectional nature. Additionally, validation of the controller under both unity, or 1:1:1 turns ratio, and non-unity transformer cases can ensure appropriate implementation in a wide array of applications. As the DC-DC-DC case is a simpler topology than the DC-AC-AC configuration, this section will contain both simulation and hardware analysis, facilitating

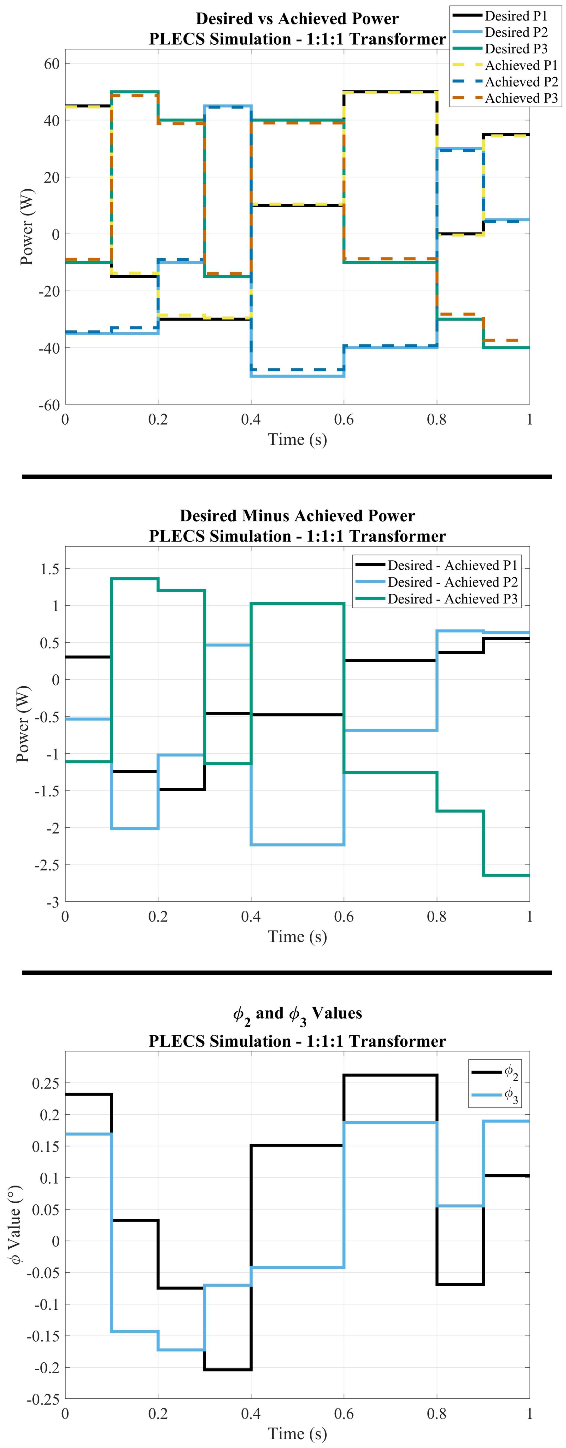

Figure 3. PLECS derived graphs of the proposed Newton-Raphson control algorithm implementation with a 1:1:1 transformer turns ratio.

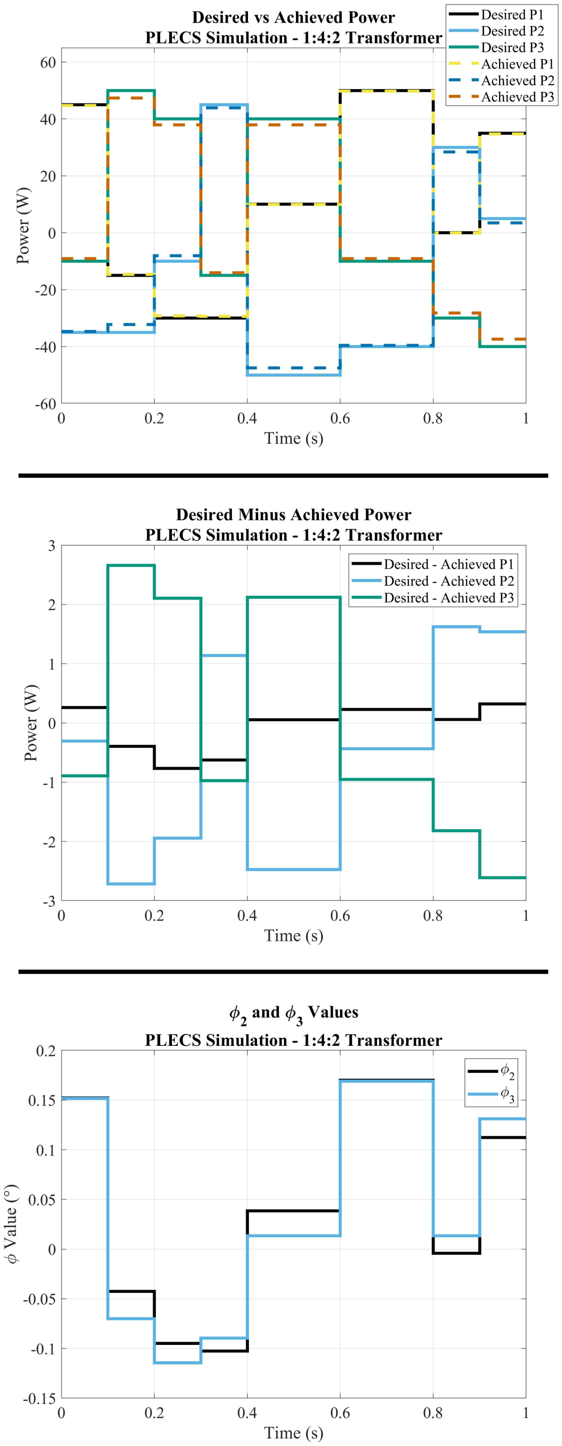

Figure 4. PLECS derived graphs of the proposed Newton-Raphson control algorithm implementation with a 1:4:2 transformer turns ratio.

the understanding of the proposed control algorithm in a simpler context. This approach more easily illustrates the effectiveness of the algorithm's functionality. To complete this testing, a sequence of step changes will be used in terms of the input or output power specified at bridges 1 and 3. The desired power at bridge 2 can be simply calculated using (10). This will allow the converter to be placed in a variety of power flow configurations, as illustrated in the proceeding unity and non-unity transformer analysis sections. For this analysis, positive values of P_1, P_2, or P_3 denote power sources, and negative values indicate power sinks. General TAB system parameters for both simulation and hardware verification are presented in Table 2. Simulation is completed using PLECS and will cover the unity transformer parameters in Table 3 and the non-unity transformer parameters outlined in Table 4. Hardware will follow the circuit configuration as pictured in Figure 5 and will cover the unity transformer parameters in Table 3.

Switching Frequency	10 kHz
Duty Cycle	50%
Magnetizing Inductance L_m	5.107mH
Leakage Inductance L_1	19.78μH
Leakage Inductance L_2	14.14μH
Leakage Inductance L_3	11.36μH

Table 2. Default TAB system parameters.

Turns Ratio (N_1:N_2:N_3)	1:1:1
Primary Voltage (V_1)	20V
Secondary Voltage (V_2)	20V
Tertiary Voltage (V_3)	20V

Table 3. Unity transformer DC-DC-DC TAB system parameters.

Turns Ratio (N_1:N_2:N_3)	1:4:2
Primary Voltage (V_1)	20V
Secondary Voltage (V_2)	80V
Tertiary Voltage (V_3)	40V

Table 4. Non-unity transformer DC-DC-DC TAB system parameters.

5.1. UNITY TRANSFORMER SIMULATION RESULTS

By integrating the newly proposed control algorithm within PLECS, implementation efficacy and output deviation of the strategy can be identified. Using the TAB system parameters identified in Table 2 and Table 3, the algorithm can be validated for instances where the voltage on each of the three bridges is equal and time-invariant. Having the same voltage across each transformer winding is desired in applications where safety and noise mitigation are the main concerns for converter implementation.

Placing the converter in a variety of phase configurations as presented in Figure 2, the graphs obtained through PLECS simulation are presented in Figure 3. The top graph illustrates the desired vs achieved power, constituting seven load changes throughout. The desired power is the value input by the user and the achieved power is calculated through the measurement of source voltage and current. Both the desired and achieved waveforms closely overlap, barring a small deviation due to modeled parasitic circuit elements, namely the transformer resistance. The graph in the middle shows the deviation between the user input desired power versus the achieved power. With a maximum absolute deviation of just under 3W, the effectiveness of this algorithm is underscored, emphasizing its importance in practical applications. The bottom graph illustrates the phase shift values, ϕ_2 and ϕ_3, that have been calculated through the employment of the control algorithm.

5.2. NON-UNITY TRANSFORMER SIMULATION RESULTS

In many realistic cases of TAB implementation, it is not desirable that the voltage on each of the three bridges is equal. Because of this, the control algorithm must continue to hold even in the non-unity case. For the following analysis, the TAB system parameters are defined in Table 2 and Table 4.

Similar to the unity transformer case, the TAB has been examined in PLECS with the same desired power curve, allowing the algorithm to be tested in each of the six possible phase configurations. The graphs obtained through this testing are available in Figure 4. When comparing these waveforms to those presented in the unity transformer case, the top graph is almost identical, containing slightly different power transfer error while still maintaining less than 3W of absolute maximum deviation, as can be seen in the middle graph. Expectantly, the calculated phase shift values, shown in the bottom graph, illustrate a decrease in magnitude. This is due to bridges 2 and 3 containing a higher voltage, thus requiring less current to be transferred between bridges. In this case, it is also apparent that the control algorithm is effective for varying combinations of transformer turn ratios.

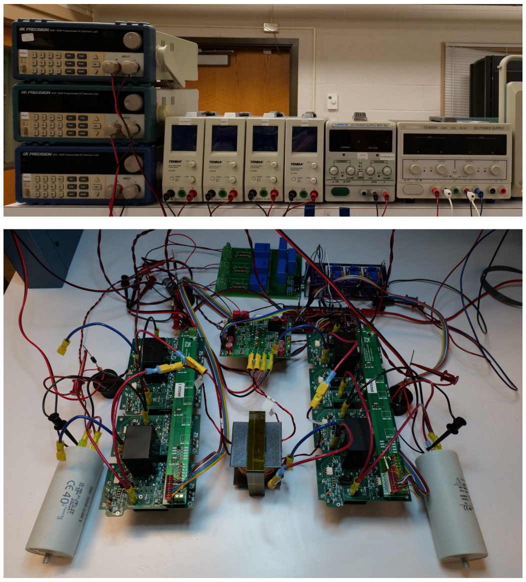

Figure 5. DC-DC-DC TAB hardware test setup.

5.3. HARDWARE RESULTS

The newly proposed control algorithm, for the unity transformer case with system parameters specified in Table 2 and Table 3, has also been validated through hardware implementation. A photo of the hardware setup used for testing is available in Figure 5.

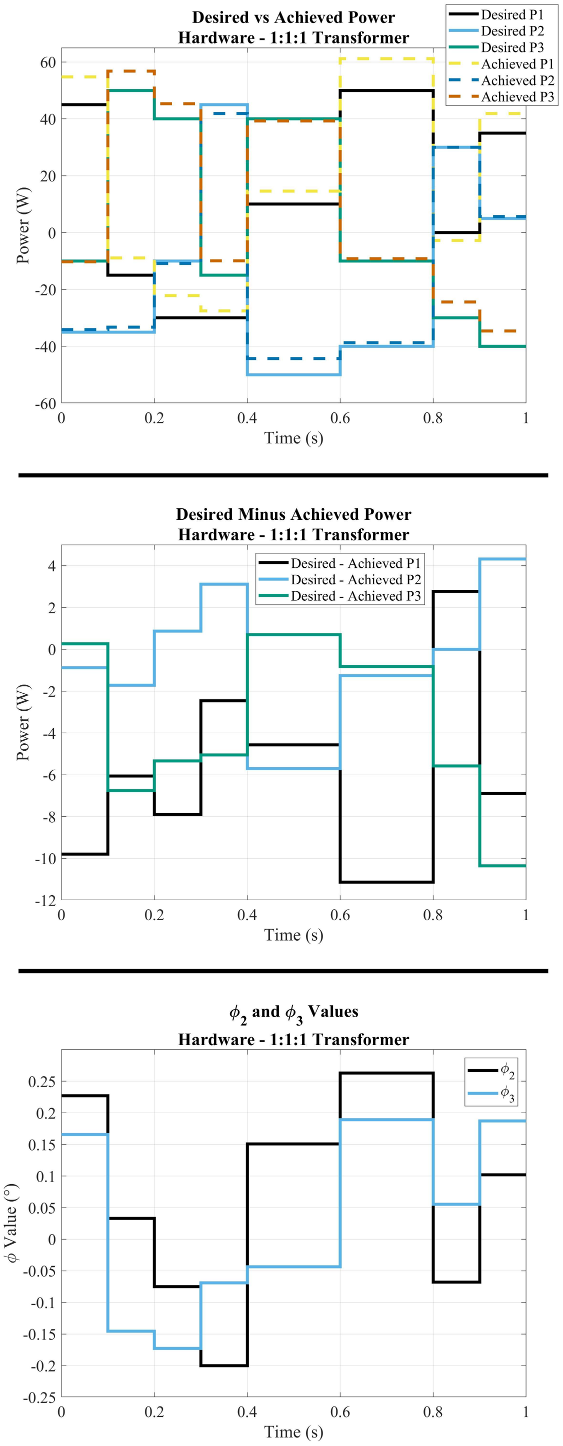

Figure 6. Hardware derived graphs of the proposed Newton-Raphson control algorithm implementation with a 1:1:1 transformer turns ratio.

Analyzing the waveforms presented in Figure 6, the top graph illustrates the difference in power desired vs the power achieved by the converter. This difference is shown in the middle graph, indicating a maximum absolute power sharing error of 12W, with the typical error being much lower. At lower power levels, such as the ones used for testing in this case, some of the undesirable converter elements become more significant in relation to total power transfer, specifically the snubber RC circuit across the MOSFETs. At higher levels of power transfer, the power consumed by this snubber circuitry remains relatively constant, therefore constituting a lower overall power percentage. Additionally, the physical hardware prototype has significantly more parasitic inductance, capacitance, and resistance than the modeled PLECS circuit. Although this is the case, the overall power transfer error is still quite minimal, indicating the effectivity of the newly proposed control algorithm. Lastly, the lower graph illustrates the values of ϕ_2 and ϕ_3 calculated by the F28377S C2000 Launchpad microcontroller. As expected, these values are identical to those generated in the unity transformer PLECS simulation case.

6. DC-AC-AC TAB HARDWARE RESULTS

The final configuration of the triple active bridge featured in this research contains one DC port, allowing for the integration of energy storage, and two AC ports, enabling the seamless connection of two AC electrical grids. By applying the previously introduced control algorithm to this new TAB configuration, its functionality can once again be illustrated and validated. A depiction of the hardware setup for this case can be seen in Figure 12. This section will concentrate exclusively on the practical implementation of the controller in hardware, demonstrating the applicability and robustness of the algorithm in a more complex system configuration.

In a PLECS representation of the triple active bridge converter, the idealistic nature of the circuit elements presents zero power transfer at zero phase shift regardless of the voltages present at the bridges. However, in a realistic hardware configuration, this is not the

Turns Ratio (N_1:N_2:N_3)	1:1:1
Primary Voltage (V_1)	20V
Secondary Voltage (V_2)	$20V_{peak}$
Tertiary Voltage (V_3)	$20V_{peak}$

Table 5. Unity transformer DC-AC-AC TAB system parameters.

case. Due to variability in parasitic elements, individual transformer winding construction, and individual MOSFET propagation and switching times, there is significant power transfer that occurs when bridge voltage magnitude is unequal. Regardless of these implementation inefficiencies that prevent direct controller analysis through hardware power transfer, the algorithm can still be validated through analysis of the generated phase shift values.

Presented in Figure 7 are the expected values of ϕ_2 and ϕ_3, as generated in MATLAB for the case of $P_{1,des} = 0W$, $P_{3,des} = 60W$, $Q_{3,des} = 10VAR$. For the same scenario, the values calculated on hardware using real-time feedback of source voltages and phase detection utilizing a second-order generalized integrator (SOGI) phase-locked loop (PLL) controller can be seen in Figure 8. Overall, the shape of ϕ_2 and ϕ_3 calculated in both implementations are very similar, validating the employment of the SOGI PLL, the voltage sensing elements as described in the appendix in Section 8.3, and the controller application.

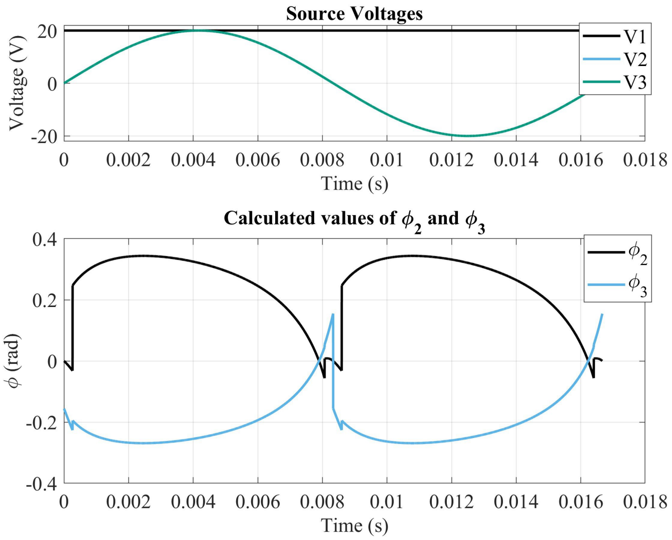

Figure 7. MATLAB generated ϕ values. $P_{1,d} = 0W$, $P_{3,d} = 60W$, $Q_{3,d} = 10VAR$.

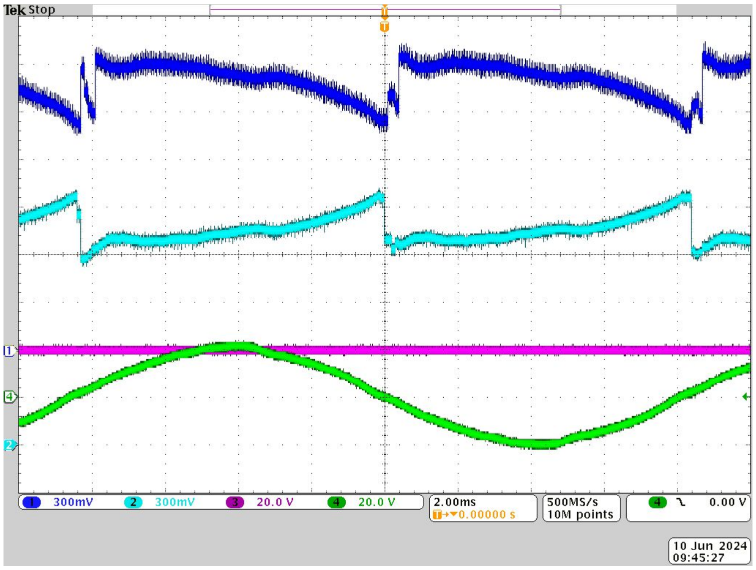

Figure 8. Hardware generated ϕ values. Top to bottom: dark blue = ϕ_2, light blue = ϕ_3, pink = DC bridge voltage, green = AC bridge 2 voltage. $P_{1,d} = 0W$, $P_{3,d} = 60W$, $Q_{3,d} = 10VAR$.

Similarly, the same analysis has taken place for an alternate scenario of $P_{1,des} = 0W$, $P_{3,des} = 60W$, $Q_{3,des} = 10VAR$ to illustrate system bidirectionality. The MATLAB-generated values are available in Figure 9 and the hardware-generated values are shown in Figure 10. Analogous to the previous case, the two graphs possess a very similar waveform shape.

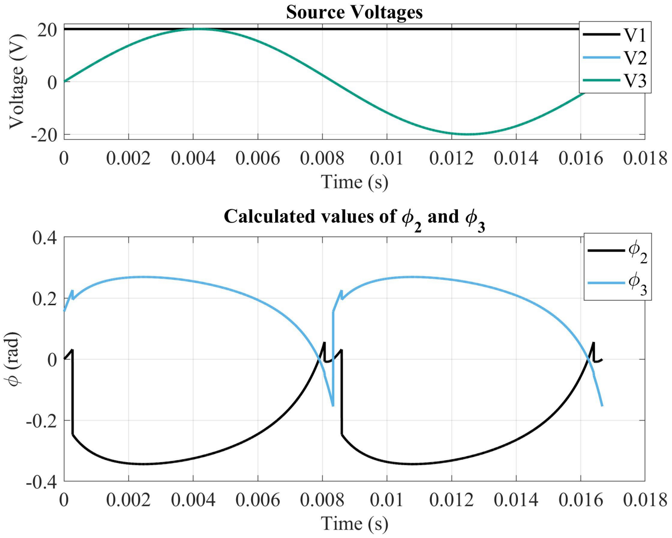

Figure 9. MATLAB generated ϕ values. $P_{1,d} = 0W$, $P_{3,d} = -60W$, $Q_{3,d} = -10VAR$.

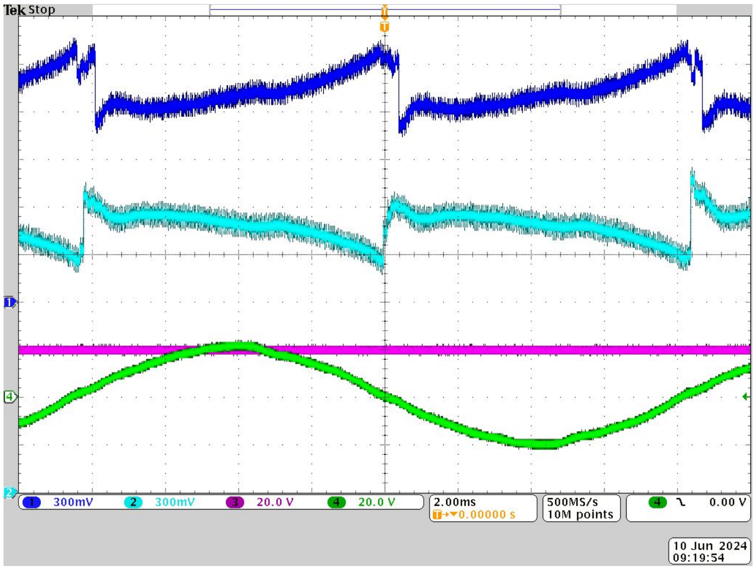

Figure 10. Hardware generated ϕ values. Dark blue = ϕ_2, light blue = ϕ_3, pink = DC bridge voltage, green = AC bridge 2 voltage. $P_{1,d} = 0W$, $P_{3,d} = -60W$, $Q_{3,d} = -10VAR$.

Since the TAB consists of a collection of DC and AC sources, the switching polarity must be inverted for the AC bridges during the negative half cycle of the input waveform. To accomplish this, all switches must be turned off for one switching cycle and then restarted with the correct polarities applied in the next cycle. This creates a small period of zero transformer voltage and current as can be seen in Figure 11. Due to the two-switch board hardware configuration as described in the appendix in Section 8.2, extra care must be taken during switching events to ensure continuous transformer current. A single leg of the converter must be switched in a specific order, allowing current to flow through the snubber circuitry or MOSFET body diodes. Improper switching of the MOSFETs can lead to significant transformer voltage spikes occurring at switching events. Additionally, the illustration of voltage-dependent power transfer at a phase shift of zero can also be seen in this figure, exemplified by the magnitude increase in transformer current surrounding the zero crossing.

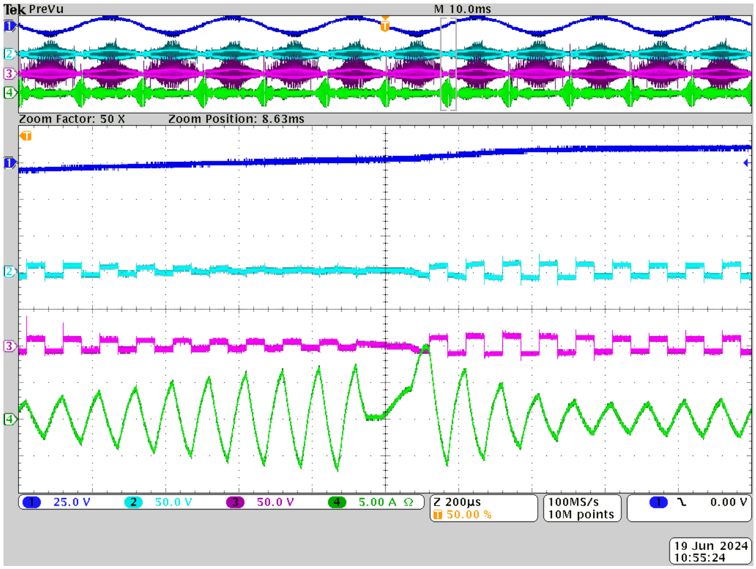

Figure 11. AC zero crossing transformer voltage and current waveforms. Dark blue = AC bridge 2 voltage, light blue = bridge 2 transformer voltage, pink = bridge 3 transformer voltage, green = bridge 2 transformer current. $\phi_2 = 0$, $\phi_3 = 0$.

7. CONCLUSION

The research encompassed within this paper presents an in-depth analysis of the triple active bridge (TAB) converter topology, followed by a detailed description of the newly proposed control algorithm. Validated initially through simulation and hardware in the DC-DC-DC TAB and then in hardware on the DC-AC-AC TAB, the efficacy of the presented feed-forward control architecture has been underscored through a low achieved power sharing error. The rigorous evaluation of results from these simulated and physical tests deem the adapted Newton-Raphson control architecture an appropriate method for determining the phase shift parameters, ϕ_2 and ϕ_3, from the set of non-linear power flow equations. Characterized by a minimal number of iterations required to achieve convergence, the algorithm proves implementable on typical microcontroller-based processors. In addition, aside from the algorithm being merely effective, it has also shown to be highly adaptable and can therefore be easily modified to fit any configuration of DC or AC sources or loads at

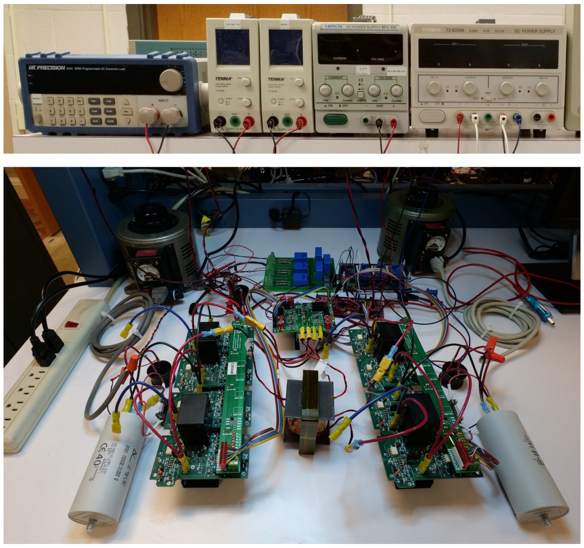

Figure 12. DC-AC-AC TAB hardware test setup.

each port. In the future, additional work may include further enhancement of the control architecture through the implementation of a feedback controller. This closed-loop control will enable further mitigation of the power transfer sharing error.

8. APPENDIX - TAB SYSTEM DESIGN

The TAB incorporates a plethora of hardware components, all of which construct the converter topology. The following section provides a highly concise description of various design choices concerning the high-frequency transformer, the two-switch boards used on the AC bridges, the measurement of system variables, and the overall construction of the bridge and port combinations.

8.1. TRANSFORMER CONSTRUCTION

The transformer constructed for the TAB is a three-winding high-frequency transformer. The core material selected is an N87 ferrite core, known for its excellent magnetic properties such as lower core losses at high frequencies and high saturation magnetization. The core is configured in an E shape, which facilitates efficient magnetic flux distribution and minimizes loses [24].

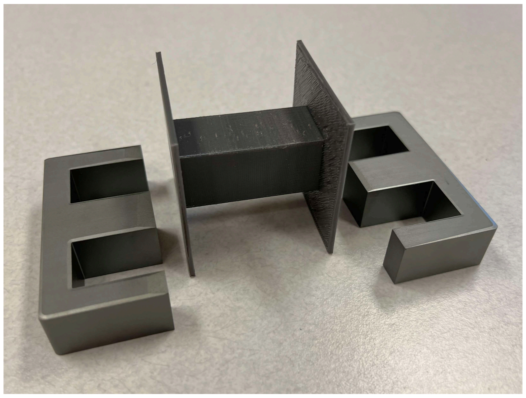

Figure 13. N87 transformer core material and 3D printed bobbin.

To accommodate the windings, a custom 3D-printed bobbin was designed and sized to fit tightly between the two core elements, providing structural integrity and simplifying construction. A photo of the ferrite core and custom 3D printed bobbin can be seen in Figure 13. Each of the three independent windings was fabricated using Litz wire, chosen specifically for its ability to reduce skin effect and proximity effect at higher frequencies [24]. The Litz wire consists of eleven smaller strands, twisted to form a composite strand, with each winding consisting of 32 turns around the bobbin. This configuration improves the current distribution across the conductor, thereby improving the overall transformer efficiency.

8.2. TAB TWO-SWITCH BOARD

The two-switch boards designed for the AC bridges incorporate electrical isolation between power and signal traces. This isolation is achieved through an isolated DC-DC power supply and optocoupler-based gate drivers. Physical isolation is also present between the high voltage power traces and low voltage signal traces. Each individual board features two silicon n-channel MOSFETs, configured with their sources connected to enable the bidirectional blocking of AC current.

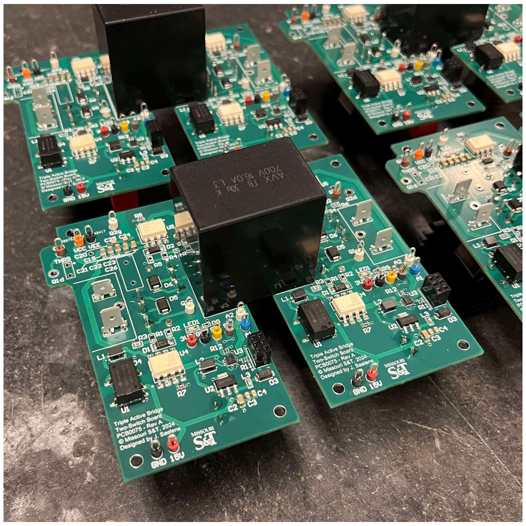

Figure 14. TAB two-switch board.

Physically, two of these green boards are connected through a large buffer capacitor and a power jumper, forming a single leg of an H-bridge. Joining two of these board pairs, constituting a total of eight MOSFETs, implements a full H-bridge. The PCB is a four-layer design, composed of two power layers, one ground layer, and one signal layer. This design ensures low noise injection on the signal planes, enhancing the converter safety and performance. The hardware design in shown in Figure 14.

8.3. SYSTEM VARIABLE MEASUREMENT

Accurately computing the values of ϕ_2 and ϕ_3 based on the relationships provided in (7), (8), and (9) requires the voltage at each of the three bridges to be known at all times. To accurately measure these voltages, a set of LV-25P voltage transducers are used, as shown in Figure 15. As the output of this transducer is centered around zero, it must be appropriately applied a gain and bias to match the microcontroller's analog input range of 0-3.3V. To achieve this, an op-amp based analog circuit board is used to scale and shift the waveform, also providing noise rejection. Additionally, this sensor board includes three LM 55-P hall effect current sensor modules. This allows provisions for future control strategies that may require the measurement of one or more system currents.

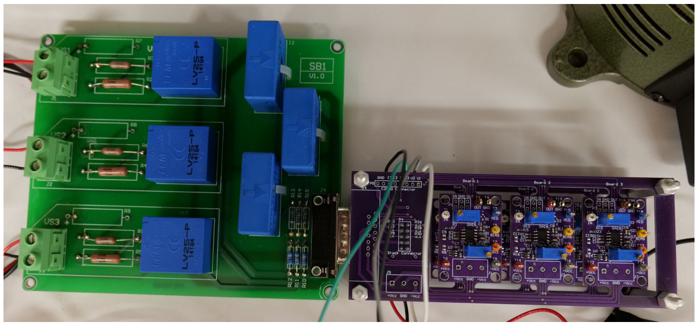

Figure 15. Voltage and current measurement board.

8.4. GENERAL BRIDGE AND PORT CONSTRUCTION

Given the complexity of the TAB topology, which interfaces both AC and DC sources, construction of the each bridge varies accordingly. As mentioned in Section 2, the AC bridges require back-to-back switches to block current flow during the negative half-cycle of the voltage waveform. Additionally, the input LC low-pass filter for AC bridges must be designed to handle negative voltages. These nuances are further described in the following sections, categorized by source type.

8.4.1. DC Bridge and Port Construction. Unlike the AC bridges, the DC bridge does not require back-to-back MOSFETs because the voltage across the supply rail is always positive. Consequently, a standard H-bridge configuration can be used, featuring electrically isolated signal and power domains to mitigate noise and enhance safety.

Given that a DC power supply can only source current, a Schottky diode is placed in series with the source to prevent it from attempting to sink current. Additionally, an electronic load is connected in parallel with the series source and diode to consume any power transmitted to the DC bridge.

To prevent the load from drawing current at twice the switching frequency, a low-pass filter must be implemented between the load and the bridge. The components selected for this LC low-pass filter include an aluminum electrolytic capacitor of 47 μF, and a 270 μH drum core wire-wound inductor with an equivalent series resistance (ESR) of 56 mΩ. The cutoff frequency of this LC low-pass filter was calculated to be approximately 1.413 kHz using the following relationship:

$$f_c = \frac{1}{2\pi\sqrt{LC}} \tag{20}$$

8.4.2. AC Bridge and Port Construction. The AC bridge design includes multiple key components to improve the overall performance and ensure safety. To mitigate voltage spikes and oscillations caused by the switching of MOSFETs, an RC snubber was implemented across each pair of MOSFETs. Due to the complexity of mathematically designing the snubber, the values were determined experimentally. The optimal values were found to be a capacitance of 1500 pF and a resistance of 6.2 Ω. To improve the safety of the converter, an inline fuse is included in series with the AC source to prevent damage in the event of a failure.

To prevent high-frequency switching harmonics from being injected into the grid frequency waveform, an LC low-pass filter must also be employed on the AC bridges. Unlike the DC bridge, however, this filter must handle negative voltages, which the electrolytic capacitor used in the DC bridge cannot support. Therefore, a $40\,\mu$F polypropylene film capacitor with an ESR of $2\,\mathrm{m}\Omega$ was selected. The inductor, similar to the one used on the DC bridge, was a $270\,\mu$H drum core wire-wound inductor with an ESR of $56\,\mathrm{m}\Omega$. Using the relationship provided in (20), the cutoff frequency for this configuration was calculated to be approximately 1.531 kHz.

ACKNOWLEDGMENT

The authors would like to thank Sandia National Laboratories for providing the funding for this project.

REFERENCES

[1] Xu She, Alex Q. Huang, and Rolando Burgos. Review of solid-state transformer technologies and their application in power distribution systems. *IEEE Journal of Emerging and Selected Topics in Power Electronics*, 1(3):186–198, 2013. doi: 10.1109/JESTPE.2013.2277917.

[2] Zheqing Li, Feng Jin, Xin Lou, Yi-Hsun Hsieh, Qiang Li, and Fred C. Lee. A transformer design with pcb litz wire concept for solid state transformer. In *2023 IEEE Energy Conversion Congress and Exposition (ECCE)*, pages 848–854, 2023. doi: 10.1109/ECCE53617.2023.10362376.

[3] Akrem Mohamed Elrajoubi and Simon S. Ang. High-frequency transformer review and design for low-power solid-state transformer topology. In *2019 IEEE Texas Power and Energy Conference (TPEC)*, pages 1–6, 2019. doi: 10.1109/TPEC.2019.8662131.

[4] Hengsi Qin and Jonathan W. Kimball. Solid-state transformer architecture using ac–ac dual-active-bridge converter. *IEEE Transactions on Industrial Electronics*, 60(9): 3720–3730, 2013. doi: 10.1109/TIE.2012.2204710.

[5] Kartikeya Jp Veeramraju, Angshuman Sharma, and Jonathan W. Kimball. A comprehensive analysis on complex power flow mechanism in an ac-ac dual active bridge. In *2022 IEEE Power and Energy Conference at Illinois (PECI)*, pages 1–6, 2022. doi: 10.1109/PECI54197.2022.9744009.

[6] Angshuman Sharma, Kartikeya Jp Veeramraju, and Jonathan W. Kimball. Power flow control of a single-stage ac-ac solid-state transformer for ac distribution system. In *2022 IEEE Power and Energy Conference at Illinois (PECI)*, pages 1–6, 2022. doi: 10.1109/PECI54197.2022.9744006.

[7] Subhradip Mukherjee and Indrajit Sarkar. A brief review on triple active bridge dc-dc converter. In *2023 IEEE International Students' Conference on Electrical, Electronics and Computer Science (SCEECS)*, pages 1–6, 2023. doi: 10.1109/SCEECS57921.2023.10063031.

[8] Shenli Zou, Jiangheng Lu, Ayan Mallik, and Alireza Khaligh. Modeling and optimization of an integrated transformer for electric vehicle on-board charger applications. *IEEE Transactions on Transportation Electrification*, 4(2):355–363, 2018. doi: 10.1109/TTE.2018.2804328.

[9] Viju Nair R., Srinivas Gulur, Ritwik Chattopadhyay, and Subhashish Bhattacharya. Integrating photovoltaics and battery energy storage to grid using triple active bridge and voltage source converters. In *IECON 2020 The 46th Annual Conference of the IEEE Industrial Electronics Society*, pages 3691–3696, 2020. doi: 10.1109/IECON43393.2020.9255053.

[10] Van-Long Pham and Keiji Wada. Applications of triple active bridge converter for future grid and integrated energy systems. *Energies*, 13(7), 2020. ISSN 1996-1073. doi: 10.3390/en13071577. URL https://www.mdpi.com/1996-1073/13/7/1577.

[11] Gouri Deshmukh, Pradyumn Chaturvedi, and Vedashree Rajderkar. Single phase cascaded h-bridge multilevel inverter topology. In *2022 International Conference on Futuristic Technologies (INCOFT)*, pages 1–6, 2022. doi: 10.1109/INCOFT55651.2022.10094514.

[12] N Sujitha. and K Ramani. A new hybrid cascaded h-bridge multilevel inverter - performance analysis. In *IEEE-International Conference On Advances In Engineering, Science And Management (ICAESM -2012)*, pages 46–50, 2012.

[13] Mohsen Feizi and Reza Beiranvand. An improved phase-shifted full-bridge converter with extended zvs operation range for ev battery charger applications. In *2020 11th Power Electronics, Drive Systems, and Technologies Conference (PEDSTC)*, pages 1–6, 2020. doi: 10.1109/PEDSTC49159.2020.9088444.

[14] Nezihe Yildiran. Design methodology and implementation of half-bridge llc resonant converter. In *2020 International Conference on Electrical, Communication, and Computer Engineering (ICECCE)*, pages 1–6, 2020. doi: 10.1109/ICECCE49384.2020.9179322.

[15] Hai-Nam Vu, Dai-Duong Tran, and Woojin Choi. A novel hybrid soft switching full-bridge pwm and full-bridge llc converter for on-board battery charger applications. In *2016 IEEE 8th International Power Electronics and Motion Control Conference (IPEMC-ECCE Asia)*, pages 2470–2473, 2016. doi: 10.1109/IPEMC.2016.7512686.

[16] Xiaoqiang Li, Jinwei Huang, Yongchao Ma, Xintan Wang, Jiafeng Yang, and Xiaojie Wu. Unified modeling, analysis, and design of isolated bidirectional cllc resonant dc–dc converters. *IEEE Journal of Emerging and Selected Topics in Power Electronics*, 10(2):2305–2318, 2022. doi: 10.1109/JESTPE.2022.3145817.

[17] Angshuman Sharma, Alvaro Cardoza, Kartikeya J. P. Veeramraju, Oroghene Oboreh-Snapps, and Jonathan W. Kimball. Bidirectional asymmetric clllc resonant dc-dc converter for onboard electric vehicle chargers. In *2023 IEEE Energy Conversion Congress and Exposition (ECCE)*, pages 2109–2116, 2023. doi: 10.1109/ECCE53617.2023.10362332.

[18] Ritwik Chattopadhyay, Sayan Acharya, Ghanshyamsinh Gohil, and Subhashish Bhattacharya. One switching cycle current control strategy for triple active bridge phase-shifted dc-dc converter. In *2017 IEEE Industry Applications Society Annual Meeting*, pages 1–8, 2017. doi: 10.1109/IAS.2017.8101785.

[19] Kazuki Minami, Shota Okutani, Masaya Ohura, Pin-Yu Huang, and Yuichi Kado. Machine learning aided optimized modulation in triple active bridge converter. In *IECON 2022 – 48th Annual Conference of the IEEE Industrial Electronics Society*, pages 1–6, 2022. doi: 10.1109/IECON49645.2022.9968640.

[20] Yue Yu, Keiji Wada, and Yuichi Kado. Power flow control of dc power distribution systems using triple active bridge converter in a data center. In *2018 9th IEEE International Symposium on Power Electronics for Distributed Generation Systems (PEDG)*, pages 1–6, 2018. doi: 10.1109/PEDG.2018.8447655.

[21] Babak Rahrovi, Ramin Tafazzoli Mehrjardi, and Mehrdad Ehsani. On the analysis and design of high-frequency transformers for dual and triple active bridge converters in more electric aircraft. In *2021 IEEE Texas Power and Energy Conference (TPEC)*, pages 1–6, 2021. doi: 10.1109/TPEC51183.2021.9384990.

[22] Venkateswara Rao Kudaravalli, Vishwabandhu Uttam, and Vishnu Mahadeva Iyer. A design methodology for triple active bridge dc- dc converter. In *2022 IEEE International Conference on Power Electronics, Drives and Energy Systems (PEDES)*, pages 1–7, 2022. doi: 10.1109/PEDES56012.2022.10080029.

[23] Jonathan Saelens, Lauryn Morris, Oroghene Oboreh-Snapps, Arnold Fernandes, Praneeth Uddarraju, Sophia A. Strathman, and Jonathan W. Kimball. Instantaneous current and average power flow characterization of a dc-dc-dc triple active bridge converter. In *2024 IEEE Power and Energy Conference at Illinois (PECI)*, pages 1–6, 2024.

[24] Deepak S and S. R. Mohanrajan. High-frequency transformer design for a bi-directional isolated dc-dc converter for electric vehicles. In *2022 IEEE 7th International Conference on Recent Advances and Innovations in Engineering (ICRAIE)*, volume 7, pages 428–432, 2022. doi: 10.1109/ICRAIE56454.2022.10054344.

SECTION

3. CONCLUSIONS AND FUTURE WORK

3.1. SUMMARY

Presented within this thesis, the design and development of the triple active bridge power converter has been investigated. The defining equations for average power and instantaneous current have been identified and verified using a MATLAB script to calculate the resulting equation output, providing a comparative graph between the calculated and PLECS simulated values. Subsequently, the hardware design for the DC-DC-DC TAB was proposed and validated using PLECS simulations. Following this, a hardware prototype of TAB architecture was constructed to substantiate the aforementioned defining equations. Once the basic functionality of the DC-DC-DC TAB was established, a feed-forward extended Newton-Raphson control methodology was proposed to dynamically calculate the phase shift parameters ϕ_2 and ϕ_3. The validation of this newly proposed control architecture on the TAB hardware prototype concluded the DC implementation of the TAB.

Transitioning to the ultimate TAB configuration, in which one port contains a DC source and two ports accommodate AC sources, the DC-AC-AC TAB was presented. This updated topological design was then implemented in PLECS to validate its efficacy. After adapting the previously introduced Newton-Raphson control methodology to comply with the DC-AC-AC implementation, incorporation within PLECS provided validation through simulation. Finally, the hardware prototype setup was modified to include the two AC bridges and validate the system's performance, allowing for comparative analysis between simulated and real-world results.

The primary challenges encountered throughout this research relate to the non-linear configuration of the TAB converter. Through analysis of the presented average power flow equations, it becomes evident that a simplistic and straightforward control algorithm can not be obtained. Because of this, a linearization technique must be applied to the mathematical model to more easily and efficiently derive the desired output. An associated challenge is that of the microcontroller's maximum operational frequency. Since the DC-AC-AC TAB contains time-varying components, the phase shift values, ϕ_2 and ϕ_3, must be dynamically updated each switching cycle to ensure seamless and efficient converter operation. Consequently, the control algorithm must be optimized to ensure computations are completed within a single switching cycle.

The research provided within this thesis illustrates the contributions to the field of power electronics, particularly in the realm of the triple active bridge (TAB) converter. The design and control methods presented expand the applicability of the converter, facilitating its more widespread adoption in applications ranging from renewable energy integration to electric vehicle charging infrastructure. The TAB holds significant promise for the transition towards an ever-evolving sustainable and electrified future, highlighting its transformative potential in shaping the evolving energy landscape.

3.2. FUTURE WORK

While this thesis has presented a comprehensive overview of the design, development, and validation of the DC-AC-AC triple active bridge converter, further improvements can be made to increase the conversion efficiency and performance. As research in the field continues to advance, exploring additional application scenarios will further improve the utility and versatility of the TAB. Through continual refinement of the converter topology and control strategies, the potential applications of the TAB are virtually endless.

The enhanced Newton-Raphson method presented within this thesis operates in feed-forward mode, directly calculating the values of ϕ_2 and ϕ_3 without employing feedback. This method inherently introduces output error due to realistic circuit elements not being incorporated within the mathematical equations and algorithm design. Implementing a closed-loop feedback controller would aid in reducing this output error by measuring and compensating for these non-modeled, realistic circuit elements. A closed-loop architecture can also aid converter efficiency, response, and robustness during transients or load changes.

Another direction for future work includes investigating the potential for higher frequency operation, further contributing to the physical minimization of the TAB converter. Exploring additional semiconductor device technologies, packaging and layout techniques, and cooling approaches can reduce losses at higher switching frequencies while reducing electromagnetic interference.

Integrating a power electronic converter into the electrical grid presents its own form of challenges including harmonics, power quality, and grid stability. Investigating advanced grid synchronization techniques, active power filtering algorithms, and grid support functionality could enhance the compatibility of the TAB with existing grid infrastructure. In addition, through the current implementation of the control algorithm, the DC bridge must abruptly begin supplying power to the AC output bridge surrounding the AC input zero crossing. This distorts the sinusoidal nature of the AC input bridge current waveform, resulting in a decreased power factor or the undesirable injection of harmonics. Power factor analysis or an eased shift in power transfer could potentially mitigate these issues.

The operation of the converter topology in a research environment is a highly controlled operational setting. Implementation of such a converter topology within real-world applications subjects it to various environmental factors including extreme temperatures, humidity, dust and other contaminants, mechanical shock and vibration, and electrical interference. Conducting a reliability analysis of the TAB converter under various operating conditions and environmental factors can provide insight into its long-term performance and degradation mechanisms.

In conclusion, the aforementioned directions for future research represent avenues for building upon the work presented in this thesis and further advancing the field of power electronics, specifically the TAB converter. By addressing these challenges and exploring new opportunities for innovation, researchers can contribute to the development of more efficient, reliable, and sustainable electrical systems to meet the evolving demands of the modern world.

APPENDIX A.

TAB TWO-SWITCH BOARD PCB SCHEMATIC AND LAYOUT

1. TAB TWO-SWITCH BOARD SCHEMATIC

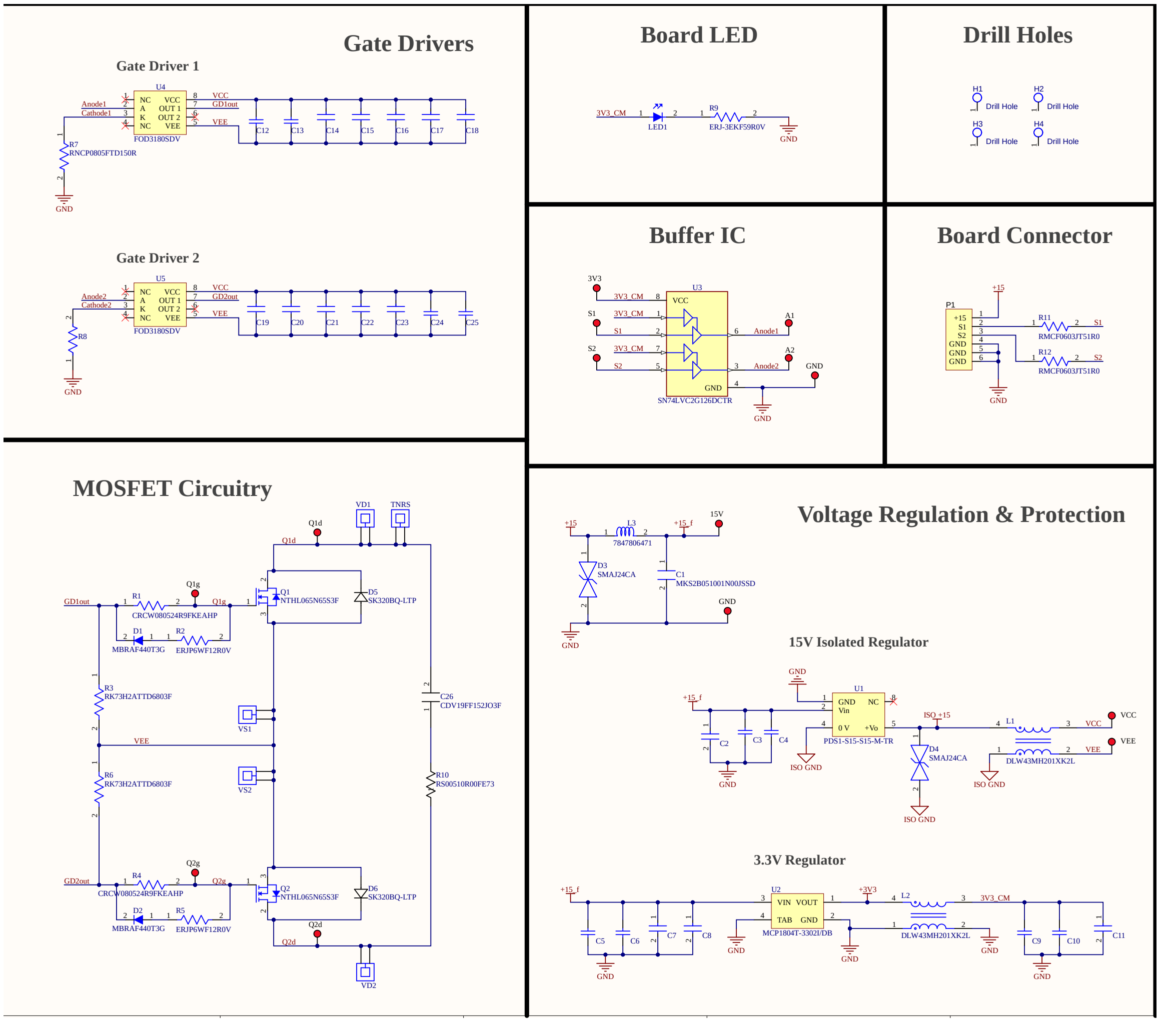

Figure 1. Schematic of the two-switch board.

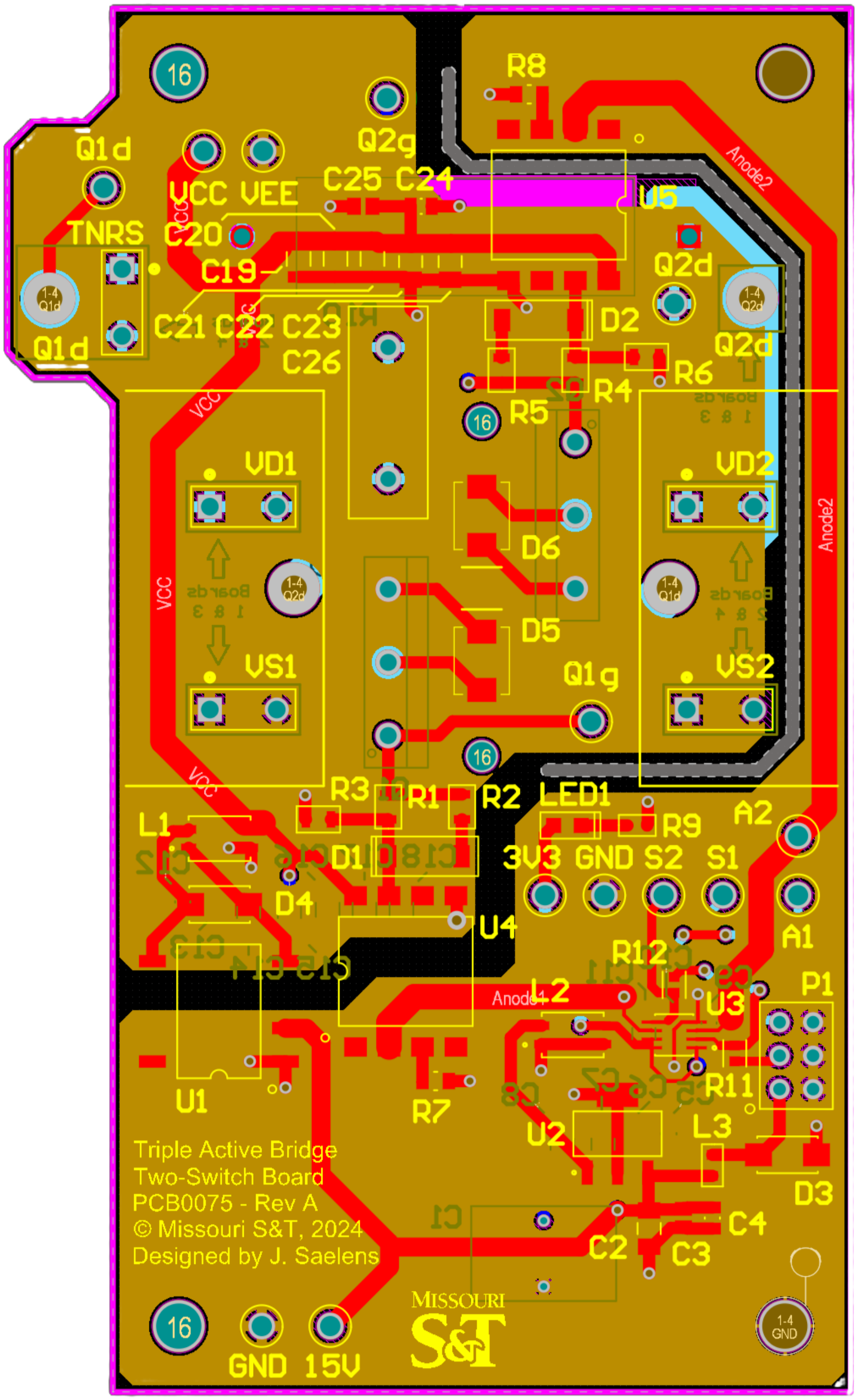

Figure 2. Top side 2D layout view of two-switch board.

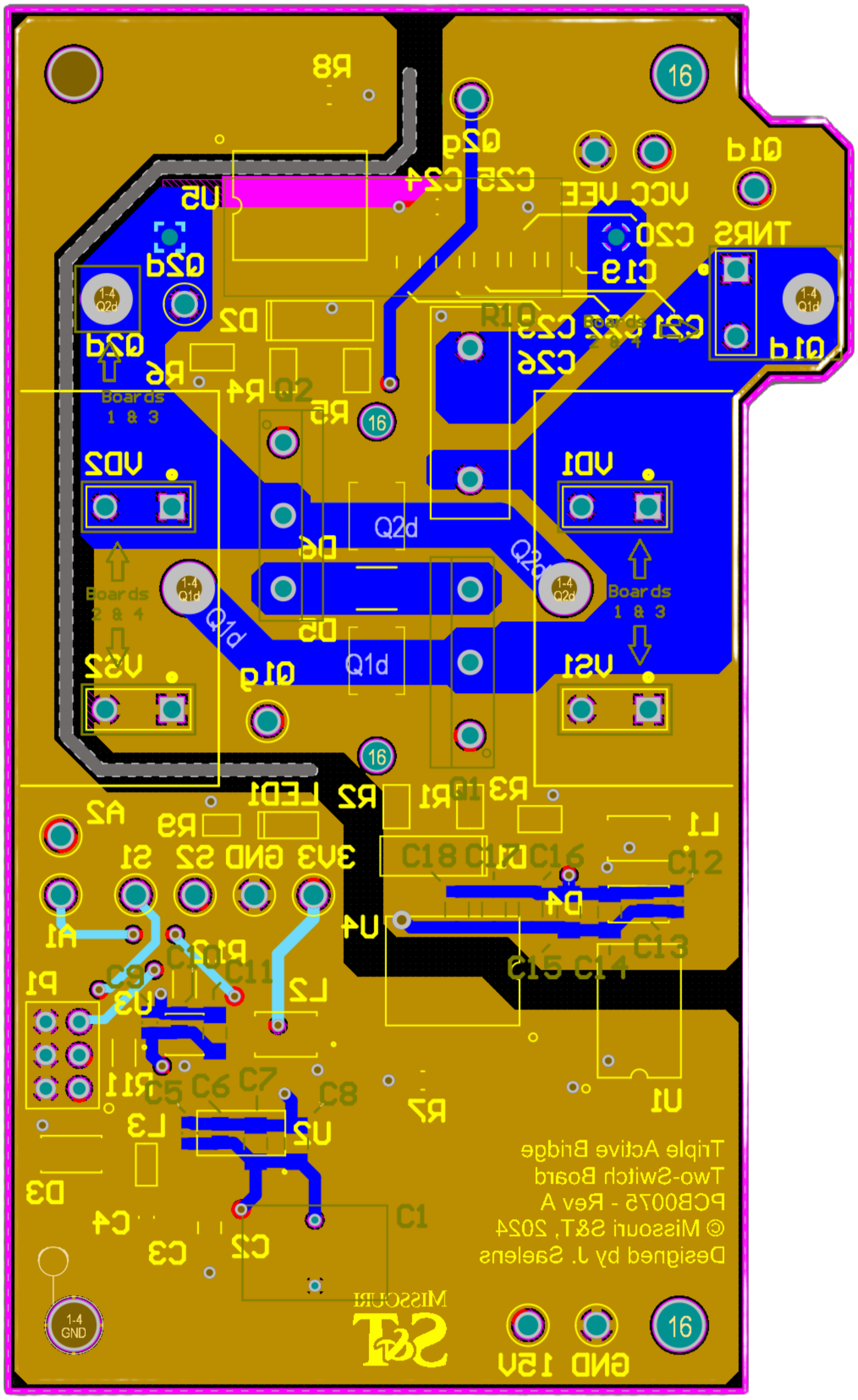

Figure 3. Bottom side 2D layout view of two-switch board.

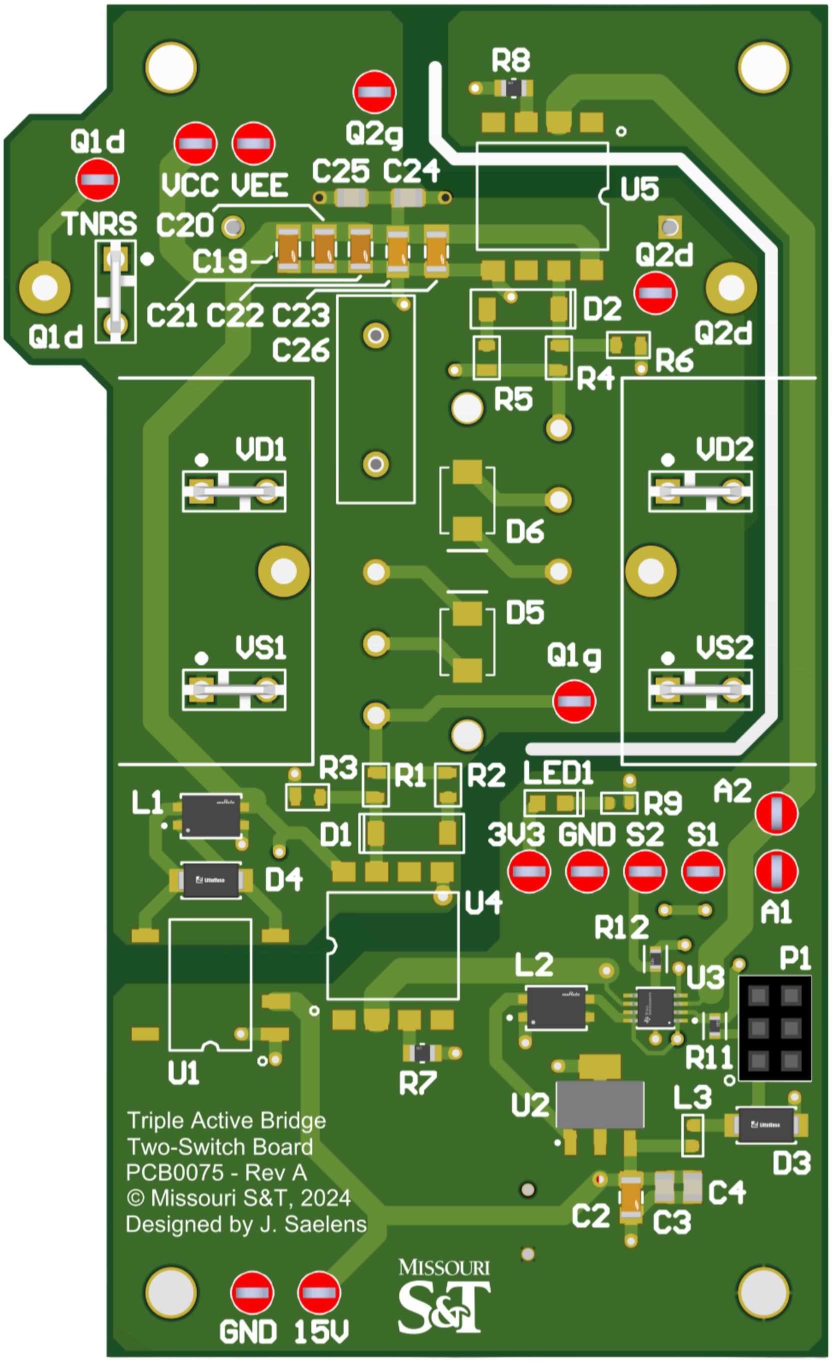

Figure 4. Top side 3D layout view of two-switch board.

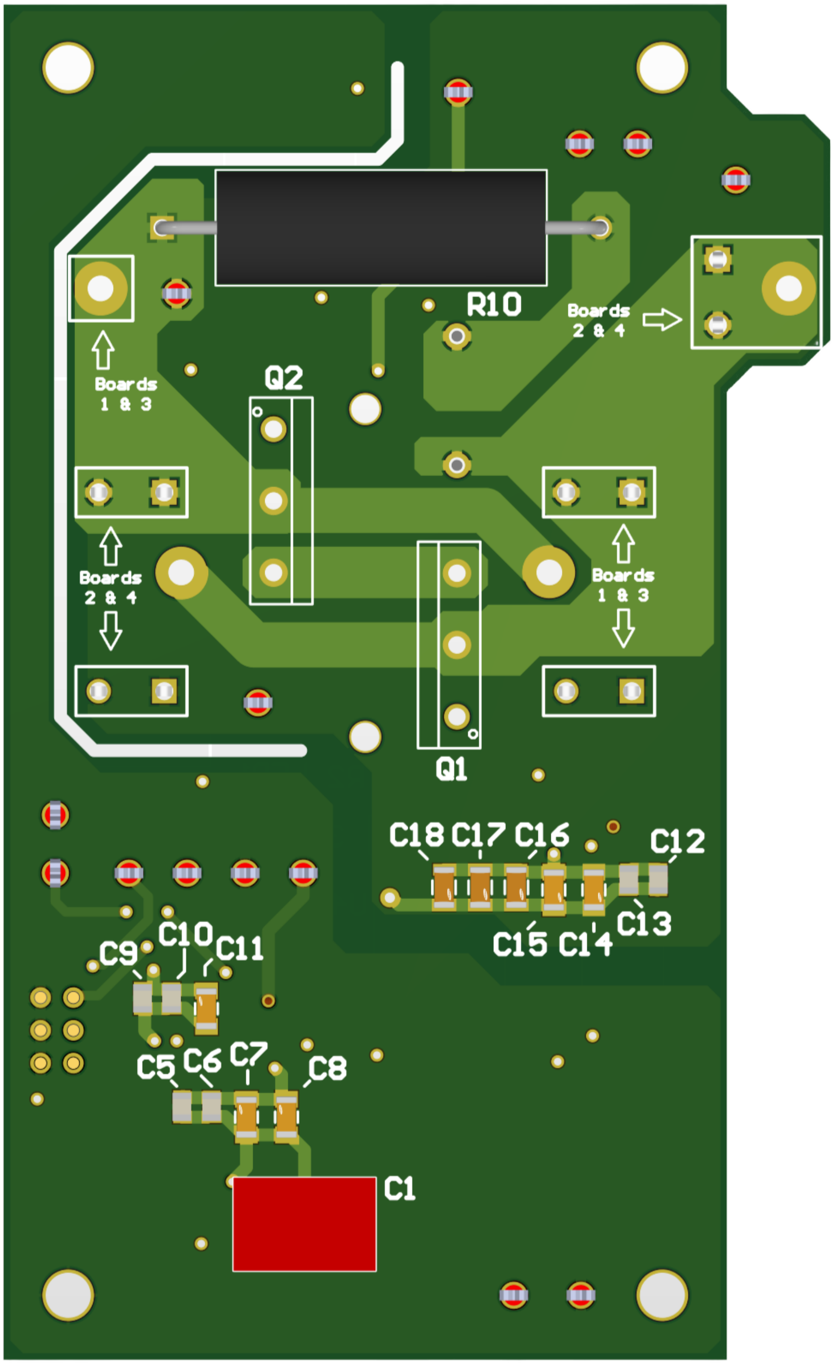

Figure 5. Bottom side 3D layout view of two-switch board.

APPENDIX B.

DC-AC-AC TAB NEWTON-RAPHSON MATLAB CONTROL CODE

```
#define PIE 3.141592653589793238

//Define transformer leakage inductances
#define L1 1.978e-5
#define L2 1.414e-5
#define L3 1.136e-5

//Define grid and switching elements
#define Fsw 10e3
#define fg 60
#define tg 1/fg
#define w_fg 2*PIE*fg

//These are used to shift power from input AC bridge to DC bridge
//Surrounding the zero crossings in the input voltage
//Specify minimum compensation voltage (V)
#define B1_CompensationVoltage 2

//Define maximum and minimum values for phi
#define phiBoundary 0.04
#define maxPhiValue ((PIE/2) - phiBoundary)
#define minPhiValue ((-PIE/2) + phiBoundary)

//Phi values for maximum power transfer to bridge 1
#define phi2_maxPwrToB1 minPhiValue
#define phi3_maxPwrToB1 minPhiValue
#define ABS_phi2_maxPwrToB1 maxPhiValue
#define ABS_phi3_maxPwrToB1 maxPhiValue

//Phi values for maximum power transfer to bridge 2
#define phi2_maxPwrToB2 maxPhiValue
#define phi3_maxPwrToB2 -phiBoundary
#define ABS_phi2_maxPwrToB2 maxPhiValue
#define ABS_phi3_maxPwrToB2 phiBoundary

//Phi values for maximum power transfer to bridge 3
#define phi2_maxPwrToB3 -phiBoundary
#define phi3_maxPwrToB3 maxPhiValue
#define ABS_phi2_maxPwrToB3 phiBoundary
#define ABS_phi3_maxPwrToB3 maxPhiValue

#define ABS__phi2_maxPwrToB3_min_phi3_maxPwrToB3 (phiBoundary +
   maxPhiValue)

//These values aren't too important. They will only be used on
   the first iteration. Successive iterations will use previously
    calculated ones
#define StartingPhi2Val 0.1
#define StartingPhi3Val 0.2


//Used in the beginning of mainPwrFunc()
//Further reduces the computation time
```

```
//The following line implements this: phi3_maxPwrToB3*(fabsf(
   phi3_maxPwrToB3)-PIE)
#define maxB1ToB3_val1 phi3_maxPwrToB3*(ABS_phi3_maxPwrToB3-PIE)
//The following line implements this: (phi2_maxPwrToB3-
   phi3_maxPwrToB3)*(PIE-fabsf(phi2_maxPwrToB3-phi3_maxPwrToB3))
#define maxB2ToB3_val1 (phi2_maxPwrToB3-phi3_maxPwrToB3)*(PIE-
   ABS__phi2_maxPwrToB3_min_phi3_maxPwrToB3)

//Placeholders to store variables that are needed multiple times
   through the phase calculation iteration
float V_B1_V_B2_L3;
float V_B1_V_B3_L2;
float V_B2_V_B3_L1;
float Expr1;
float Expr2;
float Expr1_PLUS_Expr2;
float Expr3;
float Expr4;
float Expr5_Helper;
float Expr5;
float Expr6;
float Expr7;
float Expr8;
float Expr9;
float Expr10;
float Expr11;
float fabsf_phi2_old;
float fabsf_phi3_old;
float fabsf_phi2_min_phi3_old;
float Volt_B1;
float Volt_B2;
float Volt_B3;

//Precompute the denominator of the average power flow equations
float Equation_Denominator_Inv = 1/(2*Fsw*PIE*PIE*(L1*L2+L1*L3+L2
   *L3));
#define Equation_Denominator_Inv_Squared Equation_Denominator_Inv
   *Equation_Denominator_Inv

//Calculate power at P2 (P1+P2+P3=0)
short P2_needed;

//Initialize phi2 and phi3 to initial guesses
float phi2_old = StartingPhi2Val;
float phi3_old = StartingPhi3Val;

//Used for memory wrapping
float phi2_new, phi3_new;

// Convergence criteria
float tolerance = 1e-6;
short max_iterations = 10;
```

```
//Used internally to guide the iteration process
int loopCounter;
short count;

//Positive means power source, negative means power sink
float Pdt_B3 = 0;
float Qdt_B3 = 0;
float P3_Total = 0;

//Stores the maximum possible power transfer between bridges
float maxPwrTrnsfrB1ToB3_num;
float maxPwrTrnsfrB2ToB3_num;
float maxPwrTrnsfrToB3;
float maxPwrTrnsfrB1ToB3;

//Used internally to store if the Newton-Raphson power algorithm
   should execute or if it should be skipped
short iteratePower = 1;


//This is the main phase calculation routine that determines the
   values of phi2 and phi3 based on the desired power transfer
void phiCalcRoutine(short P1_desired, short P3_Pdesired, short
   P3_Qdesired, float *V_B1, float *V_B2, float *V_B3, float
   t_grid, float *phi2_res, float *phi3_res)
{
    //Obtain the bridge voltages
    Volt_B1 = *V_B1;
    Volt_B2 = *V_B2;
    Volt_B3 = *V_B3;

    //Precompute some of the voltage and inductance parameters
    V_B1_V_B2_L3 = Volt_B1 * Volt_B2 * L3;
    V_B1_V_B3_L2 = Volt_B1 * Volt_B3 * L2;
    V_B2_V_B3_L1 = Volt_B2 * Volt_B3 * L1;

    //Combine active and reactive into total power
    Pdt_B3 = P3_Pdesired - P3_Pdesired*cos(2*w_fg*t_grid);
    Qdt_B3 = P3_Qdesired*sin(2*w_fg*t_grid);
    P3_Total = Pdt_B3 + Qdt_B3;

    if((*V_B2 != 0) && (*V_B3 != 0))
    {
        maxPwrTrnsfrB1ToB3_num = (V_B1_V_B3_L2*maxB1ToB3_val1);
        maxPwrTrnsfrB2ToB3_num = (V_B2_V_B3_L1*maxB2ToB3_val1);
        maxPwrTrnsfrToB3 = (maxPwrTrnsfrB1ToB3_num +
   maxPwrTrnsfrB2ToB3_num) * Equation_Denominator_Inv;

        //Can't achieve desired power transfer to B3 so supply
   zero power
        if(maxPwrTrnsfrToB3 > P3_Total)
        {
            iteratePower = 0;
```

```
         phi2_old = 0.01;
         phi3_old = 0.01;

         phi2_new = 0.01;
         phi3_new = 0.01;
     }
     else
     {
         //Close to the output AC waveform zero crossing,
switch power distribution so that it comes from B1 instead
         if(Volt_B3 < B1_CompensationVoltage)
         {
             maxPwrTrnsfrB1ToB3 = maxPwrTrnsfrB1ToB3_num *
Equation_Denominator_Inv;

             //B1 can't supply all of the power necessary at
B3. Set B1 to maximum possible power transfer
             if(maxPwrTrnsfrB1ToB3 > P3_Total)
             {
                 P1_desired = -maxPwrTrnsfrB1ToB3;
                 P2_needed = maxPwrTrnsfrB1ToB3 - P3_Total;
             }
             else
             {
                 P1_desired = -P3_Total;
                 P2_needed = 0;
             }
         }
     }

     for(count = 0; count < 2; count++)
     {
         if(iteratePower)
         {
             //Newton-Raphson iterations for the combined
system of equations
             for(loopCounter = 1; loopCounter <=
max_iterations; loopCounter++)
             {
                 //Check if phi2_old and phi3_old are exactly
the same
                 if(phi2_old == phi3_old)
                 {
                     if(phi2_old >= 0)
                     {
                         phi2_old = phi2_old - 0.05;
                     }
                     else
                     {
                         phi2_old = phi2_old + 0.05;
                     }
                 }
```

```
                 //Implements the Newton-Raphson proposed
method symbolically to significantly improve efficiency
                 fabsf_phi2_old = fabsf(phi2_old);
                 fabsf_phi3_old = fabsf(phi3_old);
                 fabsf_phi2_min_phi3_old = fabsf(phi2_old-
phi3_old);
                 Expr1 = (V_B2_V_B3_L1*(PIE-
fabsf_phi2_min_phi3_old))-((V_B2_V_B3_L1*(phi2_old-phi3_old)
*(2*phi2_old-2*phi3_old))/(2*fabsf_phi2_min_phi3_old));
                 Expr2 = (V_B1_V_B3_L2*(PIE-fabsf_phi3_old))
-((V_B1_V_B3_L2*phi3_old*phi3_old)/fabsf_phi3_old);
                 Expr1_PLUS_Expr2 = Expr1+Expr2;
                 Expr3 = (V_B1_V_B2_L3*(PIE-fabsf_phi2_old))
-((V_B1_V_B2_L3*phi2_old*phi2_old)/fabsf_phi2_old);
                 Expr4 = ((Equation_Denominator_Inv_Squared*
Expr1_PLUS_Expr2*Expr1_PLUS_Expr2)+(
Equation_Denominator_Inv_Squared*Expr1*Expr1))*((
Equation_Denominator_Inv_Squared*Expr2*Expr2)+(
Equation_Denominator_Inv_Squared*Expr3*Expr3));
                 Expr5_Helper = ((
Equation_Denominator_Inv_Squared*Expr2*Expr1_PLUS_Expr2)-(
Equation_Denominator_Inv_Squared*Expr1*Expr3));
                 Expr5 = 1/(Expr4-(Expr5_Helper*Expr5_Helper))
;
                 Expr6 = P3_Total-(Equation_Denominator_Inv*(
V_B2_V_B3_L1*(PIE-fabsf_phi2_min_phi3_old)*(phi2_old-phi3_old)
-V_B1_V_B3_L2*phi3_old*(PIE-fabsf_phi3_old)));
                 Expr7 = P1_desired-(Equation_Denominator_Inv
*(V_B1_V_B2_L3*phi2_old*(PIE-fabsf_phi2_old)+V_B1_V_B3_L2*
phi3_old*(PIE-fabsf_phi3_old)));

                 Expr8 = (Equation_Denominator_Inv_Squared*
Expr1_PLUS_Expr2*Expr1_PLUS_Expr2)+(Expr1*Expr1*
Equation_Denominator_Inv_Squared);
                 Expr9 = (Expr2*
Equation_Denominator_Inv_Squared)*Expr1_PLUS_Expr2;
                 Expr10 = Expr9-(Expr1*Expr3*
Equation_Denominator_Inv_Squared);
                 Expr11 = (Equation_Denominator_Inv_Squared*
Expr2*Expr2)+(Equation_Denominator_Inv_Squared*Expr3*Expr3);

                 //Update phi2 and phi3 using the corrections
                 phi2_new = phi2_old + Expr7*(
Equation_Denominator_Inv*Expr1*Expr5*Expr10+
Equation_Denominator_Inv*Expr3*Expr5*Expr8)+Expr6*(
Equation_Denominator_Inv*Expr1*Expr5*Expr11+
Equation_Denominator_Inv*Expr3*Expr5*Expr10);
                 phi3_new = phi3_old - Expr7*(
Equation_Denominator_Inv*Expr5*Expr10*Expr1_PLUS_Expr2-
Equation_Denominator_Inv*Expr2*Expr5*Expr8)-Expr6*(
Equation_Denominator_Inv*Expr5*Expr11*Expr1_PLUS_Expr2-
Equation_Denominator_Inv*Expr2*Expr5*Expr10);
```

```
                 //Saturation on values of phi
                 if(phi2_new > maxPhiValue)
                 {
                     phi2_new = maxPhiValue;
                 }
                 else if(phi2_new < minPhiValue)
                 {
                     phi2_new = minPhiValue;
                 }

                 if(phi3_new > maxPhiValue)
                 {
                     phi3_new = maxPhiValue;
                 }
                 else if(phi3_new < minPhiValue)
                 {
                     phi3_new = minPhiValue;
                 }

                 //Check for convergence
                 if(computeEuclideanNorm(phi2_new - phi2_old,
phi3_new - phi3_old) < tolerance)
                 {
                     //Convergence achieved
                     iteratePower = 0;
                     break;
                 }

                 //Update old values for next iteration
                 phi2_old = phi2_new;
                 phi3_old = phi3_new;

                 //If we reach maximum iterations and still
haven't found a good solution, there is an error in finding
the solution
                 //Meaning the desired combination with
desired power at port 1 is not possible
                 if(loopCounter == max_iterations)
                 {
                     //Reset values of phi2 and phi3
                     phi2_old = StartingPhi2Val;
                     phi3_old = StartingPhi3Val;

                     //Set desired power at port 1 equal to
zero
                     P1_desired = 0;
                     break;
                 }

             } //End for(loopCounter = 0; loopCounter <
max_iterations; loopCounter++)

         } //End if(iteratePower)
```

```
        } //End for(count = 0; count < 2; count++)
    }

    //Reset value so algorithm runs properly again next time
    iteratePower = 1;

    //Update the resulting values of phi2 and phi3
    *phi2_res = phi2_new;
    *phi3_res = phi3_new;
}

//Supplementary function used in determining algorithmic
   convergence
float computeEuclideanNorm(float x, float y)
{
    return sqrtf(x * x + y * y);
}
```

Listing B.1. Iterative power flow control algorithm for the triple active bridge.

REFERENCES

[1] Md Safayatullah, Mohamed Tamasas Elrais, Sumana Ghosh, Reza Rezaii, and Issa Batarseh. A comprehensive review of power converter topologies and control methods for electric vehicle fast charging applications. *IEEE Access*, 10:40753–40793, 2022. doi: 10.1109/ACCESS.2022.3166935.

[2] Xu She, Alex Q. Huang, and Rolando Burgos. Review of solid-state transformer technologies and their application in power distribution systems. *IEEE Journal of Emerging and Selected Topics in Power Electronics*, 1(3):186–198, 2013. doi: 10.1109/JESTPE.2013.2277917.

[3] Subhashish Bhattacharya, Tiefu Zhao, Gangyao Wang, Sumit Dutta, Seunghun Baek, Yu Du, Babak Parkhideh, Xiaohu Zhou, and Alex Q. Huang. Design and development of generation-i silicon based solid state transformer. In *2010 Twenty-Fifth Annual IEEE Applied Power Electronics Conference and Exposition (APEC)*, pages 1666–1673, 2010. doi: 10.1109/APEC.2010.5433455.

[4] Hengsi Qin and Jonathan W. Kimball. A comparative efficiency study of silicon-based solid state transformers. In *2010 IEEE Energy Conversion Congress and Exposition*, pages 1458–1463, 2010. doi: 10.1109/ECCE.2010.5618255.

[5] Gouri Deshmukh, Pradyumn Chaturvedi, and Vedashree Rajderkar. Single phase cascaded h-bridge multilevel inverter topology. In *2022 International Conference on Futuristic Technologies (INCOFT)*, pages 1–6, 2022. doi: 10.1109/INCOFT55651.2022.10094514.

[6] N Sujitha. and K Ramani. A new hybrid cascaded h-bridge multilevel inverter - performance analysis. In *IEEE-International Conference On Advances In Engineering, Science And Management (ICAESM -2012)*, pages 46–50, 2012.

[7] Mohsen Feizi and Reza Beiranvand. An improved phase-shifted full-bridge converter with extended zvs operation range for ev battery charger applications. In *2020 11th Power Electronics, Drive Systems, and Technologies Conference (PEDSTC)*, pages 1–6, 2020. doi: 10.1109/PEDSTC49159.2020.9088444.

[8] Snehal Chothe, Rajaram. T. Ugale, and Ameya Gambhir. Design and modeling of phase shifted full bridge dc-dc converter with zvs. In *2021 National Power Electronics Conference (NPEC)*, pages 01–06, 2021. doi: 10.1109/NPEC52100.2021.9672529.

[9] Amit Kumar Jain and Rajapandian Ayyanar. Pwm control of dual active bridge: Comprehensive analysis and experimental verification. *IEEE Transactions on Power Electronics*, 26(4):1215–1227, 2011. doi: 10.1109/TPEL.2010.2070519.

[10] Yanhui Xie, Jing Sun, and James S. Freudenberg. Power flow characterization of a bidirectional galvanically isolated high-power dc/dc converter over a wide operating range. *IEEE Transactions on Power Electronics*, 25(1):54–66, 2010. doi: 10.1109/TPEL.2009.2024151.

[11] Hengsi Qin and Jonathan W. Kimball. Solid-state transformer architecture using ac–ac dual-active-bridge converter. *IEEE Transactions on Industrial Electronics*, 60(9): 3720–3730, 2013. doi: 10.1109/TIE.2012.2204710.

[12] Hengsi Qin and Jonathan W. Kimball. Closed-loop control of dc–dc dual-active-bridge converters driving single-phase inverters. *IEEE Transactions on Power Electronics*, 29 (2):1006–1017, 2014. doi: 10.1109/TPEL.2013.2257859.

[13] Angshuman Sharma, Kartikeya Jp Veeramraju, and Jonathan W. Kimball. Power flow control of a single-stage ac-ac solid-state transformer for ac distribution system. In *2022 IEEE Power and Energy Conference at Illinois (PECI)*, pages 1–6, 2022. doi: 10.1109/PECI54197.2022.9744006.

[14] Hengsi Qin and Jonathan W. Kimball. Generalized average modeling of dual active bridge dc–dc converter. *IEEE Transactions on Power Electronics*, 27(4):2078–2084, 2012. doi: 10.1109/TPEL.2011.2165734.

[15] Kartikeya Jp Veeramraju, Angshuman Sharma, and Jonathan W. Kimball. A comprehensive analysis on complex power flow mechanism in an ac-ac dual active bridge. In *2022 IEEE Power and Energy Conference at Illinois (PECI)*, pages 1–6, 2022. doi: 10.1109/PECI54197.2022.9744009.

[16] Yiding Jin, Qiang Song, Wenhua Liu, and Weixin Sun. Cascaded battery energy storage system based on dual active bridges and a common dc bus. In *2010 Conference Proceedings IPEC*, pages 1019–1024, 2010. doi: 10.1109/IPECON.2010.5696964.

[17] Nezihe Yildiran. Design methodology and implementation of half-bridge llc resonant converter. In *2020 International Conference on Electrical, Communication, and Computer Engineering (ICECCE)*, pages 1–6, 2020. doi: 10.1109/ICECCE49384.2020.9179322.

[18] Hai-Nam Vu, Dai-Duong Tran, and Woojin Choi. A novel hybrid soft switching full-bridge pwm and full-bridge llc converter for on-board battery charger applications. In *2016 IEEE 8th International Power Electronics and Motion Control Conference (IPEMC-ECCE Asia)*, pages 2470–2473, 2016. doi: 10.1109/IPEMC.2016.7512686.

[19] Jingyu Shen, Liang Jing, and Jinpeng Qiu. High-frequency full-bridge 48v dc-5v dc llc resonant converter with algan/gan hemts. In *2023 5th International Conference on Electrical Engineering and Control Technologies (CEECT)*, pages 338–342, 2023. doi: 10.1109/CEECT59667.2023.10420770.

[20] Xiaoqiang Li, Jinwei Huang, Yongchao Ma, Xintan Wang, Jiafeng Yang, and Xiaojie Wu. Unified modeling, analysis, and design of isolated bidirectional cllc resonant dc–dc converters. *IEEE Journal of Emerging and Selected Topics in Power Electronics*, 10(2):2305–2318, 2022. doi: 10.1109/JESTPE.2022.3145817.

[21] Shenli Zou, Jiangheng Lu, Ayan Mallik, and Alireza Khaligh. Bi-directional cllc converter with synchronous rectification for plug-in electric vehicles. *IEEE Transactions on Industry Applications*, 54(2):998–1005, 2018. doi: 10.1109/TIA.2017.2773430.

[22] Wei Chen, Ping Rong, and Zhengyu Lu. Snubberless bidirectional dc–dc converter with new cllc resonant tank featuring minimized switching loss. *IEEE Transactions on Industrial Electronics*, 57(9):3075–3086, 2010. doi: 10.1109/TIE.2009.2037099.

[23] Angshuman Sharma, Alvaro Cardoza, Kartikeya J. P. Veeramraju, Oroghene Oboreh-Snapps, and Jonathan W. Kimball. Bidirectional asymmetric clllc resonant dc-dc converter for onboard electric vehicle chargers. In *2023 IEEE Energy Conversion Congress and Exposition (ECCE)*, pages 2109–2116, 2023. doi: 10.1109/ECCE53617.2023.10362332.

[24] Zaka Ullah Zahid, Zakariya M. Dalala, Rui Chen, Baifeng Chen, and Jih-Sheng Lai. Design of bidirectional dc–dc resonant converter for vehicle-to-grid (v2g) applications. *IEEE Transactions on Transportation Electrification*, 1(3):232–244, 2015. doi: 10.1109/TTE.2015.2476035.

[25] Sheng-Yang Yu, Chris Hsiao, and Jack Weng. A high frequency clllc bi-directional series resonant converter dab using an integrated pcb winding transformer. In *2020 IEEE Applied Power Electronics Conference and Exposition (APEC)*, pages 1074–1080, 2020. doi: 10.1109/APEC39645.2020.9124521.

[26] Stefan Ditze, Stefan Ehrlich, Dominik Happel, and Andreas Rosskopf. Asymmetric resonant tank design for a bidirectional cllc resonant converter in g2v and v2g operation. In *2023 IEEE Applied Power Electronics Conference and Exposition (APEC)*, pages 1358–1365, 2023. doi: 10.1109/APEC43580.2023.10131351.

[27] Chuanhong Zhao, Simon D. Round, and Johann W. Kolar. An isolated three-port bidirectional dc-dc converter with decoupled power flow management. *IEEE Transactions on Power Electronics*, 23(5):2443–2453, 2008. doi: 10.1109/TPEL.2008.2002056.

[28] Subhradip Mukherjee and Indrajit Sarkar. A brief review on triple active bridge dc-dc converter. In *2023 IEEE International Students' Conference on Electrical, Electronics and Computer Science (SCEECS)*, pages 1–6, 2023. doi: 10.1109/SCEECS57921.2023.10063031.

[29] Venkateswara Rao Kudaravalli, Vishwabandhu Uttam, and Vishnu Mahadeva Iyer. A design methodology for triple active bridge dc- dc converter. In *2022 IEEE International Conference on Power Electronics, Drives and Energy Systems (PEDES)*, pages 1–7, 2022. doi: 10.1109/PEDES56012.2022.10080029.

[30] Ritwik Chattopadhyay, Sayan Acharya, Ghanshyamsinh Gohil, and Subhashish Bhattacharya. One switching cycle current control strategy for triple active bridge phase-shifted dc-dc converter. In *2017 IEEE Industry Applications Society Annual Meeting*, pages 1–8, 2017. doi: 10.1109/IAS.2017.8101785.

[31] Kazuki Minami, Shota Okutani, Masaya Ohura, Pin-Yu Huang, and Yuichi Kado. Machine learning aided optimized modulation in triple active bridge converter. In *IECON 2022 – 48th Annual Conference of the IEEE Industrial Electronics Society*, pages 1–6, 2022. doi: 10.1109/IECON49645.2022.9968640.

[32] Manuel Alva Hernández and Damian Sal y Rosas. Single-stage bidirectional triple active bridge ac-dc converter for single phase grid applications. In *2020 IEEE Kansas Power and Energy Conference (KPEC)*, pages 1–6, 2020. doi: 10.1109/KPEC47870.2020.9167522.

[33] Jherson Andrade, Damian Sal y Rosas, David Frey, and Jean-Paul Ferrieux. Modified triple active bridge dc/ac three-phase converter with a series-resonant lc circuit on the ac-side. In *2017 IEEE Southern Power Electronics Conference (SPEC)*, pages 1–6, 2017. doi: 10.1109/SPEC.2017.8333612.

[34] Keigo Katagiri, Shota Nakagawa, Kento Kurosawa, Junichi Arai, Yuichi Kado, and Keiji Wada. Power flow control of triple active bridge converter equipped with ac/dc converter for constructing autonomous hybrid ac/dc microgrid systems. In *IECON 2017 - 43rd Annual Conference of the IEEE Industrial Electronics Society*, pages 1441–1446, 2017. doi: 10.1109/IECON.2017.8216245.

[35] Saravanan Ilango, R Viju Nair, Ritwik Chattopadhyay, and Subhashish Bhattacharya. Photovoltaic and energy storage grid integration with fully modular architecture using triple port active bridges and cascaded h-bridge inverter. In *IECON 2018 - 44th Annual Conference of the IEEE Industrial Electronics Society*, pages 1400–1405, 2018. doi: 10.1109/IECON.2018.8591763.

[36] Van-Long Pham and Keiji Wada. Applications of triple active bridge converter for future grid and integrated energy systems. *Energies*, 13(7), 2020. ISSN 1996-1073. doi: 10.3390/en13071577. URL https://www.mdpi.com/1996-1073/13/7/1577.

[37] Shenli Zou, Jiangheng Lu, Ayan Mallik, and Alireza Khaligh. Modeling and optimization of an integrated transformer for electric vehicle on-board charger applications. *IEEE Transactions on Transportation Electrification*, 4(2):355–363, 2018. doi: 10.1109/TTE.2018.2804328.

[38] Viju Nair R., Srinivas Gulur, Ritwik Chattopadhyay, and Subhashish Bhattacharya. Integrating photovoltaics and battery energy storage to grid using triple active bridge and voltage source converters. In *IECON 2020 The 46th Annual Conference of the IEEE Industrial Electronics Society*, pages 3691–3696, 2020. doi: 10.1109/IECON43393.2020.9255053.

[39] Babak Rahrovi, Ramin Tafazzoli Mehrjardi, and Mehrdad Ehsani. On the analysis and design of high-frequency transformers for dual and triple active bridge converters in more electric aircraft. In *2021 IEEE Texas Power and Energy Conference (TPEC)*, pages 1–6, 2021. doi: 10.1109/TPEC51183.2021.9384990.

[40] Zheqing Li, Feng Jin, Xin Lou, Yi-Hsun Hsieh, Qiang Li, and Fred C. Lee. A transformer design with pcb litz wire concept for solid state transformer. In *2023 IEEE Energy Conversion Congress and Exposition (ECCE)*, pages 848–854, 2023. doi: 10.1109/ECCE53617.2023.10362376.

[41] Akrem Mohamed Elrajoubi and Simon S. Ang. High-frequency transformer review and design for low-power solid-state transformer topology. In *2019 IEEE Texas Power and Energy Conference (TPEC)*, pages 1–6, 2019. doi: 10.1109/TPEC.2019.8662131.

[42] Yue Yu, Keiji Wada, and Yuichi Kado. Power flow control of dc power distribution systems using triple active bridge converter in a data center. In *2018 9th IEEE International Symposium on Power Electronics for Distributed Generation Systems (PEDG)*, pages 1–6, 2018. doi: 10.1109/PEDG.2018.8447655.

[43] Jonathan Saelens, Lauryn Morris, Oroghene Oboreh-Snapps, Arnold Fernandes, Praneeth Uddarraju, Sophia A. Strathman, and Jonathan W. Kimball. Instantaneous current and average power flow characterization of a dc-dc-dc triple active bridge converter. In *2024 IEEE Power and Energy Conference at Illinois (PECI)*, pages 1–6, 2024.

[44] Deepak S and S. R. Mohanrajan. High-frequency transformer design for a bi-directional isolated dc-dc converter for electric vehicles. In *2022 IEEE 7th International Conference on Recent Advances and Innovations in Engineering (ICRAIE)*, volume 7, pages 428–432, 2022. doi: 10.1109/ICRAIE56454.2022.10054344.

VITA

Jonathan Henri Saelens earned his bachelor's Degree in Computer Engineering from Missouri University of Science and Technology (Missouri S&T) in Rolla, MO in May 2023. He received his master's in Electrical Engineering from Missouri S&T in July 2024. His research interests include dc-dc conversion and embedded processor design. He was the electrical lead engineer of the Missouri S&T Formula SAE Racing design team for the 2022-2023 and 2023-2024 seasons, where he designed the electrical wiring harnesses and multiple circuit boards including the power distribution module (PDM) and the brake light, and has been a member since August 2021. Additionally, he worked as a graduate teaching assistant for one semester, aiding with the advanced programmable logic controllers (PLC) laboratory exercises while at Missouri S&T.